Volume Increase of the Hippocampus after Electroconvulsive Therapy

The Role of the Electric Field and the Individual Differences due to Body Mass Index, Sex and Age

Ingrid Mossige

Master's Thesis in Medical Technology

Department of Physics and Technology
University of Bergen

June 2021

Abstract

Electroconvulsive therapy (ECT) involves passing an electrical current through the brain, intentionally causing a brief seizure. In Norway, it is common to calculate the dose according to an age-based method. Recent studies have shown that ECT induced volume changes in the grey matter areas, hippocampus and amygdala, strongly correlate with the strength of the electric field (EF). There is not yet a complete understanding of how EFs interact with the brain. This thesis aims to evaluate how well the age-based method accounts for individual differences and investigate the effect of ECT by estimating potential volume changes of the hippocampi resulting from the treatment combined with simulations of the EFs generated by the ECT stimulus.

This project is a part of the ongoing research in the ECT-MRI group at Mohn Medical Imaging and Visualization Centre (MMIV). To examine the longitudinal volume changes, T1-weighted magnetic resonance imaging (MRI) scans from 29 patients scanned once before and once after a series of right unilateral ECT were analysed. Variations between individuals were further characterised in regard to body mass index (BMI), sex and age, to examine the extent to which the treatment strategies used today take into account individual differences.

Statistically significant negative correlation values were found between the EF strength in the hippocampi and BMI and age. However, there were no significant relationships between volume change and the variables BMI and age. Furthermore, significantly higher EF strengths in the hippocampi were found in female patients compared to male patients. Corresponding significantly greater volume changes in the left hippocampus were found for female patients. Young women have also been reported to be at higher risk for side effects. Moreover, the relationship between volume change and EF strength reported in previous studies was confirmed. In summary, the results in this thesis show that the age-based method used in the clinic today does not correct for individual differences in a way that ensures equal effects of the ECT treatment.

Acknowledgements

I would like to thank everyone who has helped and supported me throughout my work with this thesis. First, I would like to thank my supervisor, Renate Grüner, for providing me with this interesting project, being encouraging and having faith in me. Thank you for your guidance and motivating conversations. I also appreciate you taking me to the MRI methods meetings, where you introduced me to many talented people and let me present my work twice.

I would also like to express my gratitude to my co-supervisor, Leif Oltedal. Thank you for showing great interest in my work, being available and for your insightful feedback throughout this project. Thank you for introducing me to the ECT-MRI group, who gave me helpful feedback and asked important questions when I presented my work. From this group, I would especially like to thank Ute Kessler, who took the time to show me the ECT department and the treatment device, and for sharing her knowledge in this field.

Thanks to everyone at MMIV that made me feel so welcome. Thanks to Njål Brekke for helping me with Docker, Hauke Bartsch for good discussions, ideas and technical help, Lea Sjurine Starck for good advice regarding R programming, Alexander Richard Craig-Craven for detailed answers to my questions and to Frank Riemer for giving me the chance to present at the MMIV seminar. I also want to thank Miklos Argyelan for answering my ROAST method questions and Yu Huang for replying and helping me with problems with ROAST when no one else could.

I want to thank all my friends and fellow students for all the love and support. A special thanks to Annette Høisæter, Jon Asgeir Torsvik, Jon Sverre Dyrkolbotn and Stian Maurseth for your good mood, suggestions and helpful discussions at all times. Without you, I could not have done this, and studying would not have been as fun. Lastly, I would like to thank my family that is always there for me, and Magnus Breivik Løvseth for all the love and encouragement.

Contents

Nomenclature

Abbreviations

BF Bifrontal

BMI Body Mass Index

BT Bitemporal

CSF Cerebrospinal Fluid

ECT Electroconvulsive Therapy

EF Electric Field

eTIV Estimated Total Intracranial Volume

FEM Finite Element Method

FOV Field of View

FS FreeSurfer

FSPGR Fast Spoiled Gradient Echo

GM Grey Matter

MRI Magnetic Resonance Imaging

NMR Nuclear Magnetic Resonance

RF Radio Frequency

ROAST	Realistic vOlumetic-Approach-based Simulator for Transcranial electric stimulation
ROI	Region of Interest
RUL	Right Unilateral
TE	Echo Time
TES	Transcranial Electric Stimulation
TI	Inversion Time
tp	Time point
TR	Repetition Time
TRD	Treatment-Resistant Depression
WM	White Matter

Symbols

α Flip angle

b Estimated regression coefficient

B_0 Strength of main magnetic field

$\mathbf{B}$ Magnetic field

β Regression coefficient

$\mathbf{E}$ Electric field

ε_0 Permittivity

ε Electromotive force

f Pulse frequency

f_{pp} Pulse pair frequency

γ Gyromagnetic ratio

G_{fe} Frequency encoding gradient

G_{pe} Phase encoding gradient

G_{ss} Slice selecting gradient

$\hbar$ Reduced Planck constant

i Stimulus current

$\overrightarrow{J}$ Total angular momentum

$\mathbf{J}$ Current density

k Boltzmann's constant

$\overrightarrow{\mu}$ Magnetic moment

μ_0 Permeability of free space

$\overrightarrow{M}$ The net magnetisation of a sample

n Number of treatment sessions

N_s Number of spins in a sample

ω_0 Larmor frequency

Φ_B Flux of a magnetic field

Q Stimulus dose

Q_{avg} Average stimulus dose

Q_c Cumulative stimulus dose

ρ Charge density

σ Conductivity

τ Pulse width

t_{dur} Total stimulus duration

T_s Temperature of spin system

T_e Exposure time

ΔV Percentage volume change

$\mathbf{v}$ Velocity of particle with charge

List of Figures

List of Tables

Chapter 1

Introduction

Depression is currently a leading cause of disability worldwide, with more than 264 million people suffering from it. It can lead to great personal suffering, poor functionality in everyday life and an increased risk of suicide [1]. Therefore, effective treatment for this psychiatric disorder is essential to ease the burden that depression imposes on both the individuals and the society. Of the patients suffering from major depressive disorder, there are many people with treatment-resistant depression (TRD). For people with TRD, the most effective antidepressant treatment currently available is electroconvulsive therapy (ECT) [2][3]. ECT is a procedure in which a controlled amount of electrical current is passed through the brain to induce a brief seizure. The current is passed through electrodes on the scalp into the brain while the patient is under anesthesia. ECT is generally used when the standard treatment fails and for the most severely depressed. However, the use of ECT is limited by possible cognitive side effects such as severe memory loss and a high rate of relapse [4]. In addition, it is still largely unknown how ECT works and why it is effective. To reduce side effects and improve dosing paradigms, there is a need for a better understanding of the mechanisms of ECT.

Researchers in the Global ECT-MRI Research Collaboration (GEMRIC), the world's largest ECT-MRI study coordinated from Bergen, have recently shown that volume changes after ECT are broadly distributed in the brain [5] and that the volumetric changes after ECT are strongly correlated with the strength of the electric field, especially in the hippocampus and amygdala [6]. These findings suggest that it is the electrical stimulus and not the seizure that is important for the biological volume changes. However, a 2018 study found that there was no link between volume change of the hippocampus and clinical improvement [7]. Of the patients in this study, the patients with the largest volume increases had the worst outcome. There are also studies suggesting that volume changes may and may not be associated with cognitive side effect [8][9]. With many contradicting study results, it is clear that the causes of volume changes need to be investigated further.

The two most common methods used for calculating the electrical stimulation dose in ECT are the age-based and seizure threshold-based method [10]. Internationally, the method used varies, but in Norwegian practice, the age-based method is, so to speak, the only one used [11]. The age-based method depends on one parameter, age, but is sometimes corrected for differences in seizure threshold between the sexes. Knowing there are great variations in body mass index (BMI) within the groups of the same sex and age, this parameter should probably be taken into account when calculating the individual dose. Assuming that a higher BMI leads to a thicker cranial subcutaneous fat layer, less current would go through the scalp and into the brain in patients with a higher BMI undergoing ECT due to the low conductivity of fat.

The goal of this master of science project is to investigate how well the age-based method takes into account individual differences and ensures equal treatment effects. This will be evaluated by studying the extent to which variation in BMI, age, sex and intracranial volume affects the electric field distribution and strength, as well as volume change of the hippocampi after ECT treatment. Simulated electric fields based on anatomical magnetic resonance (MR) images will be used to explore the relationship between the electric field strength and volume change in the hippocampus. Variations in volume change and electric field strength between individuals will also be characterised in regard to electrical dose.

Chapter 2

Theory

For the work in the current thesis, it is important to understand the distribution of electric fields generated as part of the ECT treatment. This chapter introduces the basic theory of electromagnetism alongside an introduction to MR image generation and analysis. It also introduces the basics of ECT.

2.1 Electromagnetism

The electromagnetic force is one of the four fundamental forces in physics. For some time, electricity and magnetism were considered to be two separate subjects. However, it turned out that electricity and magnetism were linked, explaining different aspects of the same topic, electromagnetism. Maxwell's equations, together with Lorentz' force law, summarise the theoretical foundation of classical electromagnetism [12]. Maxwell's equations for electromagnetic fields are Gauss' law (Equation 2.1), Faraday's law (Equation 2.2), Gauss' law for magnetism (Equation 2.3) and Ampère's law with Maxwell's correction (Equation 2.4). They show how electric fields **E** and magnetic fields **B** depend on each other, and most importantly on electrical charges and currents.

$$\nabla \cdot \mathbf{E} = \frac{1}{\varepsilon_0}\rho, \tag{2.1}$$

$$\nabla \times \mathbf{E} = -\frac{\partial \mathbf{B}}{\partial t}, \tag{2.2}$$

$$\nabla \cdot \mathbf{B} = 0, \tag{2.3}$$

$$\nabla \times \mathbf{B} = \mu_0 \mathbf{J} + \mu_0 \varepsilon_0 \frac{\partial \mathbf{E}}{\partial t}, \tag{2.4}$$

In Maxwells's equations, ρ and $\mathbf{J}$ are the charge density and the current density respectively. Furthermore, ε_0 is the permittivity, and μ_0 is the permeability of free space [12]. By the divergence of **E**, Gauss' law describes how electric field lines flow out of positive charges and into negative ones. Faraday's law shows that a time-varying magnetic field through a conducting loop induces a circulating electric field. Gauss' law for magnetic fields illustrates that a magnetic field is an incompressible vector field since the divergence of **B** is zero. The field lines do not flow in or out of any point but are closed curve lines. Finally, Amperé's law with Maxwell's corrections demonstrates that a current and/or a time-varying electric field can induce a circulating magnetic field. Lorentz' force law tells us that the electromagnetic force on a particle with the charge q moving in a magnetic and electric field with the velocity $\mathbf{v}$ is given by Equation 2.5 [12].

$$\mathbf{F} = q(\mathbf{E} + \mathbf{v} \times \mathbf{B}) \tag{2.5}$$

2.1.1 Electromagnetic induction

The flux rule states that an electromotive force (emf) ε is induced if the flux of a magnetic field Φ_B changes. The induced emf is equal to the negative time rate of the magnetic flux through a loop [13], as can be seen in Equation 2.6.

$$\varepsilon = -\frac{d\Phi_B}{dt} \tag{2.6}$$

This induced emf will drive an induced current through the conducting loop. By Lenz's law, this current will flow in the direction that makes the produced flux oppose the change in flux. If the loop is stationary, the force that sets up the emf can not be magnetic [12]. This is because stationary charges do not experience magnetic forces. Electric fields, on the other hand, exert force on stationary charges. Faraday discovered that a changing magnetic field induces an electric field, and an induced electric field is what gives rise to the induced emf when a loop is stationary (see Equation 2.7) [12].

$$\varepsilon = \oint \mathbf{E} \cdot d\mathbf{l} \tag{2.7}$$

Equation 2.7 together with Equation 2.6, where Φ_B is substituted with the surface integral of the magnetic field change perpendicular to the surface, gives Faraday's law 2.8 [12].

$$\oint \mathbf{E} \cdot d\mathbf{l} = -\int \frac{\partial \mathbf{B}}{\partial t} \cdot d\mathbf{a} \tag{2.8}$$

By adding Stokes's theorem 2.14 [14] to the left side of Equation 2.8, Faraday's law in differential form appears [12]. This is the second of Maxwell's equations, Equation 2.2, that is

$$\nabla \times \mathbf{E} = -\frac{\partial \mathbf{B}}{\partial t}.$$

Faraday's law in differential form shows that a changing magnetic field through a stationary conducting loop with a constant cross-sectional area will induce an electric field with a curl equal to the negative time rate of the magnetic field [12]. However, for a constant magnetic field ($\partial \mathbf{B}/\partial t = 0$), no electric field is induced. Hence, there is no electromotive force or current induced in the stationary conduction loop either.

2.1.2 Magnetic Fields

A moving charge will produce a magnetic field. In fact, all magnetic phenomena happen because of charges in motion [12]. A test charge q with the velocity $\mathbf{v}$ in a magnetic field $\mathbf{B}$, experiences a magnetic force

$$F_{mag} = q(\mathbf{v} \times \mathbf{B}). \tag{2.9}$$

Equation 2.9 shows that a magnetic field (N/A·m) will exert a force perpendicular to both the magnetic field and the direction of the velocity of the test charge [12]. Magnetic fields always exist as dipoles due to Equation 2.3, and can be described as vector fields, where north is the origin of the field lines (see Figure 2.1). The strength of the magnetic field depends on the current of charges and is measured in Tesla (T). Typical field strengths of the main magnetic field in clinical MR scanners are 1.5 T and 3.0 T [15].

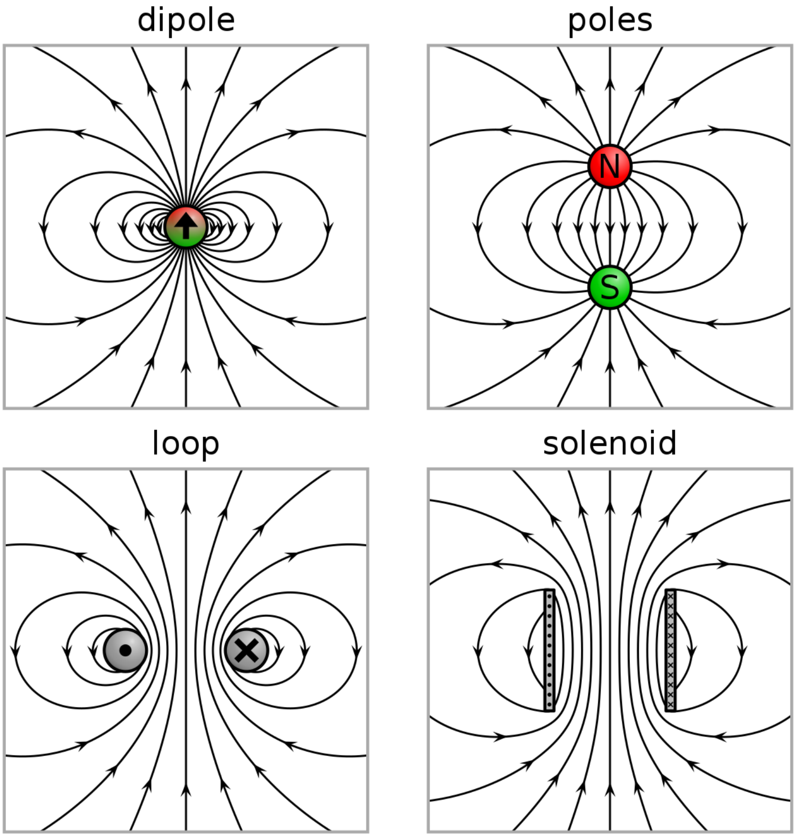

Figure 2.1: *Four types of magnetic dipoles. The magnetic field is described with field lines going from north to south. The figure is taken from [16], licensed under CC BY-SA 4.0.*

On a microscopic scale, magnetic materials consist of orbiting electrons and nuclei spinning about their axes, making up tiny currents. Different types of matter have different susceptibility to becoming magnetised (magnetically polarised) and are categorised into diamagnetic, paramagnetic and ferromagnetic matter [12]. When placed inside a magnetic field **B**, paramagnetic matter has a positive susceptibility and acquire a magnetisation parallel to **B**. In contrast, diamagnetic material has a negative susceptibility and acquire a magnetisation that aligns opposite to **B**. Ferromagnets remain magnetic after removing the external magnetic field [12]. Most organic material (hydrogen, carbon) have diamagnetic susceptibility [15]. In MRI, the magnetic properties of hydrogen are utilised.

2.1.3 Electric Fields

Coulomb's Law

The force **F** on a positive test charge Q due to a source point charge q at rest at a distance r away from the test charge is described by Coulomb's law 2.10 [12].

$$\mathbf{F} = \frac{1}{4\pi\varepsilon_0}\frac{qQ}{r^2}\hat{\mathbf{r}} \tag{2.10}$$

The vector $\hat{\mathbf{r}}$ points in the direction from the source charge to the test charge, and ε_0 is the permittivity constant of free space. If the signs of the charges are equal, the force repels, and if the signs of the charges are unequal, the force attracts. For several point charges, the superposition principle tells that the net force on a test charge is the vector sum of the forces from all source charges individually (see Equation 2.11),

$$\mathbf{F} = \mathbf{F_1} + \mathbf{F_2} + ... + \mathbf{F_n}, \tag{2.11}$$

where n is the number of source charges [12]. The electrical force per unit charge exerted on a test charge Q placed at the location $\mathbf{r}$ is called the electric field $\mathbf{E}(\mathbf{r})$. Since $\mathbf{E}(\mathbf{r}) = \mathbf{F}/Q$, an expression of the electric field can be derived from Coulomb's law (2.10) together with Equation 2.11. The electric field at location $\mathbf{r}$ is given by Equation 2.12 [12].

$$\mathbf{E}(\mathbf{r}) = \frac{1}{4\pi\varepsilon_0}\sum_{i=1}^{n}\frac{q_i}{{r_i}^2}\hat{\mathbf{r}}_\mathbf{i} \tag{2.12}$$

Equation 2.12 shows that $\mathbf{E}(\mathbf{r})$ is a vector that depends on the location of a test charge $\mathbf{r}$ in regard to the source charges. Furthermore, the strength of the field decreases with the square of the separation distance r_i [12]. Electric field lines are used to visualise the electric field of source charges. Electric field lines point away from positive source charges and towards negative charges, where the density of the field lines indicate the strength or magnitude of the electric field (see Figure 2.2). The lines from a source charge always terminate on an oppositely charged source or extend towards infinity [12].

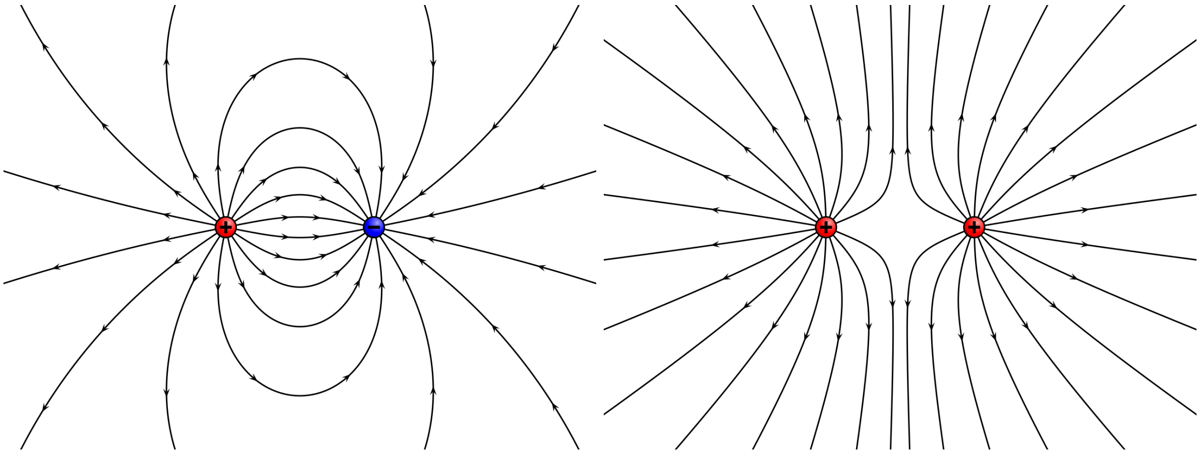

***(a)** Electric field lines for opposite charges.* ***(b)** Electric field lines for two positive charges.*

***Figure 2.2:** Electric field lines for opposite charges is taken from [17], licensed under CC BY-SA 3.0. Electric field lines for equal charges is taken from [18], licensed under CC BY-SA 4.0.*

Curl of an Electric Field

In electrostatics, the electric field is a vector function with no curl (in electrodynamics, this is not true and is explained by Maxwell's equations). Any vector field with a curl equal to zero can be written as a gradient of a scalar potential (see Equation 2.13) [12].

$$\nabla \times \mathbf{E} = 0 \Leftrightarrow \mathbf{E} = -\nabla V, \tag{2.13}$$

where V is the electric potential. Equation 2.13 can be proved by Stokes's theorem 2.14, that says

$$\iint \nabla \times \mathbf{E} \cdot \hat{\mathbf{N}} dS = \oint \mathbf{E} \cdot d\mathbf{l}. \tag{2.14}$$

In Stokes's theorem 2.14, $\hat{\mathbf{N}}$ is a unit vector normal to the smooth oriented surface S and $d\mathbf{l}$ is an infinitesimal change in the path of the smooth (or piece wise smooth) boundary curve of surface S. In spherical coordinates this infinitesimal change $d\mathbf{l} = dr\hat{\mathbf{r}} + rd\theta\hat{\theta} + rsin(\theta)d\phi\hat{\phi}$ (see Figure 2.3) [14]. From the definition of $d\mathbf{l}$ in spherical coordinates, it follows that the dot product of $\mathbf{E}$ and $d\mathbf{l}$ for one point source charge q is

$$\mathbf{E} \cdot d\mathbf{l} = \frac{1}{4\pi\varepsilon_0}\frac{q}{r^2}dr.$$

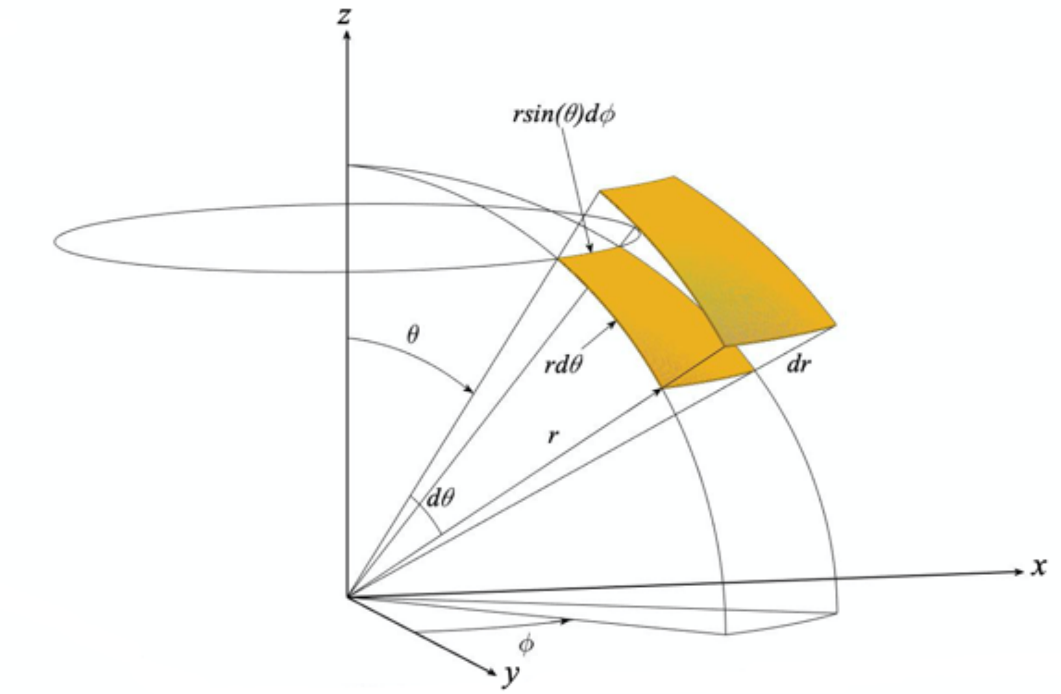

Figure 2.3: The components of the infinitesimal change $d\mathbf{l}$ *in spherical coordinates.* $d\mathbf{l} = dr\hat{\mathbf{r}} + rd\theta\hat{\boldsymbol{\theta}} + rsin(\theta)d\phi\hat{\boldsymbol{\phi}}$.

If r_a and r_b respectively are the distances from the origin to **a** and **b**, the line integral from **a** to **b** is

$$\int_a^b \mathbf{E} \cdot d\mathbf{l} = \frac{1}{4\pi\varepsilon_0} \int_a^b \frac{q}{r^2} dr = \frac{1}{4\pi\varepsilon_0} \left(\frac{q}{r_a} - \frac{q}{r_b} \right). \tag{2.15}$$

For a closed line integral $\mathbf{a} = \mathbf{b}$. Hence, by looking at Equation 2.15 it is clear that the closed line integral $\oint \mathbf{E} \cdot d\mathbf{l}$ is zero, which shows that the line integral from **a** to **b** needs to be independent of path. This is also true for many source charges by the superposition principle [12]. Stokes's theorem 2.14 then says that

$$\iint \nabla \times \mathbf{E} \cdot \hat{\mathbf{N}} dS = \oint \mathbf{E} \cdot d\mathbf{l} = 0,$$

which means that the curl of **E** must be zero. Hence, the left side of Equation 2.13 it true and **E** is the gradient of V [12].

Electric Potential

The electric potential or voltage V at a point $\mathbf{r}$ equals the amount of work needed for the electric force to move a unit charge from a reference point $\mathbf{r_0}$ to $\mathbf{r}$ in an electric field [13], and can be written as

$$V(\mathbf{r}) = -\int_{\mathbf{r_0}}^{\mathbf{r}} \mathbf{E} \cdot d\mathbf{l}. \tag{2.16}$$

From the definition of V from Equation 2.16 it follows that the potential difference between $\mathbf{a}$ and $\mathbf{b}$ is

$$V(\mathbf{b}) - V(\mathbf{a}) = -\int_{\mathbf{r_0}}^{\mathbf{b}} \mathbf{E} \cdot d\mathbf{l} + \int_{\mathbf{r_0}}^{\mathbf{a}} \mathbf{E} \cdot d\mathbf{l} = -\int_{\mathbf{a}}^{\mathbf{r_0}} \mathbf{E} \cdot d\mathbf{l} - \int_{\mathbf{r_0}}^{\mathbf{b}} \mathbf{E} \cdot d\mathbf{l} = -\int_{\mathbf{a}}^{\mathbf{b}} \mathbf{E} \cdot d\mathbf{l}. \tag{2.17}$$

The fundamental theorem of gradients states that

$$V(\mathbf{b}) - V(\mathbf{a}) = -\int_{\mathbf{a}}^{\mathbf{b}} \nabla V \cdot d\mathbf{l}. \tag{2.18}$$

Equation 2.18 is true for all points of $\mathbf{a}$ and $\mathbf{b}$ [12]. Therefore the integrands from Equation 2.17 and Equation 2.18 must be equal and leads to Equation 2.19.

$$\mathbf{E} = -\nabla V \tag{2.19}$$

This again proves the right side of Equation 2.13 [12]. It is convenient to have $\mathbf{E}$ expressed as a function of V since it is often easier to find V first and then calculate $\mathbf{E}$. As earlier mentioned, the electric field is equal to the force per unit charge. Therefore, Equation 2.11 divided by Q shows that the electric field also follows the superposition principle.

$$\mathbf{E} = \mathbf{E_1} + \mathbf{E_2} + ... + \mathbf{E_n} \tag{2.20}$$

If Equation 2.20 is integrated once more from a reference point to $\mathbf{r}$, it follows that the electric potential V, too, obeys the superposition principle (see Equation 2.21).

$$V = V_1 + V_2 + ... + V_n \tag{2.21}$$

Divergence of an Electric Field

Regarding finding V, it can be helpful to know the divergence of **E**. This can be done by going the way around Gauss's law 2.22, which states that

$$\oint \mathbf{E} \cdot d\mathbf{a} = \frac{Q_{enc}}{\varepsilon_0}, \tag{2.22}$$

where Q_{enc} is the total charge enclosed by a Gaussian surface [12]. Equation 2.22 tells that the total flux of **E** through a closed surface is equal to the total charge inside that surface divided by the permittivity of free space. By applying The Divergence Theorem 2.23 (Gauss's Theorem) [14] a surface integral of **E** can be transformed into a volume integral of the divergence of **E**,

$$\oint_S \mathbf{E} \cdot d\mathbf{a} = \int_V (\nabla \cdot \mathbf{E}) d\tau. \tag{2.23}$$

Equation 2.22 and Equation 2.23 together with the total enclosed charge rewritten into charge density ρ,

$$Q_{enc} = \int_V \rho d\tau,$$

gives Gauss's law in differential form [12], Equation 2.1, that is

$$\nabla \cdot \mathbf{E} = \frac{\rho}{\varepsilon_0}.$$

Furthermore, we know that **E** can be written as the gradient of V (see Equation 2.19), hence the divergence of **E** can be written as the Laplacian ∇^2 of V [12].

$$\nabla \cdot \mathbf{E} = \nabla \cdot (-\nabla V) = -\nabla^2 V = \frac{\rho}{\varepsilon_0} \tag{2.24}$$

Equation 2.24 leads to Poisson's equation 2.25 [12].

$$\nabla^2 V = -\frac{\rho}{\varepsilon_0} \tag{2.25}$$

In some cases, it is desirable to find the electric potential in a place where there are no charges ($\rho = 0$). When charge density is zero, Poisson's equation becomes Laplace's equation 2.26 [12].

$$\nabla^2 V = 0 \tag{2.26}$$

To make a current flow from one electrode to another, one needs to apply electromagnetic force on the charges. If the velocity of the charges is sufficiently low, the magnetic force can be ignored, and the current density **J** is proportional to the electric field **E** [12].

$$\mathbf{J} = \sigma \mathbf{E} \tag{2.27}$$

Equation 2.27 is a special case of Ohm's law (commonly written as $V = IR$). It shows that the current density depends on the conductivity of the medium and the electric field that drives the current through it. Hence, the divergence of **J** can be written as a function of the electric field, which further can be expressed in terms of the electric potential. In the case with uniform conductivity and a steady current (the current does not change with time) [12],

$$\nabla \cdot \mathbf{J} = \nabla \cdot (\sigma \mathbf{E}) = \nabla \cdot (\sigma \nabla V) = \sigma \nabla^2 V = 0.$$

As a consequence of Equation 2.19, the divergence of **J** is the conductivity multiplied with Laplace's equation 2.26. This is a partial differential equation (see Equation 2.28),

$$\sigma \nabla^2 V = \sigma \left(\frac{\partial^2 V}{\partial x^2} + \frac{\partial^2 V}{\partial y^2} + \frac{\partial^2 V}{\partial z^2} \right) = 0, \tag{2.28}$$

that can be solved for electric potential with boundary conditions. When V is found, **E** can simply be determined by calculating the gradient of V (Equation 2.19).

In the work with this thesis, a program called Realistic vOlumetric-Approach-based simulator for Transcranial Electric Stimulation (ROAST) was used for simulation of the electric field generated by ECT treatment. ROAST solves Equation 2.28 for each vertex in a volume conductor model of a head with Neumann boundary conditions [19]. By using this quasistatic approximation of Maxwell's equations, one ignores tissue capacitance and assumes that the head tissue is purely resistive [20].

2.1.4 Electrical Conductivity of Tissue

The electrical conductivity of a material is its ability to conduct electricity. The electrical conductivity varies from each material and is inversely proportional to the resistivity of the material (Equation 2.29), and has the unit Siemens per meter (S/m). Thus, a perfect conductor would have a conductivity $\sigma = \infty$, while a perfect insulator would have a conductivity $\sigma = 0$. In most cases, metals are considered perfect conductors [12].

$$\text{Conductivity} = \frac{1}{\text{Resistivity}} \tag{2.29}$$

Poorly conducting materials are called resistors, and the conductivity of the material in a cylindrical resistor can be calculated by

$$\sigma = \frac{L}{RA} = \frac{LI}{AV} = \frac{LJ}{V}, \tag{2.30}$$

if the potential is constant over both ends. In Equation 2.30 L is the length, A is the cross-sectional area, R is the resistance [Ω], V is the potential difference between the ends, and J is the current density [12]. In volume conductor models, like multiple spherical shells, Boundary Element Model (BEM) and Finite Element Model (FEM), tissue conductivities must be accurate. This is necessary to properly model how the current travels and spreads out, and to prevent significant errors in determining the electric potential and electric field distribution. For conductor models of the head, tissue conductivities are often based on earlier literature. However, reported measurements on head tissue conductivity from different literature are not consistent [21]. Table 2.1 shows some examples of typical tissue conductivities.

In Table 2.1, a conductivity constant of 0.010 S/m is assigned to the skull tissue. The human skull is actually an inhomogeneous structure that consists of three layers. Seen in Figure 2.4, the inner and outer layer consists of compact bone (skull compacta), while the middle layer is made out of spongy bone (skull spongiosa) [22][23]. The conductivities of these three layers are significantly different from each other. The conductivity of the spongy middle layer is three to six times the conductivity of the compact bone surrounding it [22]. At the same time, it has been demonstrated that an anisotropic three-layer model does not significantly perform better than an isotropic single-layer model if the conductivity used in the single-layer model is optimal. This optimal conductivity should, to a large extent, be equivalent to the radial conductivity of the three-layered skull [24].

Table 2.1: *Conductivity of head tissue and other materials. These are the values used in ROAST [19] which are based on research from Wagner et al. [25] and Datta et al. [26].*

	Conductivity σ [S/m]
Grey matter, GM	0.276
White matter, WM	0.126
Cerebrospinal fluid, CSF	1.65
Skull	0.010
Scalp	0.465
Air	$2.5 \cdot 10^{-14}$
Gel	0.3
Electrode	$5.9 \cdot 10^{7}$

Furthermore, the conductivity of the whole skull has also been discovered to increase with the current frequency and suggested to vary with age [21]. Skull thickness tends to increase with age, where the inner and outer layer are thought to grow thicker, while the middle layer gets thinner. Consequently, the conductivity of the whole skull decreases with age. If the spongy middle bone was to increase and the compact bone layers got thinner with age, increased skull conductivity would be expected [21]. Additionally, unclosed sutures in the skull make up a path of not yet ossified tissue (more ions and water than in fully ossified bone) with high conductance. The sutures close with age and therefore leads to higher skull conductivity for younger people [21].

Like the skull conductivity, white matter (WM) conductivity is also shown to be anisotropic. The anisotropic conductivity of WM has a strong relationship with diffusion tensors and can be described by dividing it into conductivity parallel or perpendicular to WM nerve fiber tracts [21]. Conductivity parallel to the nerve fibers is greater or equal to the conductivity perpendicular to the nerve fibers ($\sigma_{WM_{\parallel}} \geq \sigma_{WM_{\perp}}$) [27]. By Equation 2.27, this corresponds to a higher electric field strength for currents travelling transverse to the WM fiber tracts. Treating WM conductivity as isotropic can result in significant errors in the electric field strength values in specific ROIs [27]. WM in the brain consists of myelinated axons (fiber tracts) that connect different regions of grey matter. Grey matter (GM) contains the nerve cell bodies, unmyelinated

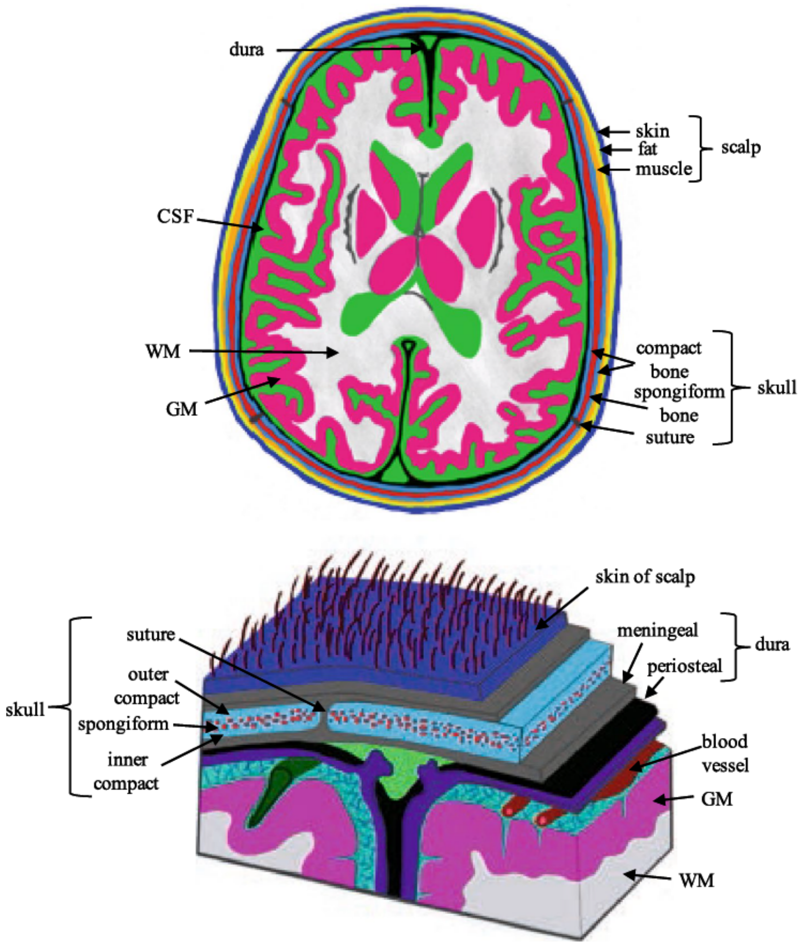

Figure 2.4: *"Figure displaying the various tissue compartments of the head and a subfigure of the detailed layers of the scalp, skull and brain", taken from McCann et al. [21] with permission.*

axons, dendrites and synapses where the signal transmission from one nerve cell to another occurs. GM conductivity is also anisotropic, but the anisotropy is lower compared to WM conductivity [21].

In Table 2.1, the scalp has an electric conductivity of 0.465 S/m. The scalp is not a homogeneous tissue but consists of multiple soft tissue layers like skin, subcutaneous fat and muscle tissue, which have different characteristics. Compared to fat and skin, muscle tissue has a high anisotropic conductivity. In the direction perpendicular to the muscle fibers, it is a lousy conductor in contrast to the parallel direction. By comparing skin, fat and muscle tissue, the skin has the highest conductivity, followed by muscle tissue and fat [28]. Fat has a significantly lower conductivity than both skin and muscle tissue and acts like an insulator. Not surprisingly, a thicker layer of subcutaneous fat leads to greater resistance, meaning a lower conductivity of the scalp [29]. In a recent study from our group in Bergen, a correlation between the estimated thickness of the cranial subcutaneous fat layer and BMI was discovered. The thickness estimates were calculated by segmenting T1-weighted structural MRIs with an open-source software (https://git.app.uib.no/bergen-fmri/fatlas). Pearson correlation values of 0.39, 0.29 and 0.19 were found for three different cohorts [30]. This indicates that individual variation in BMI can cause variation in cranial subcutaneous tissue thickness, leading to individual scalp conductivity.

Cerebrospinal fluid (CSF) lies between the skull and the brain in what is called the subarachnoid space and in the ventricles found inside the brain (see Figure 2.4) [31]. As seen in Table 2.1, CSF is a highly conducting fluid. Hence, if current enters the CSF, it can be passed on to large parts of the brain. In addition, cranial CSF has shown to expand with age, especially the extra-ventricular CSF [32].

As seen in subsection 2.1.3, the electric field depends on the conductivity of the medium it goes through. Individual differences in the electric field that actually is transmitted through the brain tissue during ECT are thus complex, far more complex than just adjusting for age alone. This could potentially result in large individual variations in applied treatment.

2.2 Magnetic Resonance Imaging

Magnetic Resonance Imaging (MRI) is a powerful diagnostic tool that uses magnetic fields and radio-frequency (RF) signals to construct images of the anatomy. It utilises a fundamental property of atomic nuclei called spin [33].

2.2.1 Basic Principles About MRI

Spin, Magnetic Moment and Energy Levels

Nuclear spin is an intrinsic property of an atom that depends on the composition of the nucleons in an atom. An atomic nucleus needs to have an odd number of protons and/or neutrons to possess spin and be NMR (Nuclear Magnetic Resonance) sensitive [33]. Both protons and neutrons are spin-$\frac{1}{2}$ particles. A spinning particle has a magnetic moment [34]. Consequently, a particle with spin will act as a small dipole magnet (see Figure 2.5), where its magnetic momentum $\overrightarrow{\mu}$ is proportional to the total angular momentum $\overrightarrow{J}$. The magnetic momentum $\overrightarrow{\mu}$ is defined by Equation 2.31.

$$\overrightarrow{\mu} = \gamma \overrightarrow{J} \tag{2.31}$$

In Equation 2.31 γ is the gyromagnetic ratio measured in MHz/T. The gyro-magnetic ratio is a constant that shows the relationship between the angular momentum and the magnetic moment for each NMR sensitive atom. The hydrogen nucleus has the highest gyromagnetic ratio of all nuclei, with a value of 42.57 MHz/T [33][15]. In addition to having the highest γ, thus the strongest magnetic properties, hydrogen is also the most abundant atom in a human body. In an MRI voxel of human tissue ($1\,\mathrm{mm}^3$) there is around 10^{18} protons coming from hydrogen atoms in water and fat molecules [15]. The most common isotope of hydrogen is protium, ^{1}H, with an abundance of more than 99.98 % [34]. These are the reasons why ^{1}H give the strongest MR signal and is mostly used for MRI, even though all particles with a net spin theoretically could be used [15].

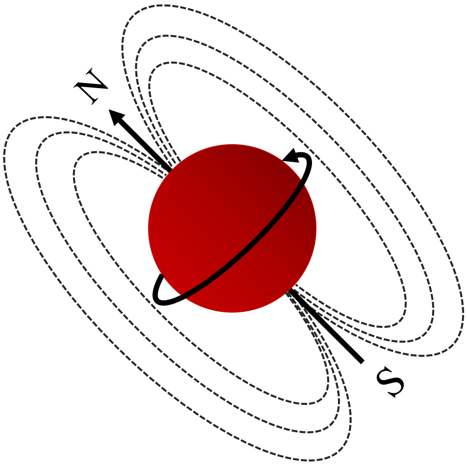

Figure 2.5: A spinning hydrogen nucleus with a magnetic moment (arrow through the nucleus) will act like a dipole magnet with a north (N) and a south (S) pole.

The net magnetisation $\overrightarrow{M}$ of a sample of spin particles is given by Equation 2.32,

$$\overrightarrow{M} = \sum_{i=1}^{N_s} \overrightarrow{\mu} \tag{2.32}$$

where N_s is the number of spins in the sample [15]. The magnetic moment $\overrightarrow{\mu}$ of a particle is randomly oriented unless it is exposed by an external field B_0. Therefore, the net magnetisation of a sample of protons will be equal to zero when placed outside a magnetic field (see the left side of Figure 2.6) [33].

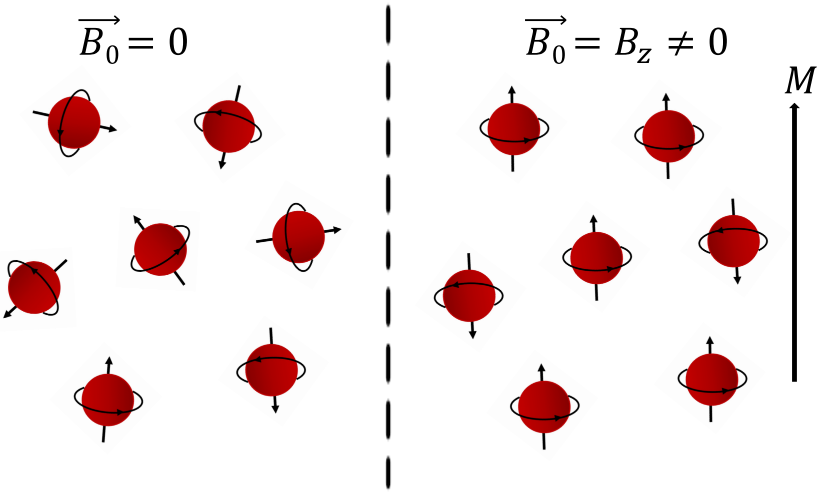

Figure 2.6: To the left: Magnetic moments of hydrogen nuclei randomly align when no external field is applied. To the right: Alignment of magnetic moments of hydrogen nuclei when an external field $\overrightarrow{B_0}$ is applied. This leads to a positive net magnetisation $\overrightarrow{M}$ in the direction of the magnetic field.

When a sample of protons (^{1}H) is placed inside a magnetic field $\overrightarrow{B_0}$ some of the hydrogen nuclei will be aligned parallel to the field direction, while a smaller number of nuclei will align anti-parallel to the field direction (Zeeman splitting) [33]. This leads to the net magnetisation of the sample being positive (see Equation 2.33 and Figure 2.6 and 2.7) [15][33].

$$\overrightarrow{M} = \sum_{i=1}^{N_s} \overrightarrow{\mu} > 0 \tag{2.33}$$

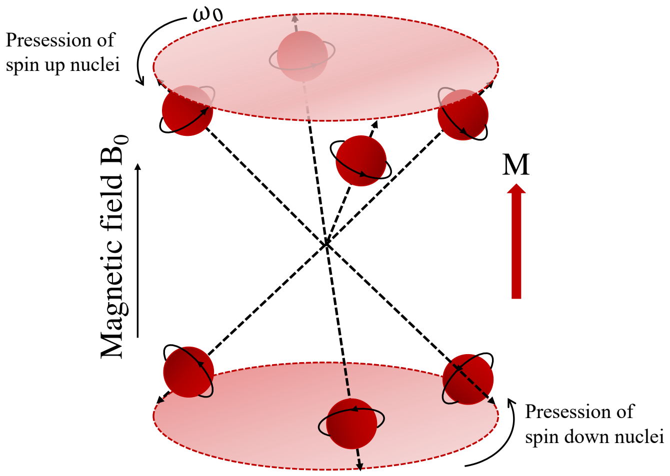

Figure 2.7: *Precession of spin up and spin down nuclei of a sample in the magnetic field $\overrightarrow{B_0}$. All precess in a circular path around $\overrightarrow{B_0}$ with Larmor frequency ω_0. There is a positive net magnetisation $\overrightarrow{M}$.*

The two orientations (parallel or anti-parallel) give rise to two possible energy states, where the magnetic moment in the direction of B_0 for both states can be described by Equation 2.34. A positive sign means pointing in the direction of the field [15].

$$\overrightarrow{\mu_z} = \pm\frac{1}{2}\gamma\hbar \tag{2.34}$$

The ratio of the number of protons with spin up and down can be described by the statistical Boltzmann distribution 2.35.

$$\frac{N_\uparrow}{N_\downarrow} \approx e^{\frac{\Delta E}{kT_s}} \tag{2.35}$$

$N_\downarrow$ is the number of spins down, $N_\uparrow$ is the number of spins up, T_s is the temperature of the sample, k is the Boltzmann constant ($1.38 \cdot 10^{-23}$J/Kelvin) and ΔE is the energy difference between these two states (spin up and spin down). $E_\downarrow$ is the higher energy state (Equation 2.36) for protons opposing B_0 and $E_\uparrow$ is the lower energy state (Equation 2.37) [15].

$$E_\downarrow = \frac{1}{2}\gamma\hbar B_0 \tag{2.36}$$

$$E_\uparrow = -\frac{1}{2}\gamma\hbar B_0 \tag{2.37}$$

Like earlier mentioned, there is always an excess of spins in the lower energy state $E_\uparrow$. Equation 2.38 describes the energy difference ΔE between the higher and lower energy state,

$$\Delta E = E_\downarrow - E_\uparrow = \gamma\hbar B_0, \tag{2.38}$$

where $\hbar$ is the reduced Planck constant ($1.05 \cdot 10^{-34}$ J·s) [15]. Equation 2.38 shows that the energy difference between the lower and higher energy state depends on the applied magnetic field (this is visualised in Figure 2.8). For a nucleus, it would therefore take more energy to align opposite to a stronger magnetic field. Nuclei with sufficient thermal energy can align opposite to the external magnetic field. The MR signal therefore strongly depends on temperature and the strength B_0. Low temperature and/or a high magnitude of B_0 makes it hard for nuclei to go to the higher energy state. This leads to a highly positive net magnetisation $\vec{M}$ and a strong signal [33].

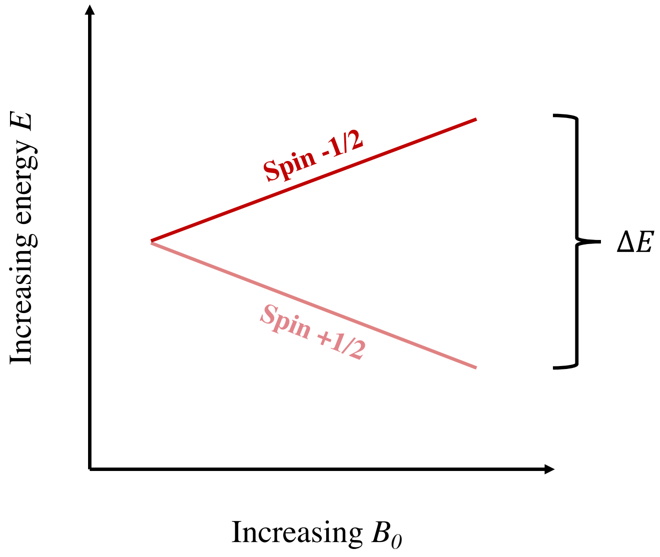

Figure 2.8: Zeeman splitting between spin up (+1/2) and spin down (-1/2), where the energy gap between the energy states is proportional to the B_0

When a proton is placed inside B_0, it does not only spin around its axis but starts precessing around B_0. The speed at which the magnetic moment circulates around B_0 is called the precessional frequency or the Larmor frequency ω_0 since the Larmor equation 2.39 defines the value.

$$\omega_0 = \gamma B_0. \tag{2.39}$$

The Larmor equation 2.39 tells us that the precession of the magnetic moment about B_0 is proportional to the main magnetic field. It is also dependent on the gyro-magnetic ratio, which means that different nuclei will have different Larmor frequencies. The Larmor frequency for a nucleus is also the frequency needed to excite a particle from a lower (spin-up) to a higher energy level (spin-down) [33]. In Figure 2.7, the multiple magnetic moments in a sample precessing around B_0 can be seen. The path they follow is called the precessional path.

If it is assumed that $\Delta E << kT_s$, Boltzmann's distribution 2.35 together with Equation 2.38 can be approximated to

$$\frac{N_\uparrow}{N_\downarrow} \approx 1 + \frac{\gamma \hbar B_0}{kT_s},$$

which leads to Equation 2.40 if it is assumed that $N_s = 2N_\downarrow$ [15].

$$N_\uparrow - N_\downarrow \approx N_s \frac{\gamma \hbar B_0}{2kT_s} \tag{2.40}$$

An expression for the net magnetisation can now be found. Since the precessional path lies in the xy-plane (transverse plane), the net magnetic moment in the x- and y-direction cancels out to zero. The net magnetic moment is therefore in the z-direction.

$$\overrightarrow{M} = M_z \overrightarrow{k} = \left(\sum_{i=1}^{N_s} \overrightarrow{\mu_{z,n}} \right) \overrightarrow{k} \tag{2.41}$$

If $\overrightarrow{\mu_{z,n}}$ is substituted by Equation 2.34

$$\overrightarrow{M} = \left(\sum_{i=1}^{N_\uparrow} \frac{1}{2}\gamma\hbar - \sum_{i=1}^{N_\downarrow} \frac{1}{2}\gamma\hbar \right) \overrightarrow{k} = \frac{1}{2}\left(N_\uparrow - N_\downarrow\right)\gamma\hbar \overrightarrow{k}. \tag{2.42}$$

By finally using the approximation from Equation 2.40 in Equation 2.42, an expression of the net magnetisation is derived and can be seen in Equation 2.43.

$$| \overrightarrow{M} | = \frac{\gamma^2 \hbar^2 N_s B_0}{4kT_s}, \tag{2.43}$$

where γ is the gyromagnetic ratio [MHz/T], $\hbar$ is the reduced Planck constant, N_s is the number of spins in sample, B_0 is strength of main magnetic field [T], k is the Boltzmann constant and T_s is the temperature of the spin system [Kelvin] [15]. Equation 2.43 shows that the magnitude of the net magnetisation, not surprisingly, is proportional to the main magnetic field and inversely proportional to the temperature of the sample.

Resonance and Signal Generation

The second letter in the acronym MRI stands for resonance. Resonance can occur when a nucleus is exposed to an oscillating force with a frequency close to the natural frequency of the nucleus ω_n. When this happens, energy is transferred from the external force to the nucleus [33]. If the frequency of the energy transferred is equal to the Larmor frequency of the nucleus ω_0, resonance will occur, and the absorbed energy from the source will cause the nucleus to be excited. At all field strengths of B_0 used in clinical MRI, the Larmor frequency of hydrogen lies in the radio frequency (RF) band in the electromagnetic spectrum [33]. Consequently, an applied RF pulse of energy with precisely the same frequency as the Larmor frequency of hydrogen would make the hydrogen nuclei resonate (this is clear by combining Equation 2.38 and Equation 2.39). In a sample of hydrogen spins, this would lead to an increase of nuclei with downward spin.

Resonance is the basis of generating signals in MRI. As a result of resonance, $| \overrightarrow{M} |$ rotates away from aligning with the main magnetic field. The angle it moves away with is called the flip angle α, and it is determined by the amplitude and duration of the RF pulse [33]. From now on, the direction of the magnetic field (z-direction) is called longitudinal, and the plane perpendicular to it, the xy-plane, is called the transverse plane. A flip angle of 90° would lead to $\overrightarrow{M}$ being completely transferred into the transverse plane ($\overrightarrow{M} = \overrightarrow{M_{xy}}$). In addition, as long as the RF pulse is on, all the individual magnetic moments move in phase [33]. Hence, the net magnetic moment is in phase (coherent) and precesses in the transverse plane at Larmor frequency. If a conducting coil is placed near the rotating magnetic field, a voltage would be induced in the coil by Faraday's law. This voltage generates the MR signal with Larmor frequency and a magnitude that depends on the amount of transverse magnetisation ($\overrightarrow{M_{xy}}$) [33].

Image Contrast

As soon as the RF pulse is turned off, the net magnetisation starts to dephase and realign with B_0. This happens due to individual magnetic moments releasing energy to the surrounding tissue (spin-lattice relaxation) and interacting with neighbouring magnetic nuclei (spin-spin relaxation). The recovery of the longitudinal magnetisation $\overrightarrow{M_z}$ is called T1-recovery, whereas the dephasing and loss of transverse magnetisation $\overrightarrow{M_{xy}}$ is called T2 decay [33].

The recovery of the longitudinal magnetisation takes place because of energy transfer to the surrounding lattice. It happens exponentially, where the constant T1 is how long it takes for 63% of the original net magnetisation M_0 to be restored [33]. Equation 2.44 shows the T1-recovery in the longitudinal direction [15].

$$M_z(t) = M_0(1 - e^{-\frac{t}{T1}}) \tag{2.44}$$

By setting time t to $T1$ in Equation 2.44, it is clear why T1 is determined to be 63 % of the longitudinal recovery.

$$M_z(T1) = M_0(1 - e^{-1}) = M_0 \cdot 0.63$$

The loss of transverse magnetisation takes place because of interactions between neighbouring magnetic nuclei. It decays exponentially, where the constant T2 is how long it takes for it only to be 37% of the transverse magnetisation left. Equation 2.45 shows the T2-decay in the transverse plane [15].

$$M_{xy}(t) = M_0 e^{-\frac{t}{T2}} \tag{2.45}$$

T1 and T2 depend on the tissue structure and the surroundings. Water molecules consist of hydrogen and oxygen, where the oxygen atom tends to pull the electrons away from the hydrogen atoms [33]. This is called a deshielding effect and makes the hydrogen nuclei feel a stronger local magnetic field [35]. On the other hand, fat consists of hydrogen connected with carbon that does not pull the electrons away from the nucleus. Hydrogen in fat remains in a cloud of electrons that acts opposite to the magnetic field [33]. Hence, the hydrogen nuclei are shielded. Consequently, the Larmor frequency of hydrogen in fat is lower than in water [35]. Hydrogen in fat also has a faster T1-recover and T2-decay. Different proton densities, in addition to variation in T1 and T2 times for different tissue is what makes the contrasts in MR images. Generally, fat and water give rise to the two contrast extremes in MRIs of the body, due to their different magnetic properties [33]. T1-recovery and T2-decay for water and fat can be seen in Figure 2.9a and Figure 2.9b. Biological tissues typically have $T1 \approx 300 - 2000\,\text{ms}$ and $T2 \approx 30 - 150\,\text{ms}$ [15]. Images used in this thesis have T1 contrast.

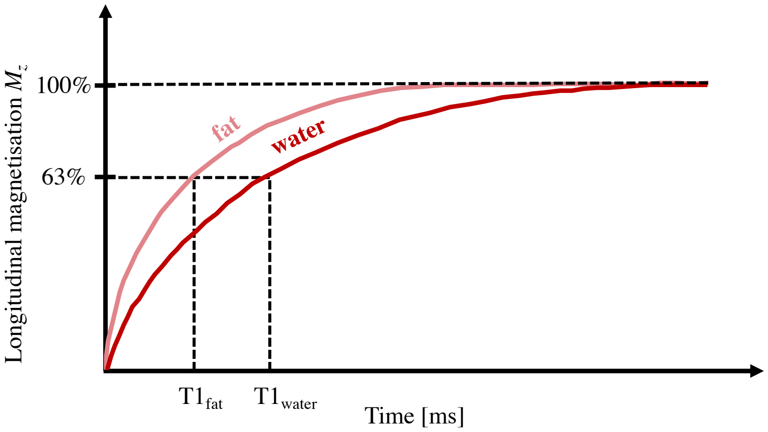

(a) *T1 recovery curves for fat and water*

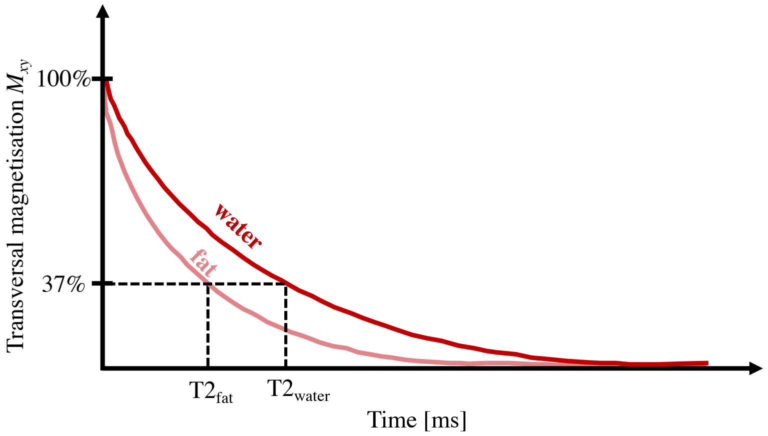

(b) *T2 decay curves for fat and water*

Figure 2.9: *T1 and T2 times for fat and water*

2.2.2 Pulse sequence

Time Parameters and Image Weighting

An MRI image is often said to be T1-weighted, T2-weighted, or proton density weighted. The weighting is determined by the flip angle α and different time parameters, the repetition time (TR), the echo time (TE) and the inversion time (T1), in a pulse sequence [15]. TR is the time between the start of one RF pulse to the start of the next pulse for a slice, while TE is the time from the start of an applied RF pulse to the peak of a signal induced in the receiver coil (see Figure 2.10) [33]. TI is a time between pulses chosen in a sequence to selectively zero out the signal from a tissue of choice [15]. The time it takes to null out the signal from a tissue strongly depends on the ratio between TR and T1 for that tissue.

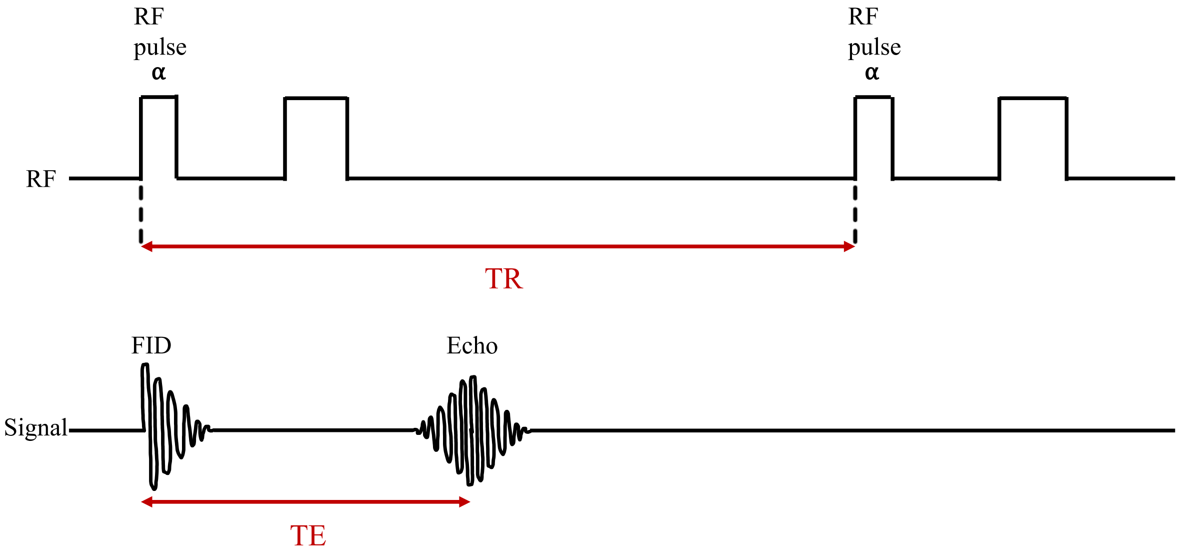

Figure 2.10: The pulse sequence parameters α, TR (repetition time) and TE (echo time).

Specific values of TR and TE is specified for a pulse sequence to get a T1 weighted, T2 weighted, or a proton density weighted MRI image [33]. The TR controls how much T1-recovery that can occur before the next RF pulse is excited, and therefore controls the amount of T1 weighting. For T1 weighting the TR must be short enough, to make sure that both fat and water have not recovered all their longitudinal magnetisation. With a TR too long, there is no contrast between the signal from fat and water [33] (see Figure 2.9a for illustration). A T2 weighted image, on the other hand, is controlled by TE. The TE decides how much T2 decay that can occur before the signal is read. Therefore, a long TE is needed to get a T2 weighted image. If it is too short, neither fat nor water would have had time to decay, and the contrast between the tissues would be too small [33].

To get an image where either the T1, T2 or proton density is weighted, the time parameters must be set so that the effects of the other processes are reduced. For example, for a T1 weighted image, a short TR and a short TE should be used. The short TE is to make sure that only a small amount of transverse decay has happened [33]. As fat have a shorter T1 time than water, fat will have greater longitudinal magnetisation than water after a short time. Hence, fat will have a strong signal and appear bright, while water will have a weak signal and appear dark.

Gradients

Gradients are smaller magnetic fields generated by coils of conducting wire inside the body of the main MR magnet. When currents run through these coils, gradient magnetic fields G are induced due to Faraday's law of induction. In an MRI scanner, gradient coils are placed so that it is possible to create gradient fields in the three orthogonal spatial directions (G_x, G_y, G_z) [15]. Gradient fields are used to locate the MR signal. Because the gradients linearly alter the net magnetic field B along the wanted axis (x, y or z) [33], the Larmor frequency also increases proportionally along that axis (see Equation 2.39). By knowing the slope of the gradient along an axis, the Larmor frequency can be identified [15]. Applying an RF pulse with a specific Larmor frequency would therefore select a slice for the MR signal because the nuclei in that slice would be the only nuclei resonating at that frequency [33]. A gradient in the z-direction G_z is often applied simultaneously as the RF pulse for slice selection.

To further locate the signal in the other two directions, something called phase and frequency encoding is used. By turning on G_x, the net magnetic field alters linearly along the x-axis. Hence, the signal can be located based on frequency differences. This frequency encoding gradient is often applied during signal readout [33].

For the location of the signal on the remaining axis, phase encoding solves the problem. Before the gradient is turned on, the nuclei precess in phase at Larmor frequency. When G_y is turned on for a short period, the phase of the nuclei shifts according to their position. Nuclei experiencing a lower magnetic field will precess at a slower rate and loose phase, while nuclei experiencing a higher magnetic field will precess at a higher rate and gain phase. When G_y is turned off, the nuclei again precess at Larmor frequency but with a phase shift depending on their position in y-direction [33]. The phase encoding gradient is often applied before signal readout. Figure 2.11 shows a simple visualisation of how phase and frequency shift enable localisation of individual signals within a slice.

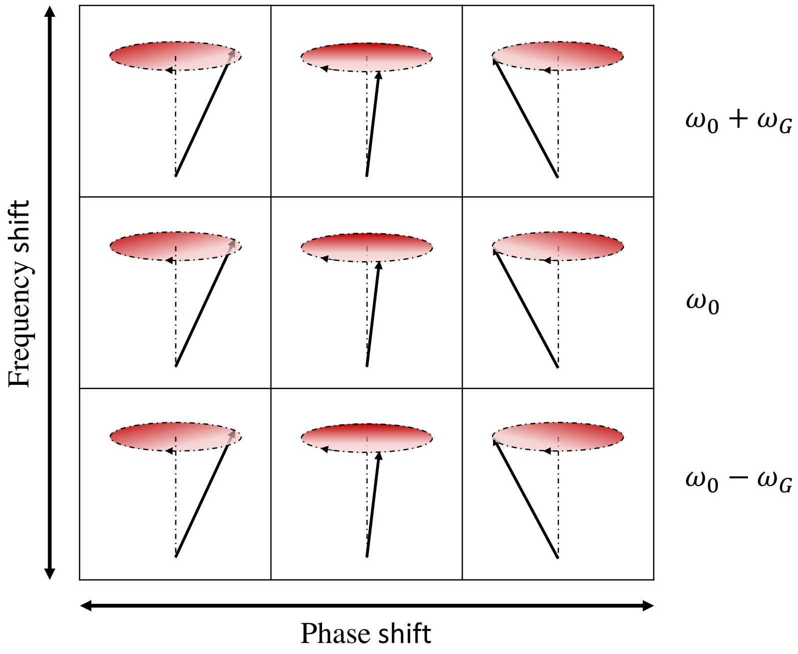

Figure 2.11: *Phase and frequency shift in a slice*

RF Spoiling

RF spoiling is used to disrupt residual transverse magnetisation that may be present from the previous repetition. In this way, only the longitudinal magnetisation component affects the signal. RF spoiled sequences, therefore, often produce good T1 images [33]. RF spoiling is done by adding RF pulses at continuously changing phases. Applying an RF pulse at a specific phase ϕ leads to the net magnetisation flipping to a specific position in the transverse plane [36]. If the first RF pulse is transmitted at ϕ_1, the receiver coil can be locked to only receive RF signal with this phase. When the next RF pulse is transmitted at ϕ_2, the net magnetisation acquires the phase ϕ_2 and the receiver coil only receives RF signal with ϕ_2. By locking the receiver coil to a specific phase, transverse magnetisation at other phases is ignored. Dephasing because of magnetic field inhomogeneity and T2 relaxation can therefore not dominate an RF spoiled image [36]. In this thesis, the T1 weighted images were acquired using MRI sequences with RF spoiling.

2.3 Electroconvulsive Therapy

This section introduces the basics of electroconvulsive therapy (ECT), some history of the treatment and different parameters that influence the efficacy and side effect of ECT.

2.3.1 ECT as a Treatment Against Major Depressive Episodes

ECT is short for electroconvulsive therapy and is mainly used in treatment-resistant severe depression. It works by sending a controlled amount of current through the brain to induce a seizure (getting convulsions) [37], where the seizure normally lasts for 20-90 seconds [10]. A great development of the treatment has happened over the last 80 years. The idea of treating mental illness with convulsion therapy was first proposed by Laszló Meduna, which hypothesised that epilepsy and schizophrenia were antagonistic. This became a theory after discovering that glial cells occupied the spaces left by lost neurons in the brains of patients with epilepsy, while schizophrenia patients had a reduction of glial cells in the brain [38]. In 1938, induced seizures using electrical stimulation of the brain was introduced as a treatment by the neurologist Cerletti and the psychiatrist Bini from Italy. At this time, there were no effective medications for mental disorders. ECT was first used for many mental disorders (such as schizophrenia) but eventually mainly used to treat depressive symptoms [37].

When introducing the treatment method, no anesthesia or muscle relaxants were used. In addition, treatment was often administered without the consent of the patients [37]. These circumstances are what a lot of people associate with ECT and are probably some of the reasons why ECT is thought of as frightening by many people and is surrounded by controversy and stigma. In the 1950s, effective antipsychotics and antidepressants became available, and the use of ECT was gradually reduced and reserved for the most seriously ill patients [37]. Since then, the treatment technique has been significantly improved in such a manner that the side effects are dramatically reduced. This includes the use of anesthesia and muscle relaxants, in addition to the use of consent forms and change of stimulus type and electrode placement.

2.3.2 Currently Discovered Effects and Side Effects of ECT

Not all patients benefit from ECT, but 70-80 % of patients receiving treatment for moderate to severe depressive episodes respond well to the treatment. At the same time, the relapse rate is high. Treatment with antidepressant drugs after an ECT series is therefore often recommended [11].

Due to the possibility of cognitive side effects and heart complications, the need for anesthesia, and the high relapse rate, the use of ECT is limited [27]. Of all the side effects, the cognitive side effects have led to the most concern. For a long time, it has been known that ECT can cause cognitive side effects in the form of impaired ability to create new memories (anterograde amnesia), decreased memory of events in one's own life before ECT (retrograde amnesia for autobiographical memories) and reduced memory of facts one had acquired before ECT (retrograde amnesia for impersonal facts) [11]. However, most studies have shown that anterograde memory problems decrease with time. It is common with memory and concentration difficulties for a few days up to weeks after treatment [37]. Some patients even experience improved ability to concentrate some time after ECT [11]. The effects on retrograde memory after ECT are still unclear [37]. It can be difficult to distinguishing retrograde amnesia caused by ECT or the depression itself from completely normal forgetting [11]. Differentiating between possible cognitive side effects after ECT and cognitive changes related to the mental illness is also challenging [37].

Some years ago, a study was carried out in Sweden to identify the patients who were more likely to experience short-term subjective memory worsening after ECT. It turned out that it is more common in women compared to men and more common for patients between 18 to 39 years to experience subjective memory worsening than patients from 65 years and older. Hence, young women are at high risk [39].

Some possible physical side effects of ECT are headache, nausea, muscle aches and skin burns [10]. Tooth damage is also a possible physical side effect, especially with poor dental status [37]. Mortality due to ECT is in several studies showed to be comparable to minor surgical procedures which involve general anesthesia [11].

There are individual differences concerning the side effects of ECT. While most patients tolerate the treatment well, some patients suffer from memory problems over longer periods and report permanent loss of autobiographical memories [37]. In the following subsections, various parameters that affect the side effects of ECT will be presented. A complete explanation of the physical mechanisms that make the differences is still missing. In subsection 2.3.4, it will be shown that some electrode placements lead to fewer cognitive side effects than others. However, it is not known if this, for example, is due to lower electric field strength in the hippocampus and other regions essential for memory function [27].

2.3.3 Brief Pulse Stimulus

The type of ECT stimulus provided by the different ECT devices has been changed over time. Initially, sine waves were used, but from the beginning of the 80s, the recommendation was to use brief pulse stimulation and stop using sine current [11]. Sine wave stimuli show greater cognitive side effects and are less efficient compared to brief pulse stimuli [10]. Brief pulse stimuli are alternating square waves with pulse widths between 0.5-1.5 ms. They are dominant globally because of the discovery that large pulse widths cause more extensive cognitive side effects [11]. For brief pulse stimuli, the dose needed with shorter pulse widths is shown to be less than with wider pulse widths. Specifically a pulse width of 5 ms is reported to be the most efficient. Another study also says that for a current at 900 mA, a pulse width between 0.25 ms and 0.5 ms is similarly efficient [10].

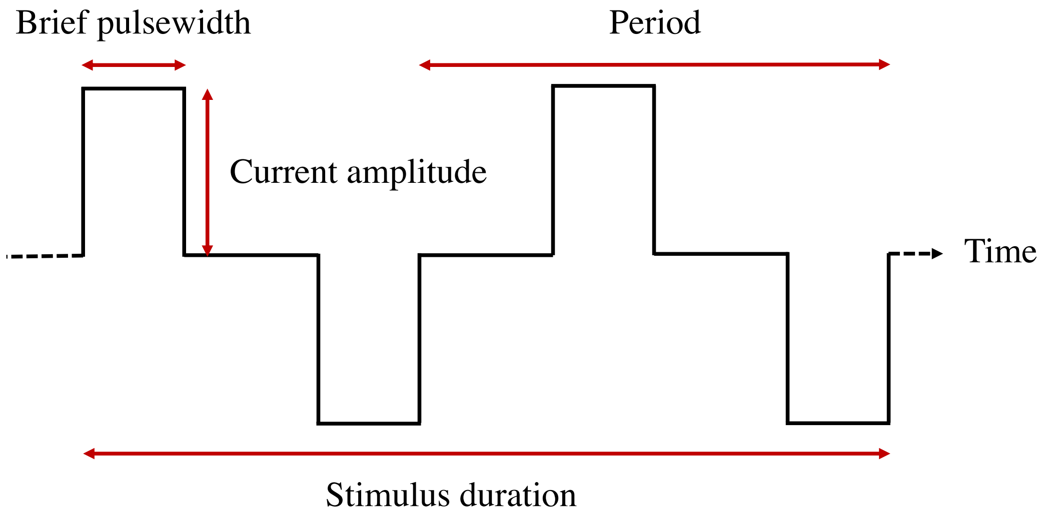

Figure 2.12: Brief pulse stimulus illustration.

In Figure 2.12, an illustration of a brief pulse stimulus is shown. A wave is considered to contain two pulses, one with a positive amplitude and one with a negative amplitude. The frequency f_{pp}, therefore, refers to the number of pulse pairs per second and is equal to 1/period. By multiplying the pulse pair frequency f_{pp} with two, one gets the pulse frequency f. The amplitude of the pulses represents the magnitude of the current i in mA, while the pulse width τ is the time each pulse last in ms. Figure 2.12 clearly shows how the current is constant in a brief pulse stimulus. In this thesis, brief pulse stimulus with current amplitude equal to 900 mA and pulse widths between 0.25-1.00 ms was used.

2.3.4 Electrode Placement

In modern ECT, different electrode placements are used. Efficacy and side effects of ECT are affected by electrode placement. The most common placements are bitemporal (BT), right unilateral (RUL) and bifrontal (BF) placement [11]. These three electrode placements are illustrated in Figure 2.13. Originally, BT was the standard, but RUL was early tried out, primarily to spare memory and language areas of the brain. Unilateral (UL) ECT has now been proved to have less side effects than BT ECT at low stimulus doses but also lower efficacy. At high doses, UL ECT increases in efficacy but also in side effects (same as BT) [10].

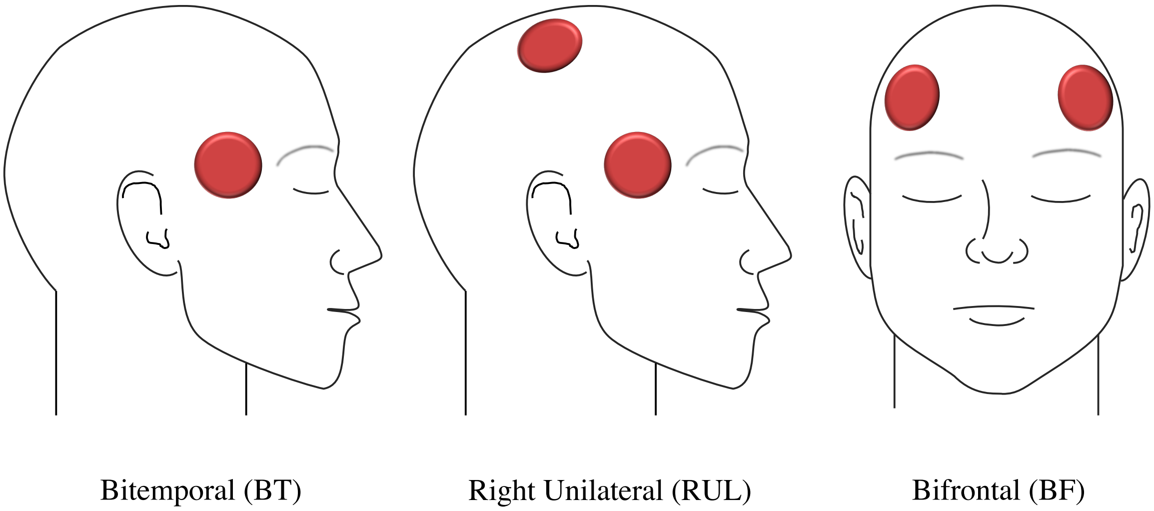

Figure 2.13: Bitemporal, right unilateral and bifrontal electrode placement. Electrodes are illustrated in red.

In Norway, RUL is the preferred electrode placement [11]. RUL electrode placement was used in the current study. With this placement, one electrode is placed just to the right of the highest part of the skull, while the second electrode is placed on a flat area just above the right anterior temporal lobe (this is illustrated in Figure 3.1 in section 3.2).

2.3.5 Dosing

In ECT, current is passed through the brain between two electrodes to trigger a seizure. The amount of charge needed to trigger a seizure is called the seizure threshold [11]. Stimulation without subsequent seizures has been thought to be ineffective. The amount of charge, from now on called dose, is therefore important for the treatment effect of ECT. The choice of a dose is controlled by two factors: the presumed antidepressant effect and the risk of cognitive side effects. Previous findings indicate that doses given just above the seizure threshold at the RUL placement were less effective than doses significantly above the seizure threshold [11]. It is recommended not to use a dose more than 5-6 times the seizure threshold, even though no documentation says that high doses cause more cognitive side effects in the long run. The seizure thresholds decrease with smaller pulse width and RUL placement compared to BT. Furthermore, men have higher seizure thresholds than women, and older people seem to have higher seizure threshold than younger people at group level [11]. Research done as early as in 1987 by Sackeim et al. found sex differences in seizure threshold, and showed that male patients on average needed a dose 158.34 % of what female patient needed to elicit a seizure [40]. However, correcting for sex differences in seizure threshold is not the standard procedure when determining the dose.

The stimulus dose Q is measured in mC (mA·s) and can be calculated with Equation 2.46.

$$Q = i \cdot \tau \cdot f \cdot t_{dur} \tag{2.46}$$

where i is the current, τ is the pulse width, f is the pulse frequency (two times pulse pair frequency f_{pp}) and t_{dur} is the total stimulus duration in seconds [20]. Defining charge as the ECT dose is widely used in clinical practice and research studies. However, some people think that defining it by the individual stimulus parameters and shape should be done instead to reduce the risk of not seeing their distinct roles [20].

To find an adequate stimulus dose, it is common to either use an age-based formula or use seizure threshold titration, i.e. stimulate the brain several times with ascending charge in the same anesthesia until there is an adequate seizure [37]. In Norwegian practice, age-based dose calculations are most common. Internationally, the method used is more variable [11]. In the current thesis, an age-based method was used to determine the treatment stimulus dose Q. This method primarily calculates the individual percentage energy $E[\%]$ with Equation 2.47,

$$E[\%] \simeq \text{Patient's age in years,} \tag{2.47}$$

before calculating the treatment dose by Equation 2.48. The stimulus energy E_{stim} is E corrected for sex-specific differences in seizure threshold (adding some percentages to male patients and subtracting some percentages from the dose for female patients).

$$Q \simeq E_{stim} \cdot Q_{max} \tag{2.48}$$

In Equation 2.48, Q_{max} is the maximum charge the ECT device can deliver. Q_{max} for a Thymatron System IV that was used in this study is 504 mC.

2.4 Status of Knowledge in the Research Field

Over the last twenty years, there has been a growing interest in using neuroimaging (brain imaging) to investigate how ECT affects brain structure and function. There now seems to be a great deal of agreement between studies that documents structural and functional changes in the brain as a consequence of ECT [5][6][41][42]. Studies particularly report significant changes in the hippocampus [7][43][44]. Volumetric changes in the hippocampus are therefore being carefully examined, both as a whole structure and divided into subfields. Hippocampus is a brain structure that is important for memory function and learning, and relative to controls, patients with depression is associated with reduced hippocampal volumes [45].

Most neuroimaging studies of ECT demonstrate volume increase of the hippocampus, but how the changes relate to outcome still remains unclear. Single studies have been inconsistent, saying the changes relate and not relate to clinical improvement, and saying increased volume changes may correspond to cognitive side effects [8] and may not [9]. The main reason for this inconsistency is probably that single studies have a limited number of samples and therefore lack statistical power. In larger GEMRIC studies (n=281 and n=328), they found no significant link between hippocampal enlargements and positive clinical outcome [7][5]. It was also found that patients with the worst outcome had the largest increases in hippocampal volume.

However, the hippocampus is not uniform but contains multiple subfields with different functionalities. When studied as a non-uniform structure, different hippocampal subfield is assumed to play different roles in ECT. It is suggested that volume changes in different subfields of the hippocampus may be biomarkers for ECT response [46], and that more focused targeting of hippocampal subregions maybe could improve ECT outcome [9].

Hippocampus is a brain region known to contain neural stem cells [47]. A hypothesis is that adult neurogenesis (new neurons are formed) is impaired during depressive episodes [48], and that ECT increases neurogenesis in the dentate gyrus of the hippocampus [49]. An increase of the dentate gyrus would therefore be expected after ECT. In a small sample study, a large and significant volume increase in the dentate gyrus was observed after ECT [50]. This was done by segmenting images from a 7-tesla MR scanner (high resolution). Increased volume in the dentate gyrus also showed a positive relation with clinical improvement in this study.

Ultra high resolution images, in combination with recently developed programs for segmentation of hippocampal subfields, enable studying the changes that occur during ECT at a much more detailed level.

2.5 Thesis Aims and Motivation

Since the electric field strength has been shown to have a strong correlation with volume change in various brain structures in a dose-dependent way, it is important to understand what affects the applied electric field and how the electric field interacts with the brain tissue in order to explain the underlying mechanisms of ECT treatment effects and side effects. Thus, the main aims of the current thesis are to:

- Quantify the volumetric changes of the hippocampus after ECT treatment with respect to the applied electric field strength and dose.
- Characterise variations in volume change and electric field strength across individuals with an emphasis on differences in BMI, age, sex, number of ECT sessions and intracranial volume.
- Characterise volumetric and electric field strength variations in different brain structures.

The main tasks in this thesis includes handling and processing local data from Bergen (40 patients) in order to quantify the volumetric changes of the hippocampus after ECT by the use of an established processing pipeline (FreeSurfer 7.1.1) [51]. Furthermore, the work includes simulating the electric field generated by the ECT stimulus in the hippocampi using the software Realistic vOlumetric-Approach-based Simulator for Transcranial electric stimulation (ROAST 3.0) [19]. Moreover, statistical analysis are performed in RStudio [52] to investigate the relationships between the electric field strength, volume change and dose, in addition to possible individual differences due to BMI, age, sex, number of ECT sessions and intracranial volume.

With this work, I hope to contribute to a better understanding of the relationship between dose, electric fields and volume changes in ECT, which hopefully will contribute to the development of a more personalised dosage and effective treatment in the future, with minimal side effects.

Chapter 3

Methods

In the current chapter, study participants, study design, data acquisition and analysis is described.

3.1 Study Participants

The data in the current thesis stem from an observational study on ECT treatment in patients suffering from major depressive episodes, Table 3.1. A total of forty patients received routine ECT treatment at the Haukeland University Hospital, Bergen, Norway. These patients received ECT as a treatment for moderate or severe symptoms of depression. Montgomery and Åsberg Depression Rating Scale (MADRS) is used to determine the extent and severity of some of the most commonly occurring symptoms of depression [53]. A MADRS score ≥ 25 was a threshold for participating in the study. Only patients over 18 years were included. An exclusion criterion was that the patient could not have had ECT treatment during the last 12 months. More detailed descriptions of the inclusion and exclusion criteria for participation can be found in the study protocol [54].

Table 3.1: *Distribution in BMI, age and sex in the participant group (N=29).*

	Mean+SD	**Min**	**Max**	**Female**	**Male**
Age [years]	35 ± 15	18	68	15	14
BMI	24.9 ± 4.1	18.5	36.6		

The group of study participants included patients with both bipolar and major depressive disorder, and they were observed over a period of six months. Before undergoing any study procedures, the patients had to sign an informed consent form after receiving both oral and written information about the study. All data were handled without patient sensitive information such as name and date of birth (de-identification).

All participants underwent an MRI scan at four different time points in the treatment period (see section 3.3 for more details). In ten of the participants the MRI image before and/or after the ECT were missing, and therefore were excluded from the analysis in the current project. In addition, data from another participant were excluded because of poor image quality. Hence, the dataset used consists of material from 29 patients. A summary of the distribution in BMI, age and sex within the participant group is gathered in Table 3.1.

3.2 ECT Treatment

ECT was given in three sessions per week until remission, with a maximum of 18 sessions. The mean, standard deviation (SD), the maximum and the minimum number of treatment sessions n is provided in Table 3.2. In addition, Table 3.2 contains information about the average dose

$$Q_{avg} = \frac{\sum_1^n Q_n}{n},$$

cumulative dose

$$Q_c = \sum_1^n Q_n,$$

and exposure time

$$T_e = \sum_1^n \tau_n \cdot f_n \cdot t_n = \frac{Q_c}{i}. \tag{3.1}$$

In all of the sessions, ECT was done under anesthesia and with muscle relaxant.

Table 3.2: *The mean±SD, maximum and minimum number of ECTs in the participant group (N=29)*

	Symbol	Mean+SD	Min	Max
Number of ECTs	n	10 ± 4	3	18
Average dose [mC]	Q_{avg}	250 ± 110	81	618
Cumulative dose [mC]	Q_c	2541 ± 1631	698	6801
Exposure time [s]	T_e	2.8 ± 1.8	0.8	7.6

For the treatment, a Thymatron System IV (Somatics, Venice, Florida) device was used [55]. The Thymatron ranges from 25.2 to 504 mC in stimulus dose and outputs a bidirectional stimulus of brief square pulses with a constant current i of 900 mA. Furthermore, the pulse width τ was set between 0.25 ms and 1.00 ms for each dose setting, while the stimulus duration t_{dur} and the pulse repetition frequency f were individually calculated by the Thymatron to give the set treatment stimulus dose, Q. The stimulus energy was calculated by Equation 2.47, and was further adapted by Equation 3.2 for female patients and Equation 3.3 for male patients. This was done because clinical experiences indicate that female patients have a lower seizure threshold, and male patients have a higher seizure threshold.

$$\textbf{Female: } E_{stim}[\%] = E[\%] - (5\text{-}10\%) \tag{3.2}$$

$$\textbf{Male: } E_{stim}[\%] = E[\%] + (5\text{-}10\%) \tag{3.3}$$

This sex corrected stimulus energy E_{stim} in percent was set on the Thymatron by rotating the *"PERCENT ENERGY"* dial. This dial selects the treatment stimulus dose. In general, the treatment stimulus dose can be described by Equation 2.48, and is a function of E_{stim} and Q_{max}. The treatment stimulus dose Q for the Thymatron, with its specific Q_{max}, is

$$Q \simeq E_{stim}[\%] \cdot 504\,\text{mC}. \tag{3.4}$$

Hence, a treatment stimulus dose of 504 mC from the Thymatron corresponds to 100 % stimulus energy. In other words, Equation 2.47 together with Equation 3.4 show that the age-based method gives a stimulus dose corresponding to approximately 5.04 mC per year in age if a Thymatron system is used. This is because an increase in one year in age leads to one percent increase in stimulus energy (ignoring sex correction).

Right unilateral electrode placement (RUL) of d'Elia [56] was used for all patients (see Figure 3.1). The first electrode (1) was placed over the frontotemporal region with a flat metal electrode, while the second electrode (2) was a concave metal electrode placed on the line between the two meatus acustici externi, centered three cm to the right of the centerline from nasion to inion. Both the flat and the cupped electrode had a diameter of $\sim 5\,\text{cm}$.

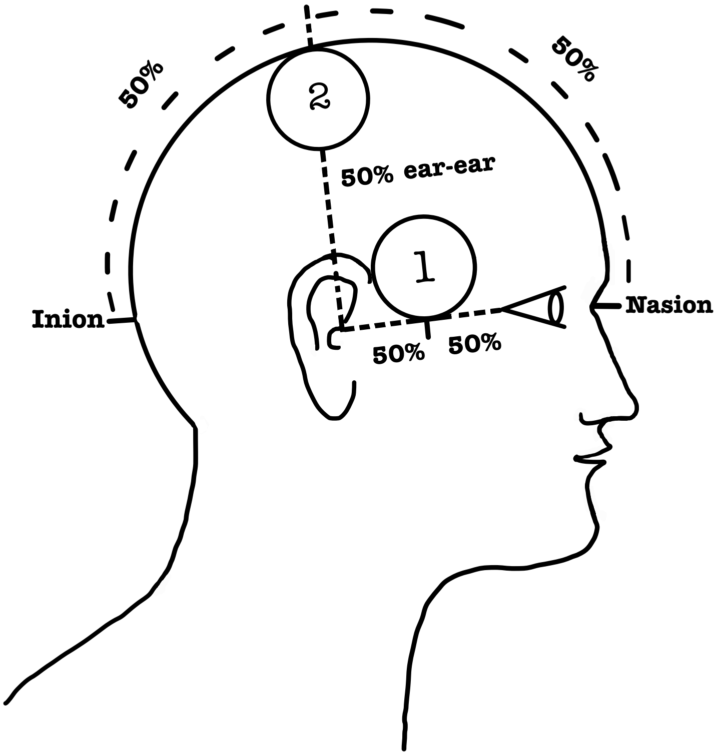

Figure 3.1: *Right unilateral electrode placement (RUL) according to d'Elia [56].*

3.3 MRI Acquisitions

As a part of the ECT-MRI study, image data were acquired using state of the art magnetic resonance imaging (MRI) techniques. A flow chart of the protocol for MRI acquisition is shown in Figure 3.2. It shows that MRI images were acquired at four different time points: The first approximately $1-2$ hours before the initial ECT, the second approximately $1-2$ hours after the initial ECT, the third approximately $7-14$ days after ended treatment and the fourth 6 months after ended treatment. At each time point, the same MRI protocol was used.

Most of the patients in the study were scanned on a 3T Discovery MR750 system with 32 channel head coil, but eight patients included early in the study were scanned using a 3T GE Signa HDxt system with 8 channel head coil. This was due to an upgrade of the hospital MR scanner. In this project, only the T1-weighted image volume at the first and third time point was used. For each patient in this project, the same MR system was used for both MRI 1 and MRI 3.

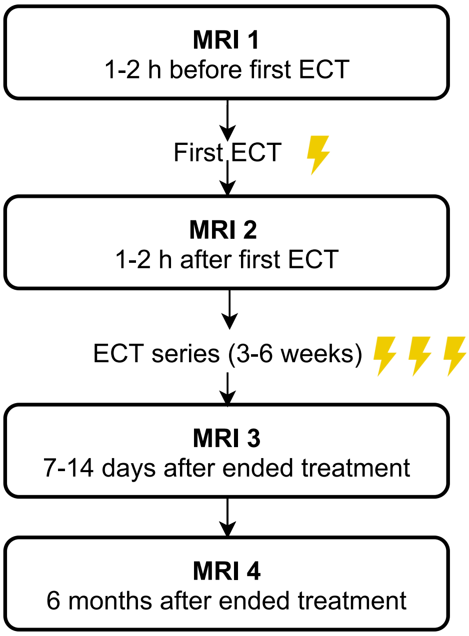

Figure 3.2: *Flow chart of the MRI acquisition protocol for ECT patients*

The T1-weighted image volumes were acquired using a fast spoiled gradient echo (FSPGR) pulse sequence. The MRI data were stored in DICOM format at SAFE (the University of Bergen's secure data storage system used for sensitive data). Furthermore, the specific values that were used in the FSPGR sequence are listed in Table 3.3. As mentioned in section 2.2.2, a short TE and a short TR are chosen to get a T1 weighted image. Additionally, the small α used reduces scan time. The pulse sequence diagram of the FSPGR sequence is provided in Figure 3.3.

The sequence starts with an 180° pulse, applied at the same time as a slice selecting gradient G_{ss}. This pulse inverts the net magnetisation. After it is turned off, the net magnetisation starts to recover along $\overrightarrow{B_0}$. After an inversion time, TI, a new RF pulse with a small flip angle α is applied, that flips the net magnetisation α degrees from the original position along $\overrightarrow{B_0}$. Furthermore, a frequency encoding gradient G_{fe} is used to dephase and rephase the magnetic moments at different locations in the slice to create an echo signal. The phase encoding gradient G_{pe} is used to fill the different lines of k-space in the orthogonal direction. K-space is a data matrix where echo signals are stored. With an inverse 2D Fourier transform, k-space is transformed into an MR-image. Moreover, RF spoiling of the longitudinal magnetisation is achieved by applying RF pulses with different phase offsets, see section 2.2.2. The remaining signal, therefore, depends on the T1 values, the α and the different time parameters.

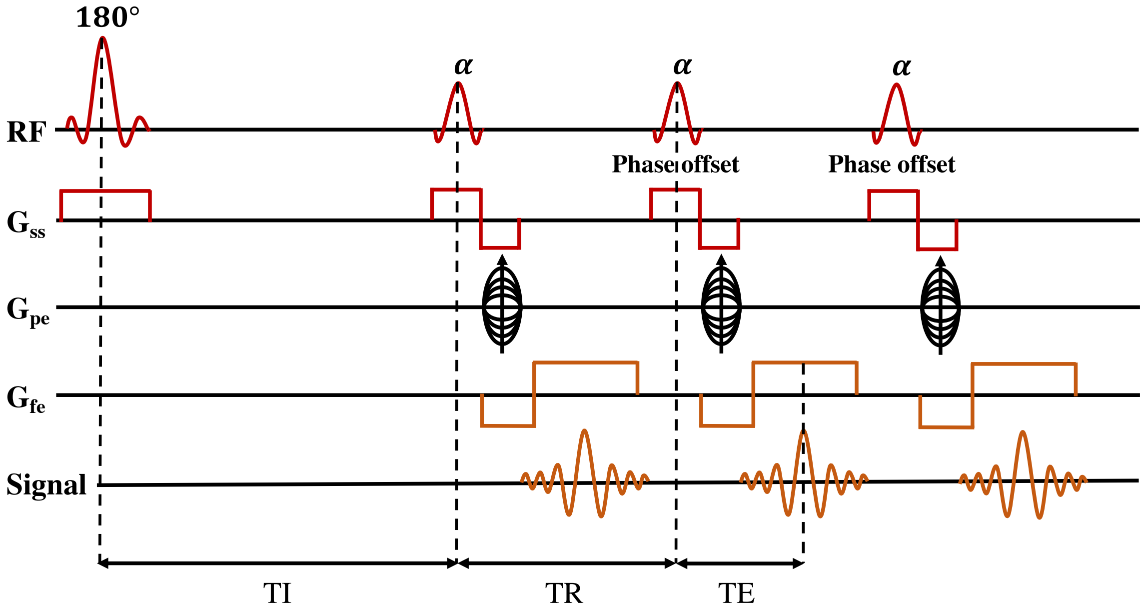

Figure 3.3: *Fast spoiled gradient echo sequence.* G_{ss} *is the slice selecting gradient,* G_{pe} *is the phase encoding gradient and* G_{fe} *is the frequency encoding gradient.*

Table 3.3: *Details for the T1-weighted FSPGR. TE=Echo time, TR=Repetition time, TI=Inversion time,* α*=Flip angle and FOV=Field of view.*

TE/TR	2.9/6.7 ms
TI	600 ms
α	8 °
FOV	25.6 cm
Voxel size	1.0 x 1.0 x 1.0 mm^3
Acquisition time	10:32 min

3.4 Image Analysis

Figure 3.4 shows an overview of the image analysis process. It consists of pre-processing with a FreeSurfer MMPS pipeline, volume segmentation with FreeSurfer [51] and Transcranial Electric Stimulation (TES) with ROAST [19].

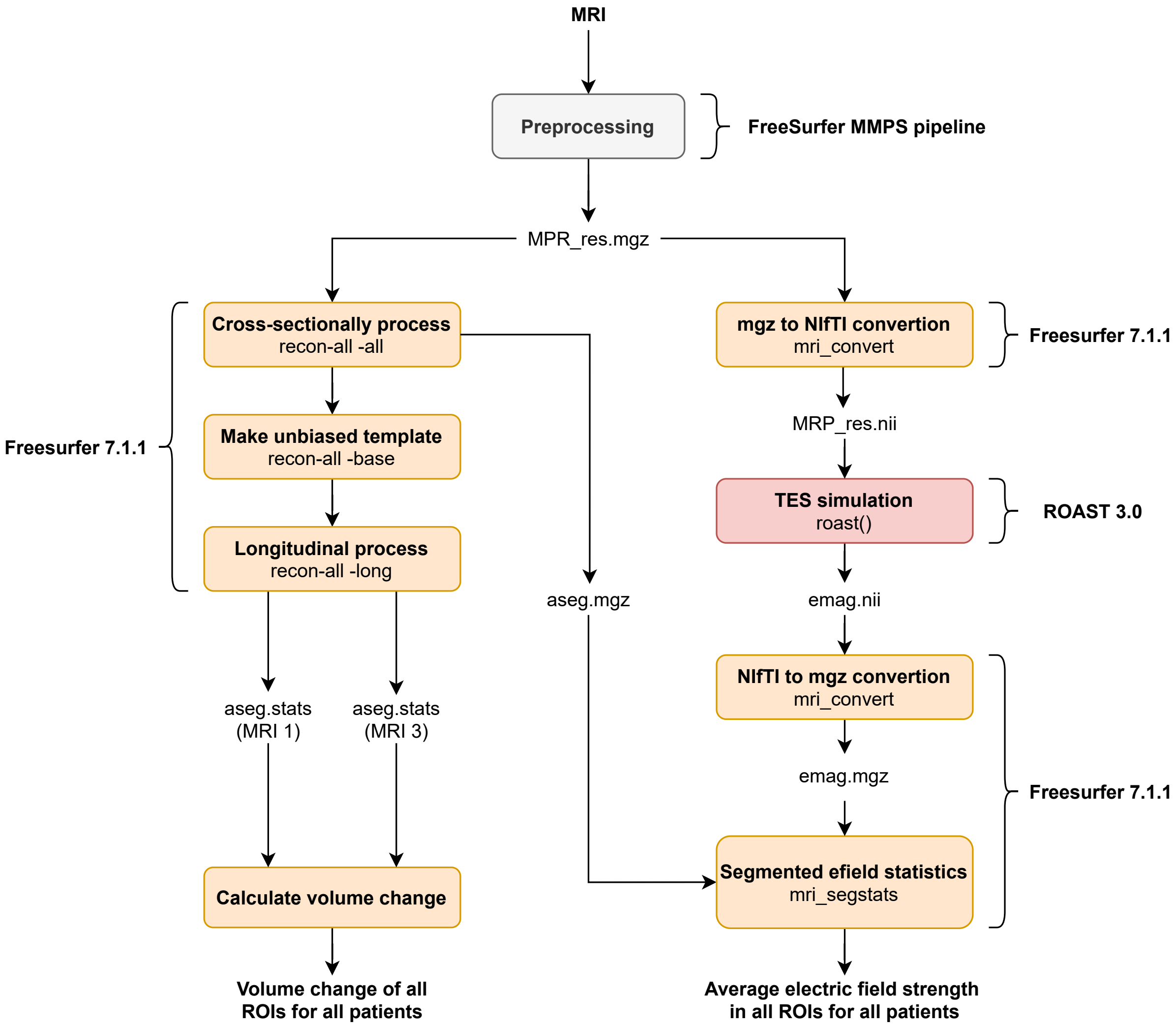

Figure 3.4: Flow chart of the image analysis process

3.4.1 Pre-Processing

Pre-processing is the first step in Figure 3.4, and was done with an already existing script called *runMMPS.sh*. The command in Listing 3.1 was used to start the pre-processing of the MRI data for each patient. E0XX in the command is the folder containing the DICOM files for participant nr. XX.

Listing 3.1: *The command for the MMPS pre-processing*

```
/usr/bin/nohup .runMMSP.sh E0XX > E0XX.log &
```

The script starts to run a docker called *mmps_gemric* with E0XX as input. The pre-processing includes converting DICOM files to mgz-format (FreeSurfer format) and correcting for gradient field nonlinearities with a gradient unwarp tool, where the correction fields are scanner specific. As explained in section 2.2.2, a gradient should ideally produce a magnetic field that increases linearly with distance from the isocenter. Unfortunately, this is not usually the case. The farther one gets from the isocenter, the more gradient linearity falls off [57]. Non-linear gradient fields can affect the accuracy of the geometry and the intensity. How non-linear fields affect image warping depends on the head position and differ between scanner systems from different vendors.

Furthermore, the pre-processing does intensity correction for non-uniformity in B_0. The intensity correction is done with a Non-parametric Non-uniform intensity Normalisation (N3). The N3 intensity normalisation is also a part of the FreeSurfer's *recon-all*-pipeline. In addition, the MRI is registered to a common atlas and resampled to 1 mm isotropic resolution.

The pre-processing is important to reduce possible errors in tissue contrast that can bias the volume segmentation, and hence the estimates of the electric field strength and volumes of the regions of interest (ROI).

3.4.2 Quantification of Volumetric Changes

FreeSurfer version 7.1.1 was used for subcortical volume segmentation of the following ROIs.

- Left/Right Hippocampus
- Left/Right Amygdala
- Left/Right Thalamus
- Left/Right Caudate

The ROIs of the amygdala, the thalamus and the caudate were segmented for reasons of comparison. FreeSurfer (FS) is a powerful analytical tool. It does surface-based analysis and creates computerised models of the brain from MRI data. For this project, the FS Longitudinal Processing pipeline was used [58]. This pipeline consists of the following steps.

- Cross-sectional analysis
- Base creation
- Longitudinal analysis

Cross-sectional analysis: recon-all

The cross-sectional processing uses the regular FS processing stream called *recon-all*, and it is the first of three steps in the longitudinal processing pipeline. It does all of the FS cortical reconstruction processes, consisting of 31 processing steps. If any of these fail, it is possible to return and run a subset of these steps to save time [59]. With a docker version of FS 7.1.1 (see subsection 3.5.1) it took about 6 hours to run all of the steps of *recon-all* for one MR image.

To run *recon-all*, a subject ID and an input T1 weighted image need to be specified. The unwarped, N3 intensity normalised and resampled image, *MPR_res.mgz*, from the pre-processing was used as input. The subject ID was set to E0XX_01 for the analysis of MRI 1 and E0XX_03 for analysis of MRI 3. This created two directories for each subject with the names E0XX_01 and E0XX_03, containing a cross-sectional analysis of the images. Listing 3.2 shows the two commands that were run to segment and reconstruct cortical surfaces of the two 3D volumes (MRIs) for all 29 subjects.

Listing 3.2: *The commands for cross-sectional analysis/processing with recon-all*

```
recon-all -i MPR_res.mgz -subjid E0XX_01 -all
recon-all -i MPR_res.mgz -subjid E0XX_03 -all
```

A summary of the *recon-all* processing pipeline is illustrated in Figure 3.5. The first three steps are the most important for this thesis. What these steps include will now be further explained. First of all, it is important to have a T1 weighted image with good contrast between grey and white matter since the segmentation is intensity-based [59].

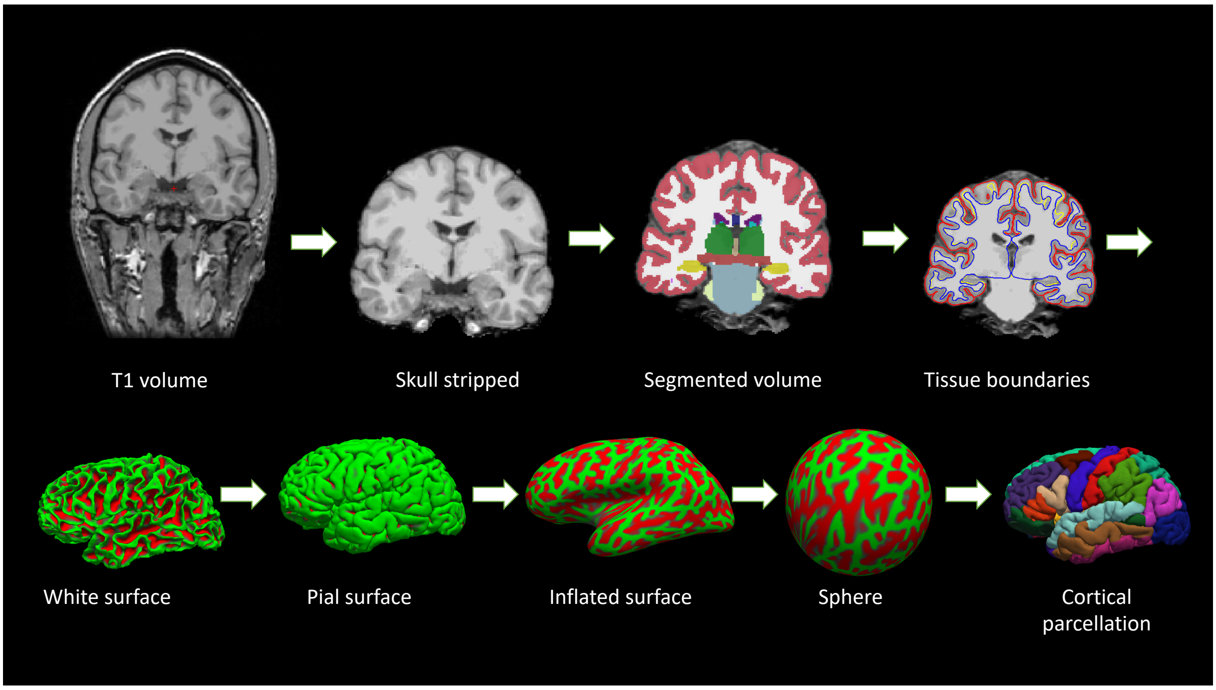

Figure 3.5: *The recon-all processing pipeline. A test object called "Bert", found in the subjects folder in FS was used to make this illustration.*

The input volume (*MPR_res.mgz*) can be found as mri/*orig.mgz* in the subject folder since it is the only input image, and it already is in mgz format after the pre-processing. Hence, *orig.mgz* was used as input to ROAST as it was more easily accessible than *MPR_res.mgz* (see subsection 3.4.3). In the *recon-all* processing pipeline, the orig volume (*orig.mgz*) is once again corrected for non-uniformity in intensity with N3 (earlier done in pre-processing, see subsection 3.4.1). Often, an MRI has brighter and darker areas (worse with many coils), where the brightness depends on the distance from the receiver coils. White and grey matter can be made more homogeneous with normalisation. In the N3 process, four iterations of the tool *nu_correct* are run, and the file mri/*nu.mgz* is created. This correction is essential since the segmentation is intensity-based, and it is needed to separate grey and white matter. Furthermore, an intensity normalisation where the intensities are scaled so that the mean intensity of the white matter is 110 is performed on all the voxels [59]. The output of this normalisation is mri/*T1.mgz* and can be seen as the first image in Figure 3.5

Moreover, *recon-all* removes the skull from the brain volume and creates the file mri/*brainmask.mgz*. This is the second step in Figure 3.5. Everything that is not the cortex or subcortical grey or white matter is removed. This volume mask is later applied to the result images from ROAST to illustrate the electric field in the brain.

After the skull-stripping, the normalised brain volume is segmented into subcortical structures, cortex and white matter. The volume segmentation of subcortical structures in the brain is based on intensities and an atlas found in the ’average’ directory containing probabilistic information on the location of the structures [60]. The segmented structures are saved in mri/*aseg.mgz*. This is the third image in Figure 3.5. Each voxel in *aseg.mgz* is assigned one of 37 labels and gets the colour that belongs to this label. For example, the left and right hippocampus can be seen as yellow in the third image in Figure 3.5. stats/*aseg.stats* contain the computed volumes of the segmented subcortical ROIs. The *aseg.mgz*-file from this cross-sectional process is later used as a mask to segment out the average electric field strength in the ROIs (see Figure 3.4 and subsection 3.4.3).

Base creation: recon-all -base

Base creation is the second step of the longitudinal processing pipeline. Based on the assumption that head size does not change with time [61], it creates a within-subject template space and image (base) [62]. One single base named E0XX is created for each subject based on the information at time point (tp) 1 and tp 3. E0XX now represents a new unbiased template for this subject, and will be passed onto the last longitudinal processing step for both time points [61]. By using a within-subject template, meaning using a subject as his or her own control, reliability and statistical power significantly increase [58]. Listing 3.3 shows the command used to create the within-subject template for each subject. Creating a base for one subject took approximately 6 hours with the FS docker.

Listing 3.3: *The command for base creation. A base is made from time point 1 and 3 for all subjects.*

```
recon-all -base E0XX -tp E0XX_01 -tp E0XX_03 -all
```

Longitudinal analysis: recon-all -long

This is the third and last step in the longitudinal processing pipeline. Two longitudinal runs were done for each subject, one for each time point (see Listing 3.4). The longitudinal analysis for one time point takes around two hours.

Listing 3.4: *The commands for the longitudinal analysis for time point 1 and 3*

```
recon-all -long E0XX_01 E0XX -all
recon-all -long E0XX_03 E0XX -all
```

After running this analysis, the two directories, E0XX_01.long.E0XX and E0XX_03.long.E0XX, were created. They contain the most reliable and accurate processing results when comparing these files with the files from the cross-sectional analysis. The computed volumes of the segmented ROIs (at both time points) found in stats/*aseg.stats* for all subjects were gathered and saved to one file (see Listing 3.5).

Listing 3.5: *The command used in the FS docker to gather all the ROI volumes from aseg.stats (both time points) from all 29 subjects and save it to one text file. 10=Left-Thalamus, 11=Left-Caudate, 17=Left-Hippocampus, 18=Left-Amygdala, 49=Right-Thalamus, 50=Right-Caudate, 53=Right-Hippocampus and 54=Right-Amygdala.*

```
asegstats2table \
--inputs    FS/E001_01.long.E001/stats/aseg.stats \
            FS/E001_03.long.E001/stats/aseg.stats \
            FS/E002_01.long.E002/stats/aseg.stats \
            FS/E002_03.long.E002/stats/aseg.stats \
            .
            .
            .
            FS/E029_01.long.E029/stats/aseg.stats \
            FS/E029_03.long.E029/stats/aseg.stats \
--segno     10 11 17 18 49 50 53 54 \
--meas      volume \
--tablefile FS/AllSubjs_ROIs_asegsegstats_volume.txt
```

3.4.3 Simulation of Electric Fields

ROAST was used to simulate the electric field in the brain generated during ECT treatment. It is an open-source tool that runs on MATLAB, that combines a segmentation algorithm of SPM 12, a MATLAB script for touch-up and electrode placement, a finite element (FE) mesher called iso2mesh and the FE solver getDP [19]. For this project, ROAST version 3.0 (Hell's Kitchen) was used with MATLAB (R2020b, Mathworks inc., Massachusetts, USA). A docker version of ROAST was developed for this project and is described in subsection 3.5.2.

Converting from FreeSurfer Format to NIfTI

ROAST needs a T1 (or T2) weighted image as input in NIfTI format [19]. The *orig.mgz* image found in the output directory from the cross-sectional processing of tp 1 in FS was therefore converted to *orig.nii* before running the simulation (*orig.mgz* for tp 3 was used for three subjects because of poor resolution at tp 1). This was done by running the *mri_convert*-function in the FS docker. The command used can be seen in Listing 3.6.

Listing 3.6: *The command used to convert orig.mgz to orig.nii*

```
mri_convert FS/E0XX_01/mri/orig.mgz ROAST/E0XX/orig.nii
```

The ROAST Pipeline

Figure 3.6 shows the pipeline for transcranial electric stimulation modelling in ROAST and Table 3.4 shows the settings used for each subject. First of all, the *orig.nii* is re-oriented into RAS orientation (towards Right, towards Anterior, towards Superior). The zero-padding option was used to avoid complications with large electrodes placed close to the image boundaries [63]. It adds 60 empty slices to the RAS oriented MRI in all six directions. This zero-padded MRI is further used as input to ROAST.

Table 3.4: *Details for the TES simulation done with ROAST.*

Input image	*orig.mgz*
Current	±900 mA
EEG capsystem	10-05
Electrode placement	C2 and FFT8
Electrode type	Disc
Electrode size	Radius=25 mm; Height=1 mm
Zero-padding	60 slices

Starting from an MRI image volume, a full head is segmented into air cavities and five different tissue compartments; white matter, grey mater, CSF, bone and scalp. It then assigns conductivity to all of the different compartments [19]. These conductivities are listed in Table 2.1 in subsection 2.1.4. For segmentation, ROAST uses Statistical Parametric Mapping 12 (SPM12, Wellcome Centre for Human Neuroimaging, London, UK). The segmentation algorithm of SPM12 is applied for the whole head and neck with an extended tissue probability map for the head [19][23]. The tissue probability map also marks important skull openings, like the optic foramen, by making a special mask marking these regions. Post-processing of the segmentation includes smoothing segmentation masks, filling holes of CSF and remove disconnected voxels. [19].

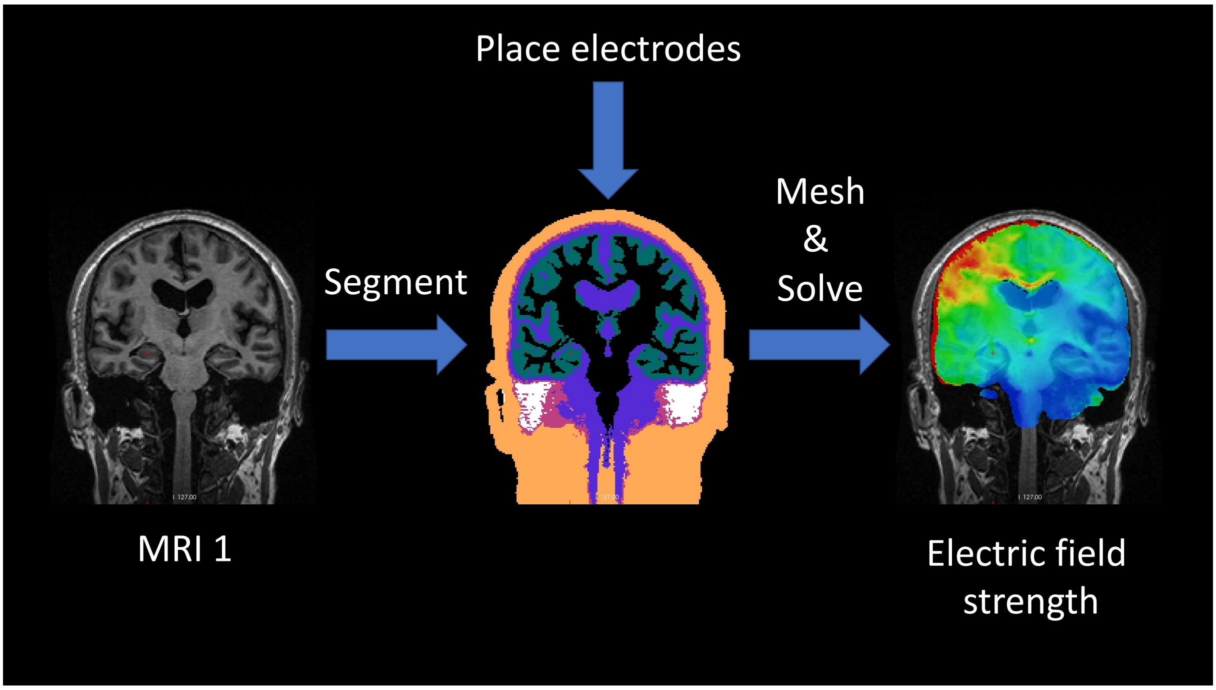

Figure 3.6: *TES modelling pipeline for ROAST.*

The virtual electrode placement is done by a MATLAB script. For this project, locations from the 10-05 EEG system was used (see Figure 3.7). This is a method to describe standardised locations of the electrodes on a head model [64]. Following the same method as Argyelan et al. [6], location C2 and FT8 were first used. This was changed to C2 and FFT8 because of problems with placing the second electrode for a lot of the subjects (see Figure 3.7). The placing is supposed to correspond to RUL electrode placing (see Figure 3.1)

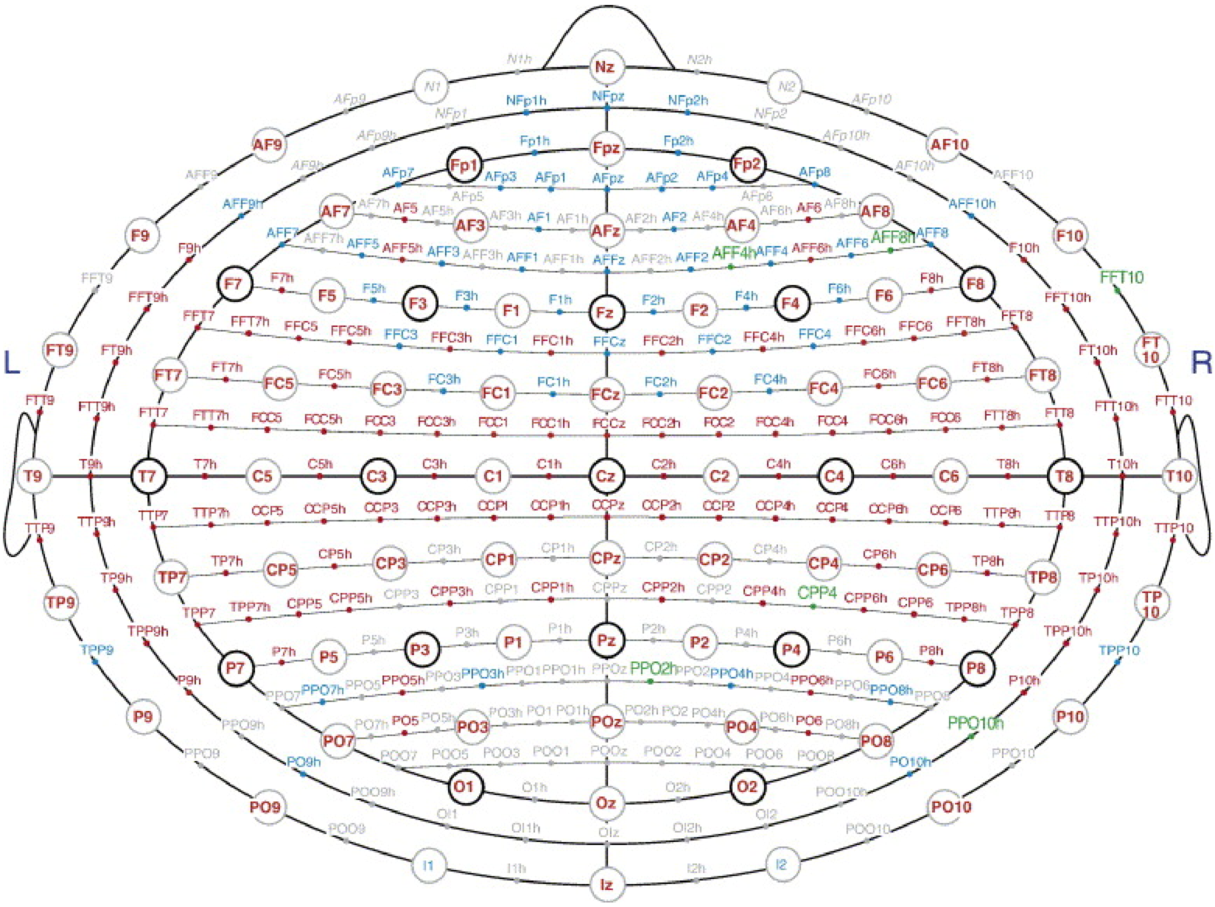

Figure 3.7: *The five percent electrode EEG system (10-05 EEG system). The electrodes are placed on curves with approximately equal distance (5 %) between each other. Figure taken from Jurcak et al. [64].*

From the segmented MRI a tetrahedral Finite Element Model (FEM) mesh is generated using the MATLAB toolbox iso2mesh. Iso2mesh is a 3D surface and volumetric mesh generator. It extracts the post-processed segmentation masks of the GM, WM, CSF, skull, scalp and air as closed triangular iso-surfaces and fills tetrahedral elements in the sub-volumes bounded by these. It uses the *cgalv2m*-function (Computational Geometry Algorithms Library: Volume to mesh) to do this.

The FE mesh is solved for voltage and then the electric field using GetDP (A General Environment for the Treatment of Discrete Problems) version 3.2.0. It solves the underlying Laplacian equation, Equation 2.28, for each vertex/node based on the tissue conductivity and current density at each electrode (one anode and one cathode) [19]. At the anode, a normal inward current density is defined to be

$$-\mathbf{n}\cdot\mathbf{J}_{\mathbf{anode}} = J_s$$

where J_s is the stimulation current density $J_s = I/A$, I is the input stimulus current, A is the area (m^2) of the electrode ($A = \pi r^2$) and $\mathbf{n}$ is a vector normal to the head surface. The cathode is set to be ground with $V = 0$. Everywhere else on the head boundary, the normal current flow is set to be zero, making an insulating boundary. Inner tissue boundaries are defined in a way to ensure continuity in current flow [65]. If $\mathbf{J_1}$ and $\mathbf{J_2}$ are the current densities in two neighbouring tissues, the inner boundary condition would be

$$\mathbf{n} \cdot (\mathbf{J_1} - \mathbf{J_2}) = 0.$$

The source current is specified in the command line that starts the program. Listing 3.7 shows the command that was run in the ROAST-docker for each subject to get simulated electric fields. It took about 12 minutes to simulate the electric field in one brain.

Listing 3.7: *The command used to run roast() for each subject*

```
roast('ROAST/E0XX/orig.nii',{'C2',900,'FFT8',-900},
'capType', '1005', 'elecSize', [25 1], 'zeroPadding', 60)
```

Converting from ROAST to FreeSurfer Format

Electric field magnitude data from ROAST can be found as *orig_'simulationTag'_emag.nii*. This file will be referred to as *emag.nii*. Because orientation was changed and 60 extra slices were added to *orig.nii* in the ROAST process, the dimension and orientation of *emag.nii* is entirely different from *orig.nii*. Hence, dimension and orientation need to be considered when *emag.nii* is going to be converted to FS format (mgz). A conversion to FS format is necessary since *aseg.mgz* will be used to segment out the electric field in the ROIs. The whole converting process can be seen in Figure 3.8

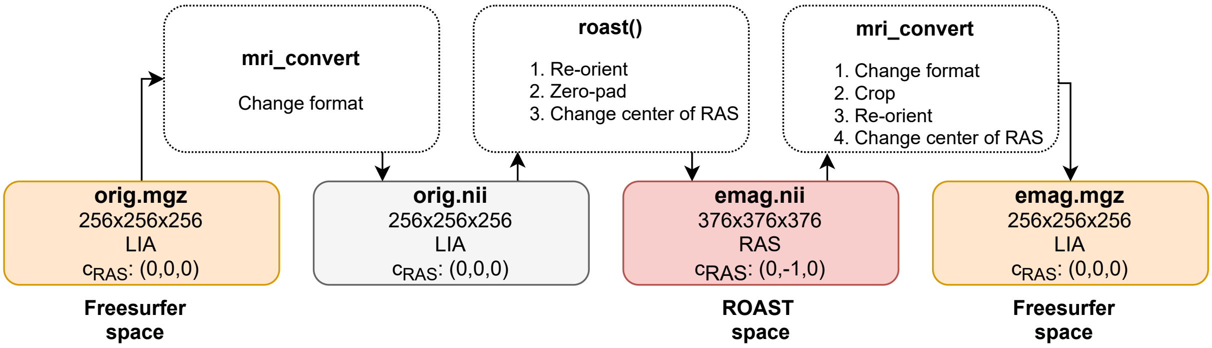

Figure 3.8: *The converting process.*

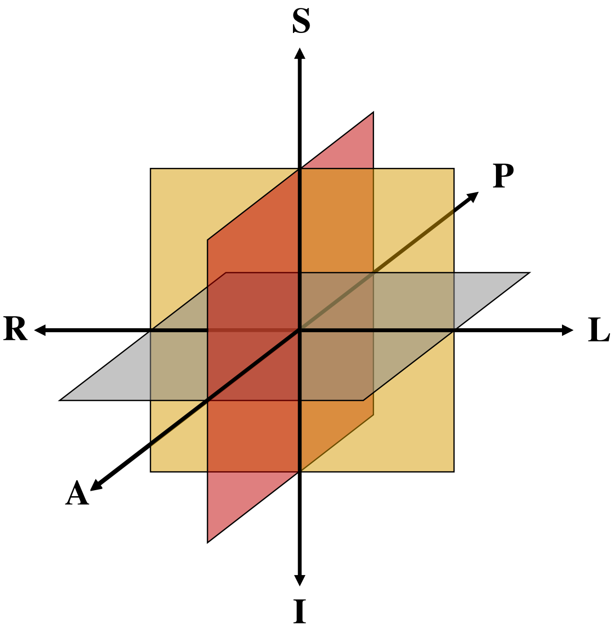

Figure 3.9: *Orientations. R=Right, L=Left, S=Superior, I= Inferior, A=Anterior and P=Posterior.*

Figure 3.9 shows the different orientations of MRI coordinate systems. The function *mri_info* in FS was used to find the dimension, orientation and center of RAS c_{RAS} (origin if orientation was RAS) for *aseg.mgz* and *emag.mgz*. This info is gathered in Table 3.5.

Table 3.5: *Information about dimension, orientation and center of RAS*

	aseg.mgz	***emag.mgz***
Dimension	$256 \times 256 \times 256$	$376 \times 376 \times 376$
Orientation	LIA	RAS
Center of RAS	$(0,0,0)$	$(0,-1,0)$

Listing 3.8 shows the command that was used to convert *emag.mgz* to *emag.nii*, re-orient it from RAS to LIA, crop the image to $256 \times 256 \times 256$ around a center c_{crop} and move the center of RAS. To move the center of RAS to $(0,0,0)$, the crop center of *emag.nii*, was calculated according to

$$c_{crop} = \left(\frac{376}{2}, \frac{376}{2}, \frac{376}{2}\right) - c_{RAS} = (188,188,188) - (0,-1,0) = (188,189,188).$$

Listing 3.8: *The command used in the FS docker to convert emag.nii to emag.mgz. The image is cropped to the dimension* $256 \times 256 \times 256$ *around the center (188,189,188), and orientation is changed from RAS to LIA.*

```
mri_convert \
--crop                 188 189 188 \
--in_orientation       RAS \
--out_orientation      LIA \
--in_type              nii \
--out_type             mgz \
ROAST/E0XX/*_emag.nii  efield/E0XX/emag.mgz
```

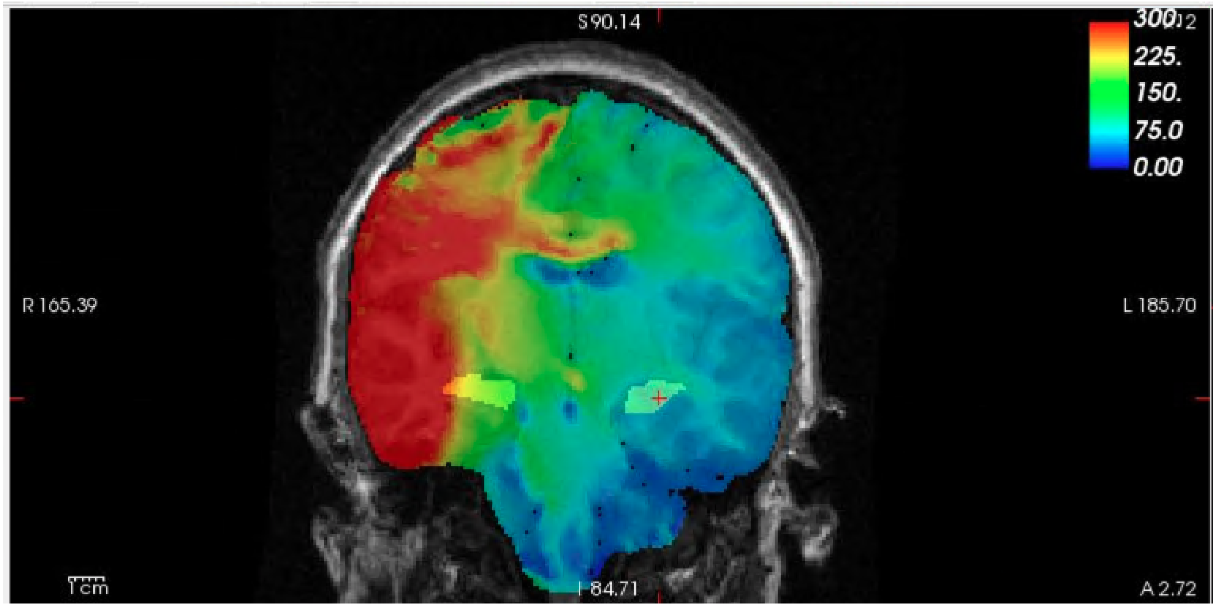

Figure 3.10: *The simulated EF strength in a brain visualised with freeview. mri_mask was used to mask emag.mgz with brainmask.mgz to get this image. The segmentation of the hippocampi is behind the EF.*

Segmenting the Electric Fields

The emag files from ROAST are voxel-wise electric field distribution maps for each subject (see Figure 3.10). An FS function called *mri_segstats* was used to compute the average electric field (EF) strength spatially across each ROI, based on the cross-sectional segmentation of MRI 1 (*aseg.mgz* from section 3.4.2). Listing 3.9 shows the command with all of the options that were used for each subject. The highest and lowest one percentile was excluded in the average calculations of EF strength. The output, *segstats_emag.txt*, contains info about *all* the segmentation volumes from *aseg.mgz*

Listing 3.9: *The command used in the FS docker to segment the average electric field strength inside the ROIs. Highest and lowest 1 percentile EF strength was excluded in the calculations with "–robust 1".*

```
mri_segstats \
--sd         FS\
--seg        FS/E0XX_01/mri/aseg.mgz \
--i          efield/E0XX/emag.mgz \
--ctab       $FREESURFER_HOME/FreeSurferColorLUT.txt\
--excludeid 0 \
--robust     1 \
--sum        efield/E0XX/segstats_emag.txt
```

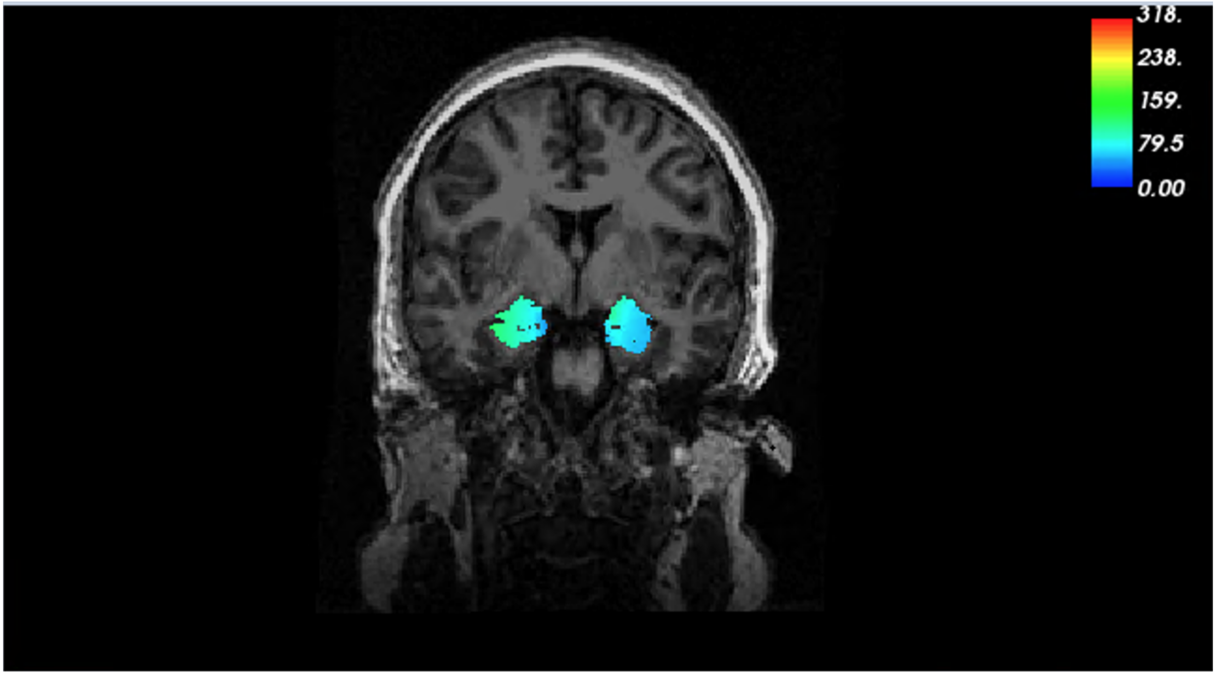

Figure 3.11: *The simulated electric field strength in hippocampus visualised with freeview. mri_mask was used to mask emag.mgz with results from the hippocampus module to get this image.*

The electric field strength in the left and right hippocampus for a random participant can be seen in Figure 3.11. To extract and gather the average electric field strength within the ROIs from all subjects into one table, the FreeSurfer function *asegstats2table* was used. The command used can be seen in Listing 3.10.

Listing 3.10: *The command used in the FS docker to create one text table with the segmented average EF strength (mean) in the ROIs from all subjects. 10=Left-Thalamus, 11=Left-Caudate, 17=Left-Hippocampus, 18=Left-Amygdala, 49=Right-Thalamus, 50=Right-Caudate, 53=Right-Hippocampus and 54=Right-Amygdala.*

```
asegstats2table \
--inputs    efield/E001/segstats_emag.txt \
            efield/E002/segstats_emag.txt \
            .
            .
            .
            efield/E029/segstats_emag.txt \
--segno     10 11 17 18 49 50 53 54 \
--meas      mean \
--tablefile efield/AllSubs_ROIs_segstats_emag.txt
```

3.5 Docker Containers

Docker is a way to package an application and all its dependencies into a file so that it works in the same way when it is moved from one computing environment to another. One tries to limit the data stored inside it so that it runs quickly and is easy to move. A Docker container image is an executable package of software that has everything it needs to run an application. When the image is run, a Docker container is created [66]. A container uses an isolated filesystem to run the application, where all the data created inside the container does not persist after the container stops existing. Directories on the host machine can therefore be mounted into the container to share files and to store files created by the container. The directory can be mounted to an already existing directory, or it will create a new one on demand [67].

To create an image, a Dockerfile written in Go programming language needs to be generated. It consists of all the steps needed to build an image, where each instruction creates a layer in the image. Often, an image is based on another Docker image [66]. Two Docker container images were developed as a part of this thesis, one for FreeSurfer 7.1.1 and one for ROAST 3.0.

3.5.1 FreeSurfer 7.1.1

This image was build based on the official dockerised FreeSurfer neuroimaging package *freesurfer/freesurfer:7.1.1* [68]. As seen in Listing 3.11, my own licence for FreeSurfer was copied into the docker image.

Listing 3.11: *Dockerfile for FreeSurfer 7.1.1*

```
FROM freesurfer/freesurfer:7.1.1
COPY license.txt /usr/local/freesurfer/.license
```

The image was build and got the tag (-t) *freesurfer_docker:7.1.1* by running the *docker build* function in the terminal (see Listing 3.12).

Listing 3.12: *Building Docker image*

```
docker build -t freesurfer_docker:7.1.1 .
```

Each time this image was used to create a container for an FS analysis, a similar command like the one in Listing 3.13 was used. It creates a new Docker container from the image *freesurfer_docker:7.1.1* that runs in interactive (-i) mode and is attached to the terminal (-t). It means that one can give input to the container with the keyboard and that output is logged in the terminal [66]. The container has two mounted volumes to it that enables it to create or modify files in these directories. Inside the container, an FS command (-c) is executed in a Bourne-again shell (bash). Furthermore, -rm means that the container is automatically removed when it exits [69].

Listing 3.13: *Running the FreeSurfer Docker container*

```
docker run --rm -it \
-v </path/to/input/data>:/input \
-v </path/to/output/data>:/usr/local/freesurfer/subjects \
freesurfer_docker:7.1.1 \
/bin/bash -c "<FS command>"
```

3.5.2 ROAST 3.0

This docker image was provided to me by Njål Brekke. As a summary, an image with a Linux environment and an installation of MATLAB R2020b was created following the instructions at Github [70]. This MATLAB image was further used as the base for the ROAST image. The building of the ROAST image includes downloading and unzipping the roast-3.0-zipfile. A MATLAB licence was copied into the Docker image that is connected to a MAC (Media Access Control) address. Hence the MAC address needs to be passed on to the container each time it is run to set the container's Ethernet to the MAC address.

The standard command that was used to run a ROAST analysis in the Docker container for this thesis can be seen in Listing 3.14. The image *imossige/roast:3.0* creates a container that runs in an interactive mode and is removed after it exits. MATLAB is opened from the terminal with the option -nosoftwareopengl because of troubles with the software OpenGL on the Linux operating system Ubuntu. Furthermore, it executes the commands written after the -r option. In Listing 3.14, it can be seen that the working directory is changed to the directory that is mounted to the folder ROAST/E0XX, which contains the input image *orig.mgz*. Further, the roast command is executed, and all output in the terminal is saved to a log file called *E0XX.txt*.

Listing 3.14: *Running the ROAST Docker container*

```
docker run --rm -it \
--mac-address xx:xx:xx:xx:xx:xx \
-v ROAST/E0XX:/opt/roast-3.0/subjects \
imossige/roast:3.0 \
-nosoftwareopengl \
-r "cd /opt/roast-3.0/subjects; \
<ROAST command>; \
exit;" \
> ROAST/roastLogs/E0XX.txt
```

3.6 Statistical Analysis

All statistical analysis, linear models, scatterplots and boxplots presented in this thesis were made in RStudio (version 1.3.959) [52]. The percentage volume change ΔV in each ROI for each subject where estimated by subtracting a odd number line (tp 1) from the following even number line (tp 3), and dividing the difference by the odd number line (tp 1) in a data frame based on the file *AllSubjs_ROIs_asegsegstats_volume.txt* created by Listing 3.5 (contains the unbiased longitudinal volume segmentations). Furthermore, the average EF strength data was extracted from the file *AllSubs_ROIs_segstats_emag.txt*, which was the output from the command in Listing 3.10. The average EF strength will in the next chapters sometimes be referred to as just the EF strength.

Data about each treatment stimulus dose Q_i, age, sex and BMI were collected from already existing SPSS and Excel files associated with the local study and were stored in a separate Excel file. The average dose Q_{avg} and cumulative dose Q_c was calculated in Excel. RStudio was used to calculate the exposure time T_e, by dividing Q_c with 900 mA (see Equation 3.1).

Simple (one variable) and multiple linear regression models were created in RStudio with the *lm()* function. These are statistical models that analyse the relationship between a response variable ($\mathbf{y}$) and one or several explanatory variables ($\mathbf{x_1}, \mathbf{x_2} ... \mathbf{x_p}$) and their interactions. Linear regression models are created based on the following assumptions:

- The y-values can be expressed as a linear function of the predicting independent variables
- The residuals are independent of each other
- The residuals have constant variance
- The residuals are normally distributed
- There is no multicollinearity (happens when the independent variables are too highly correlated)

The *lm()*-function uses the least square method to find coefficients that make the data fit the linear model in Equation 3.5 [71].

$$\mathbf{y} = \beta_0 + \beta_1 \cdot \mathbf{x_1} + \beta_2 \cdot \mathbf{x_2} + ... + \beta_p \cdot \mathbf{x_p} \tag{3.5}$$

Hence, the resulting linear regression model will be on the form

$$\hat{\mathbf{y}} = b_0 + b_1 \cdot \mathbf{x_1} + b_2 \cdot \mathbf{x_2} + ... + b_p \cdot \mathbf{x_p}, \tag{3.6}$$

where $\hat{\mathbf{y}}$ is the vector with predicted y-values and $\mathbf{y} - \hat{\mathbf{y}}$ is the residual vector $\mathbf{e}$ of the linear regression model, Equation 3.6, of p predicting variables. Estimated regression coefficients $(b_0, b_1, b_2...b_p)$, estimated standard errors (SE) of the coefficients, t-values, p-values of the coefficients, adjusted multiple R^2, the F-value and the p-value for the whole model were found using the *summary()*-function on the linear models.

The t-value associated with a coefficient is the estimated coefficient b divided by its standard error SE (see Equation 3.7) [72].

$$t = \frac{b}{SE} \tag{3.7}$$

where the estimated standard error of the coefficient is

$$SE = \sqrt{\frac{\sum_{i=1}^{n}(y_i - \bar{y})^2 - b^2 \sum_{i=1}^{n}(x_i - \bar{x})^2}{(n-2)\sum_{i=1}^{n}(x_i - \bar{x})^2}}. \tag{3.8}$$

In Equation 3.8, $n-2$ is the degrees of freedom (df) [72]. Furthermore, the p-value of the coefficient is the probability of achieving an absolute t-value that high or higher by coincidence if the null hypothesis ($\beta_i = 0$) was true [72]. A 95 % confidence interval was used, meaning the alpha level is 0.05. This is a typical level for educational research. A calculated p-value below the alpha level means there is a statistically significant relationship. A statistically significant relationship means one can reject the null hypothesis that the real coefficients are zero ($\beta_i = 0$).

Moreover, the multiple R^2 tells how much of the variance in y the model explains. R^2 is generally described as

$$R^2 = 1 - \frac{SS_{res}}{SS_{tot}}, \tag{3.9}$$

where the total sum of squares is

$$SS_{tot} = \sum_{i=1}^{n}(y_i - \bar{y})^2, \tag{3.10}$$

the sum of squares of the residuals is

$$SS_{res} = \sum_{i=1}^{n} {e_i}^2, \tag{3.11}$$

and n is the sample size. The adjusted R^2 is adjusted for the number of explanatory variables in the model [73] since R^2 automatically increases with increasing predictors even though the predicting variables may not have statistical power.

The linear relationship between two variables (x and y) is determined by Pearson's correlation coefficient r, calculated by the function $cor()$ in RStudio. If $\bar{x}$ and $\bar{y}$ are the mean of x and y, respectively, the correlation coefficient can be expressed as

$$r = \frac{\sum_{i=1}^{n}(x_i - \bar{x})(y_i - \bar{y})}{\sqrt{\sum_{i=1}^{n}(x_i - \bar{x})^2}\sqrt{\sum_{i=1}^{n}(y_i - \bar{y})^2}}. \tag{3.12}$$

Equation 3.12 shows that r is the covariation of x and y divided by their individual standard deviations multiplied [72]. r takes on a value between -1 and 1. A negative correlation means the two variables vary in the opposite direction, meaning one of them increase if the other decrease. If the correlation is positive, it means the variables vary in the same direction [72]. The correlation will be of greatest strength if the two expressions $(x_i - \bar{x})$ and $(y_i - \bar{y})$ either have the same or opposite sign for all values of i. Furthermore, a correlation value close to zero indicates that the two variables are independent of each other. A correlation test was done with the function *cor.test()* to find the p-value that tells if the correlation is significantly different from zero. An alpha level of 0.05 was used. Consequently, with a p-value below this value, the null hypothesis that there is no linear relationship between the two variables can be rejected.

Chapter 4

Results

In this chapter, plots and statistical values, produced in RStudio, representing the relationship between EF strength, volume change, and variables assumed to have an effect on these will be presented. These variables are BMI, age, sex, intracranial volume and number of ECT sessions. Additionally, plots and statistics will be presented for volume change versus different dose concepts. Coloured scatter plots represent the individual relationship between two variables. A straight line in the same colour as the scatter plot represent the fitted linear regression model for the variables. All fitted linear models have a 95 % confidence interval added with a more transparent version of the colour.

4.1 Electric Field Strength

This section explores the relationship between EF strength and the variables BMI, age, sex, and intracranial volume. The simulation of the TES in ROAST outputs a static image of the EF (see Figure 4.1 and 4.2). ROAST only takes in one of the dose parameters, current, that is 900 mA for all patients. Hence, plotting EF versus dose has no meaning and was not done.

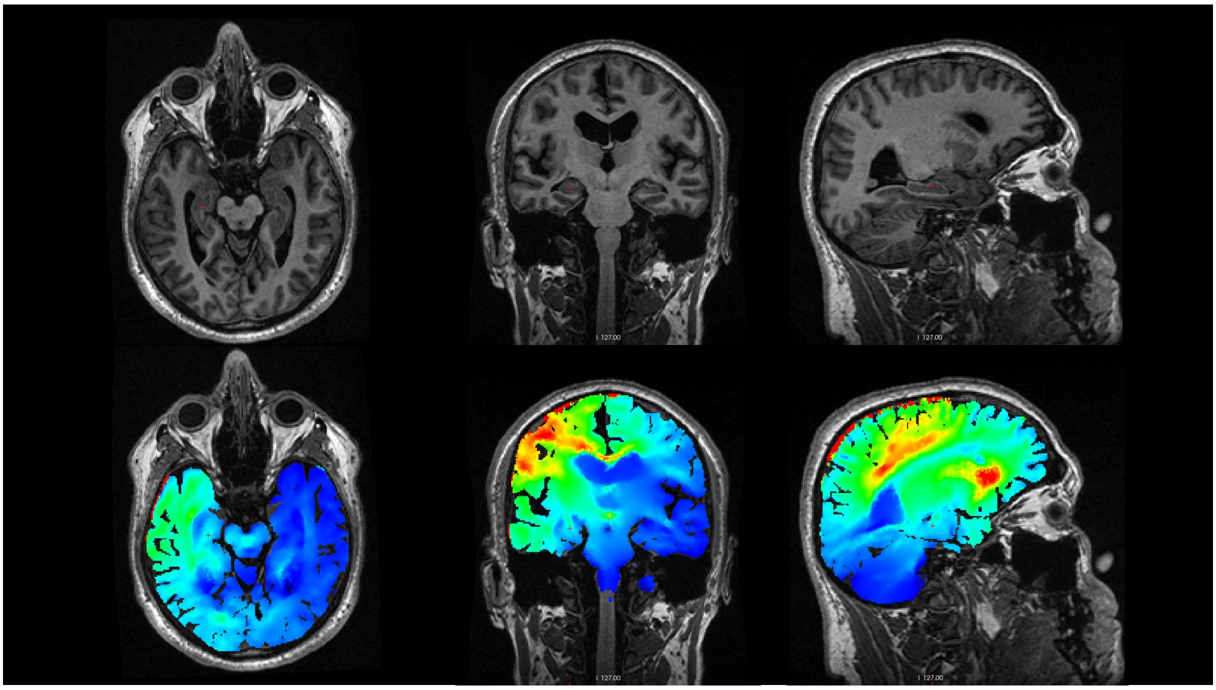

__Figure 4.1:__ Random participant, MRI 1. __Top:__ Axial, coronal and sagittal view of a T1-weighted MRI (orig.mgz). __Bottom:__ Axial, coronal and sagittal view of the EF strength in a brain (emag.mgz masked with aseg.mgz). The minor red cursor points at the right hippocampus.

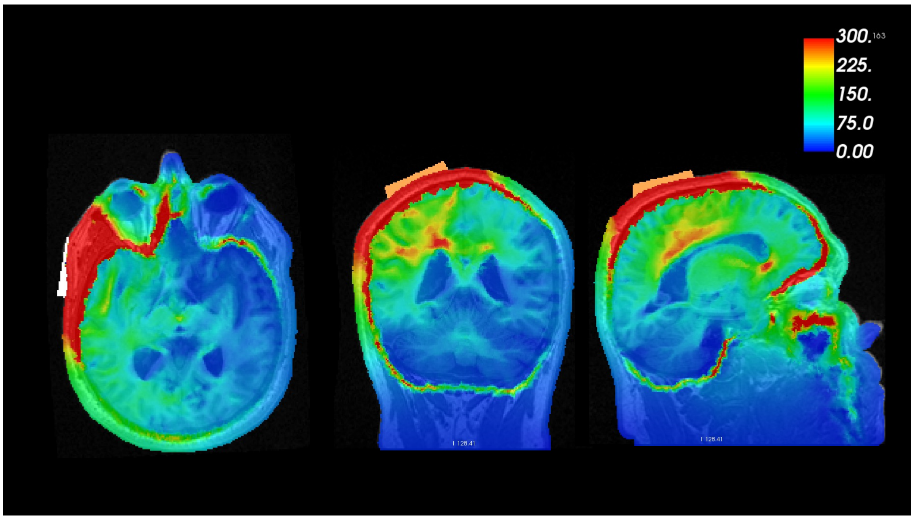

__Figure 4.2:__ Random participant, MRI 1. Axial, coronal and sagittal view of the simulated EF in the whole head. The two electrodes can be seen in white and light orange. The colourmap was scaled to see contrast in the brain. Consequently, EF strength values higher than 300 V/m are coloured as 300 V/m.

4.1.1 Effect of BMI

Hippocampus

A plot of the average electric field strength in the left and right hippocampus versus BMI is shown in Figure 4.3. Both the EF strength in the right and left hippocampus are negatively correlated with BMI. Hence, the linear models indicate that a patient with a lower BMI will receive a greater EF strength in the left and right hippocampus than patients with a higher BMI. The linear relationship is statistically significant since both p-values are smaller than the chosen alpha level (0.05). The number of data points for high BMI is sparse. Consequently, the models have larger error bands in this area.

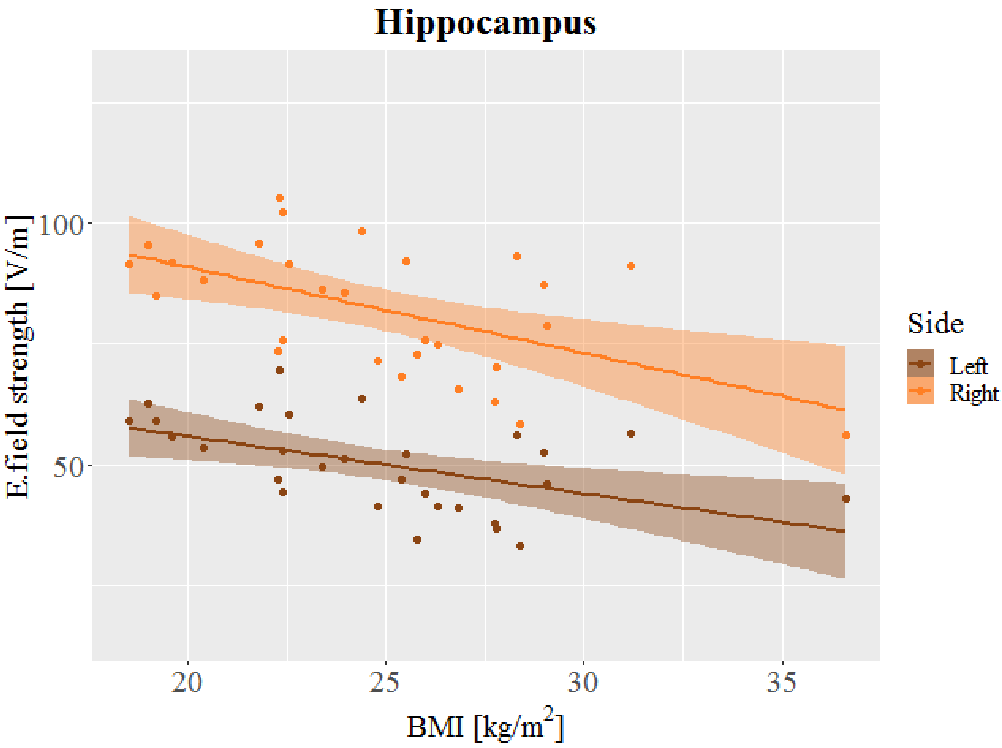

Figure 4.3: *Average electric field strength in the left and right hippocampus versus BMI. Statistical significant relationship on the left (r=-0.51, p=0.005, t=-3.05 and df=27) and right side (r=-0.55, p=0.002, t=-3.41 and df=27).*

Table 4.1: *Statistical values for the linear models of average EF strength in the left and right hippocampus based on the variable BMI.*

$EF_{Left.Hippo} \sim BMI$						
	Estimate	**SE**	**t**	**p**	**Adj. R^2**	**F**
BMI	-1.18	0.39	-3.05	0.005	0.23	9.3
$EF_{Right.Hippo} \sim BMI$						
	Estimate	**SE**	**t**	**p**	**Adj. R^2**	**F**
BMI	-1.78	0.52	-3.41	0.002	0.28	11.6

An estimate of the BMI coefficient, found in Table 4.1, tells that the EF strength in the left hippocampus decreases with -1.18 V/m when BMI increases with one, for the model

$$\mathbf{EF_{Left.Hippo}} = \beta_0 + \beta_{BMI}\mathbf{BMI} + \mathbf{e}.$$

The p-value suggests that the probability of achieving a t-value equal to or larger than the one observed if $\beta_{BMI} = 0$ is small. The model is statistically significant but only explains 23 % of the variation in the EF strength in the left hippocampus. By looking at the estimated value for the BMI coefficient in Table 4.1 for the EF strength model in the right hippocampus,

$$\mathbf{EF_{Right.Hippo}} = \beta_0 + \beta_{BMI}\mathbf{BMI} + \mathbf{e},$$

it can be observed that this model decreases faster than the one for $EF_{Left.Hippo}$. The model for the right hippocampus have statistical values in the same order of magnitude as the model for the left hippocampus and explains 28 % of the variation of EF strength in the right hippocampus.

Regions of Interest

The EF strength plotted against BMI for hippocampus, amygdala, thalamus and caudate is shown in Figure 4.4. EF strength in all the ROIs has a clear negative correlation with BMI. The linear relationship is statistically significant in all the ROIs except the right caudate. The significant *r* values range between -0.56 and -0.46. Figure 4.4 also illustrate how the EF strength generally is higher in the right hemisphere of the brain compared to the left. This is as expected based on the electrode placement (RUL ECT) and that the electric field decrease with the square of the distance from the source (Equation 2.12).

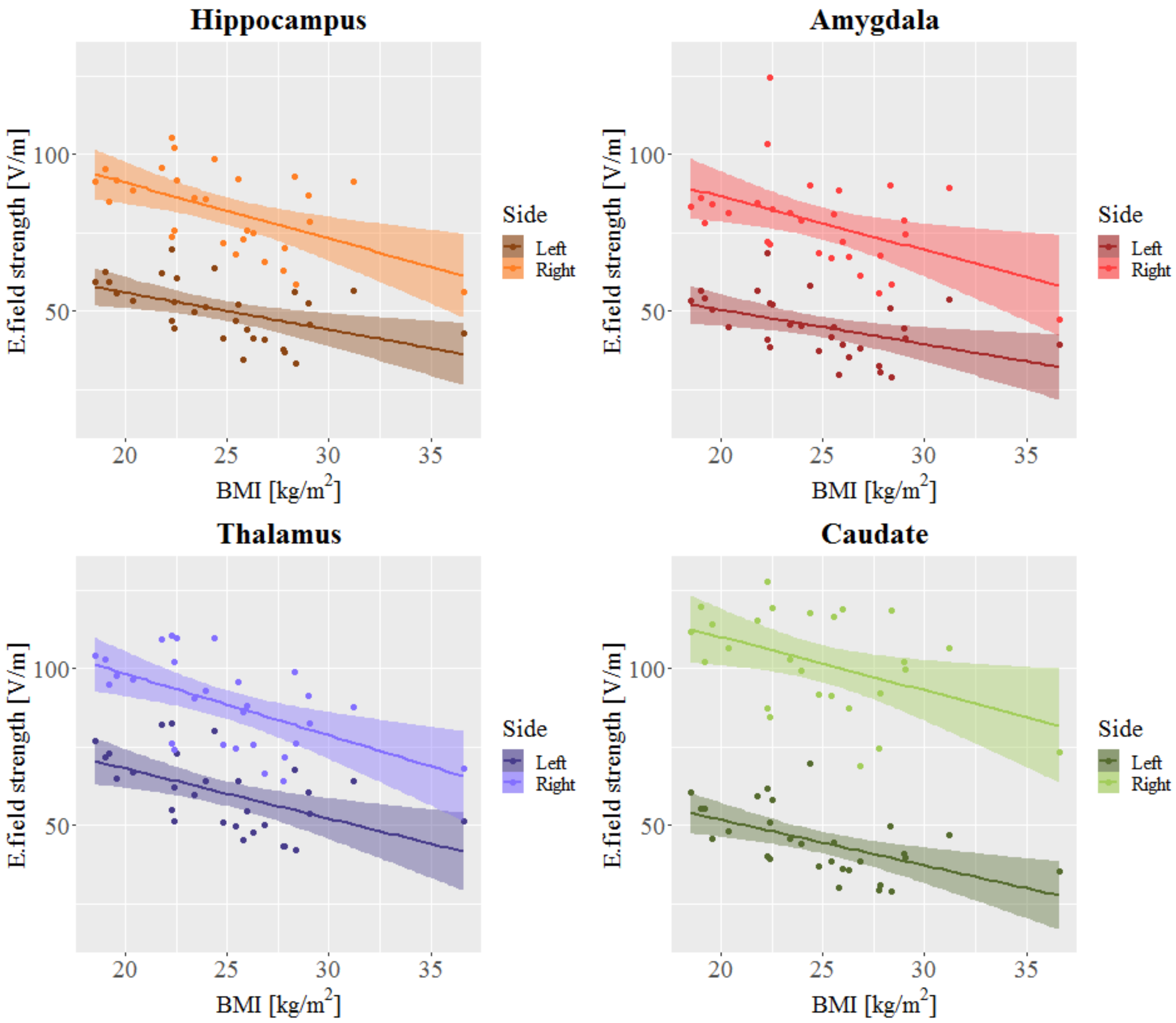

Figure 4.4: *Average EF strength in the hippocampus, amygdala, thalamus and caudate versus BMI. Statistical significant relationship in the left hippocampus (r=-0.51, p=0.005, t=-3.05 and df=27), right hippocampus (r= -0.55, p=0.002, t=-3.41 and df=27), left amygdala (r=-0.46 , p=0.01, t=-2.7 and df=27), right amygdala (r=-0.46 , p=0.01, t=-2.7 and df=27), left thalamus (r=-0.53 , p=0.003, t=-3.29 and df=27), right thalamus (r=-0.56, p=0.002, t=-3.51 and df=27) and left caudate(r=-0.55 , p=0.002, t=-3.43 and df=27). No significant relationship in the right caudate (r=-0.32 , p=0.09, t=-1.75 and df=27).*

4.1.2 Effect of Age

To investigate whether there is a linear connection between the EF strength and age was motivated by the fact that the conducting properties of the head seem to change with age (see subsection 2.1.4). A significant negative correlation was found between age and EF strength in both the left and right hippocampus. Hence, according to these linear models, the EF strength in the hippocampus for an older person would generally be lower than for a younger person when exposed to ECT treatment with a steady current of 900 mA.

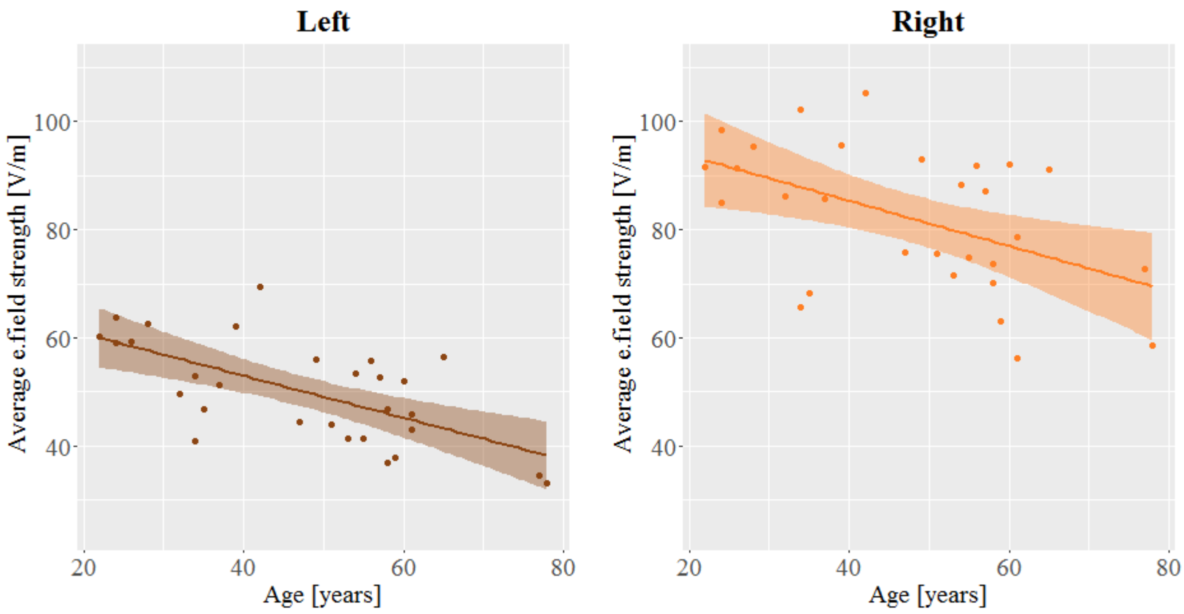

Figure 4.5: *Average electric field strength in the left and right hippocampus versus age. The relationship is statistically significant on the left side (r=-0.64, p=0.0002, t=-4.33 and df=27) and the right side (r=-0.50, p=0.006, t=-2.96 and df=27).*

4.1.3 Effect of Sex

The stimulus dose for each patient was corrected for sex-specific differences (section 3.2). This is the reason why EF strength differences with respect to sex were investigated. Figure 4.6 shows a clear difference in the EF strength in the hippocampus between female (F) and male (M) patients. This difference is statistically significant in both the left and right hippocampus ($t_{left} = -4.13$, $p_{left} < 0.001$; $t_{right} = -4.79$, $p_{right} < 0.0001$). The negative correlations mean that going from female (0) to male (1) will result in a decrease in EF strength in the left and right hippocampus.

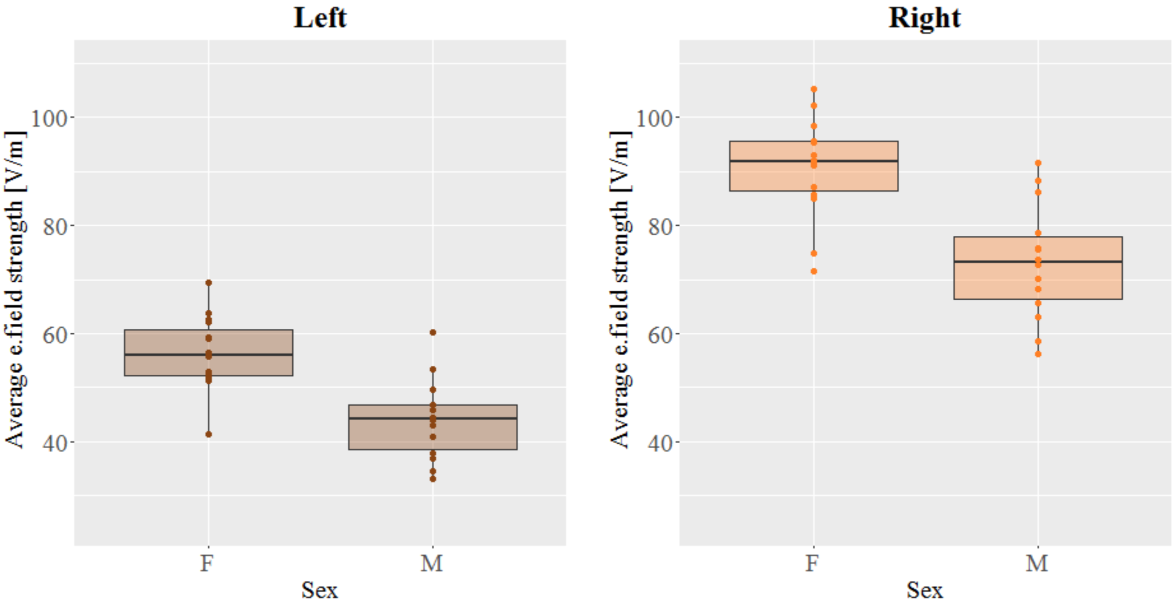

Figure 4.6: *Average electric field strength in the left and right hippocampus versus sex. The difference in average electric field strength between the sexes is statistically significant on the left (r=-0.62, p=0.0003, t=-4.13 and df=27) and the right side (r=-0.68, p=0.00005, t=-4.79 and df=27).*

4.1.4 Effect of Intracranial Volume

Figure 4.7 shows the EF strength plotted against the estimated total intracranial volume (eTIV). The EF strength decrease with the square of the distance (Equation 2.12). Therefore, it would be expected that large heads would have smaller EF strength in the hippocampus compared to smaller heads since the length between the electrodes and the hippocampi would be greater for these patients. The results in Figure 4.7 confirms this relationship with significant negative correlation values ($p_{left} < 0.01$; $p_{right} < 0.001$). Hence, this model predicts that a patient with a large head size will get a lower field strength in both the left and right hippocampus than a patient with smaller head size.

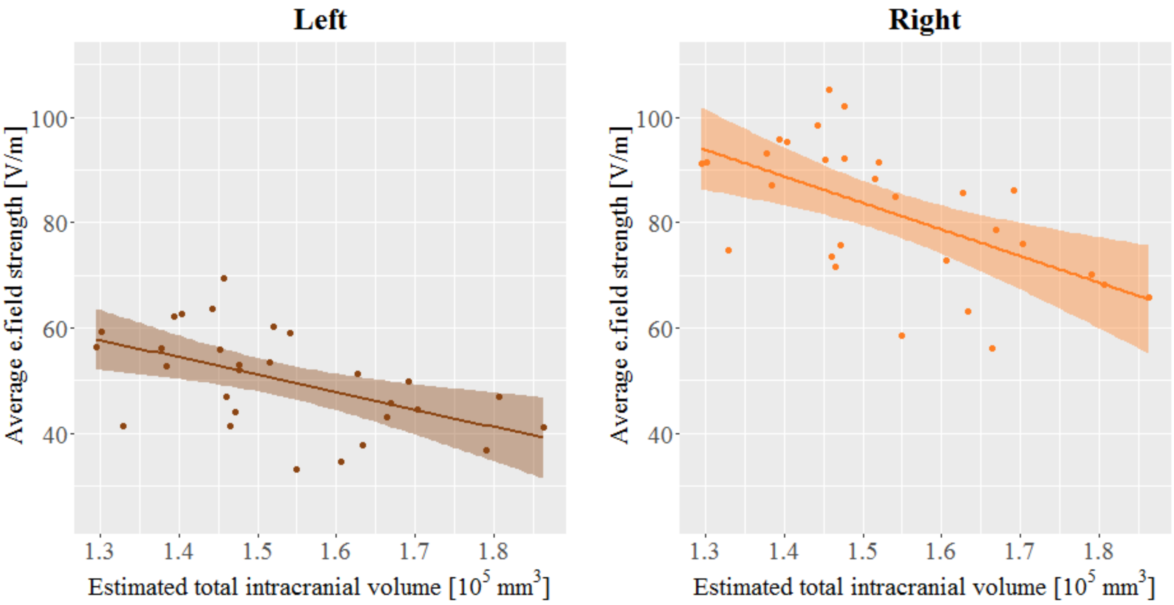

Figure 4.7: *Average electric field strength in the left and right hippocampus versus total estimated intracranial volume. The relationship is statistically significant on the left (r=-0.53, p=0.003, t=-3.22 and df=27) and on the right side (r=-0.58, p=0.00097, t=-3.70 and df=27).*

4.1.5 Effect of Multiple Variables

Correlation between Electric Field Strength, BMI, Age, Sex and Intracranial Volume

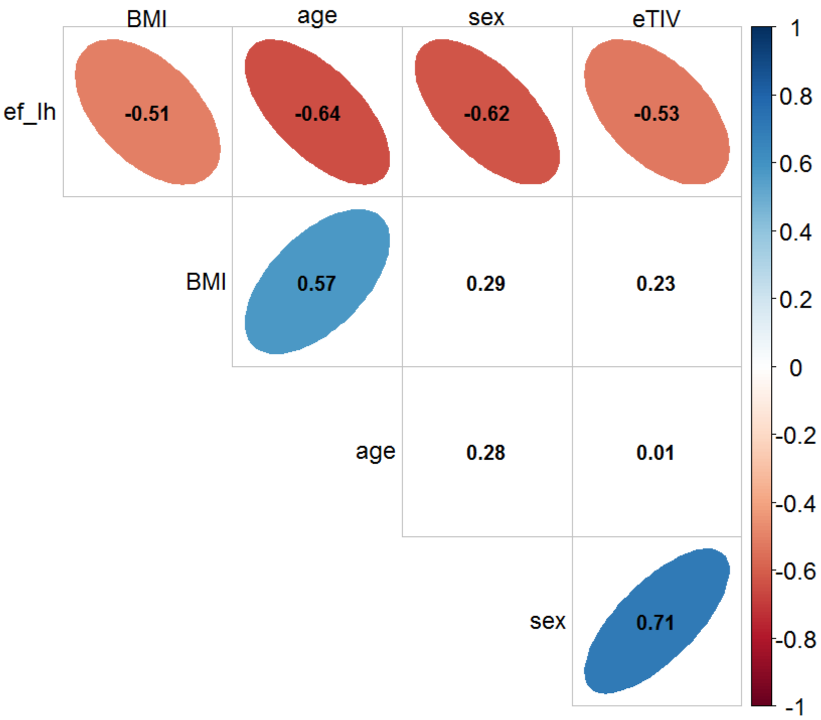

(a) Correlation plot for the variables: average EF strength in the left hippocampus (ef_lh), BMI, age, sex and estimated total intracranial volume (eTIV).

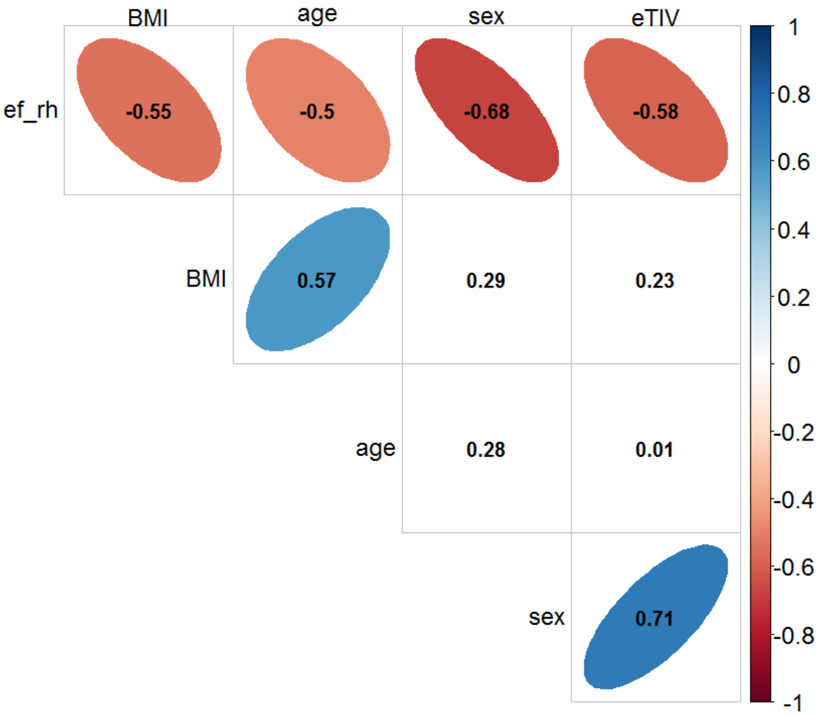

(b) Correlation plot for the variables: average EF strength in the right hippocampus (ef_rh), BMI, age, sex and estimated total intracranial volume (eTIV).

Figure 4.8: *Correlation plot made with corrplot().*

Figure 4.8 shows correlation values between all the selected variables assumed to have an effect on the EF strength. Statistically significant correlation values have an ellipse drawn around them in a colour corresponding to its value. The shape of the ellipse depends on the magnitude of the correlation, where a narrower ellipse means a stronger linear relationship. Orientation of the ellipse matches the sign of the correlation. Positive correlations are tilted to the right, while negative correlations are titled to the left (going from a vertical starting point). The colour depends on the sign of the correlation, and the intensity of the colour depends on the magnitude of the correlation.

Figure 4.8a shows that the EF strength in the left hippocampus ($EF_{Left.Hippo}$) has a strong negative correlation with all the variables assumed to have an effect on it. Furthermore, a significant positive relationship between age and BMI can be observed, indicating that BMI within the patient group increase with age. Moreover, a strong correlation is to be found for eTIV and sex, demonstrating that female patients generally have smaller heads than male patient.

Correlation with all the variables correlating with $EF_{Left.Hippo}$ was also found for the EF in the right hippocampus ($EF_{Right.Hippo}$) and can be seen in Figure 4.8b. The linear relationship between $EF_{Right.Hippo}$ and BMI, sex and eTIV are a little bit stronger than the relationship $EF_{Left.Hippo}$ has with the same variables. The correlation between $EF_{Right.Hippo}$ and age is weaker compared to $EF_{Left.Hippo}$.

BMI, age, sex and eTIV were used as explanatory variables in two multiple linear regression models for the response variables $EF_{Left.Hippo}$ and $EF_{Right.Hippo}$. The correlation values between explanatory variables and the response variables are gathered in Table 4.2.

Table 4.2: *Pearson's correlation between the average electric field strength (EF) in the hippocampus and the variables: BMI, age, sex and total estimated intracranial volume (eTIV).*

Pearson's correlation values, r				
	BMI	**Age**	**Sex**	**eTIV**
$\mathbf{EF_{Left.Hippo}}$	-0.51	-0.64	-0.62	-0.53
$\mathbf{EF_{Right.Hippo}}$	-0.55	-0.50	-0.68	-0.58

Multiple Linear Regression with Normalised Variables

Table 4.3 shows the estimated coefficients and the statistical values of the model,

$$\mathbf{EF}_{Left.Hippo} = \beta_0 + \beta_1\mathbf{BMI} + \beta_2\mathbf{age} + \beta_3\mathbf{sex} + \beta_4\mathbf{eTIV} + \mathbf{e},$$

after normalising the variables to have a range between 0 and 1. First, it shows that the estimated intercept is $66.7 \pm 2.8\,\mathrm{V/m}$. The intercept is the EF strength when all of the explanatory variables take on the lowest measured value (for sex, that means female). By looking at the estimated coefficients in Table 4.3, a negative relationship between EF strength and all the variables is observed. It is clear that age and eTIV have the greatest effect on EF strength in the left hippocampus. These are also the only two statistically significant coefficients in the model. Age have the most negative coefficient, a t-value of -3.5 and a $p(>|t|) < 0.01$, while the coefficient of eTIV is smaller in magnitude and has a t-value of -2.2 and $p(>|t|) < 0.05$. Of the four predicting variables, BMI has the least effect on $EF_{Left.Hippo}$ in this model, with an estimated coefficient of $-1.8 \pm 6.1\,\mathrm{Vm/kg}$. The whole model has a $p = 6 \cdot 10^{-6}$, meaning the model is statistically significant, and the null hypothesis that β_i is zero can be rejected. This model explains 64 % of the variation in $EF_{Left.Hippo}$.

Table 4.3: *Statistical values for the linear model of average EF strength in the left hippocampus based on multiple normalised variables.*

$EF_{Left.Hippo} \sim BMI + age + sex + eTIV$							
	Estimate	**SE**	**t**	**p(>|t|)**	**Adj. R^2**	**F**	**p**
Intercept	66.7	2.8	24	$< 2 \cdot 0^{-16}$	0.64	13.7	$6 \cdot 10^{-6}$
BMI	-1.8	6.1	-0.30	0.8			
Age	-19.9	5.1	-3.8	**0.001**			
Sex (M)	-3.3	3.2	-1.0	0.3			
eTIV	-13.7	6.1	-2.2	**0.03**			

In Table 4.4 the estimated coefficients and the statistical values of the model,

$$\mathbf{EF}_{Right.Hippo} = \beta_0 + \beta_1\mathbf{BMI} + \beta_2\mathbf{age} + \beta_3\mathbf{sex} + \beta_4\mathbf{eTIV} + \mathbf{e},$$

can be found. The variables in this model have also been normalised to have a range from 0 to 1 to be able to compare the effect. By studying the estimated coefficients belonging to the model, one sees that the effects from the various variables are of the same order of magnitude. eTIV has the greatest effect on $EF_{Right.Hippo}$. BMI has the second largest effect, age has the third largest, while sex has the smallest effect size. None of the coefficients is statistically significant, but the model as a whole explains 59 % of the variation in $EF_{Right.Hippo}$ and has a p-value of $3 \cdot 10^{-5}$. Therefore, it is a very small probability that all of the coefficients of the predictors β_i are equal to zero.

Table 4.4: *Statistical values for the linear models of average EF strength in the right hippocampus based on multiple normalised variables.*

$EF_{Right.Hippo} \sim BMI + age + sex + eTIV$

	Estimate	**SE**	**t**	**p(>|t|)**	**Adj. R^2**	**F**	**p**
Intercept	102.7	4.2	25	$< 2 \cdot 10^{-16}$	0.59	11.2	$3 \cdot 10^{-5}$
BMI	−13.8	9.0	−1.5	0.1			
Age	−12.4	7.5	−1.7	0.1			
Sex (M)	−8.6	4.8	−1.8	0.09			
eTIV	−14.2	9.1	−1.6	0.1			

When Table 4.3 and Table 4.4 are compared, a clear difference of around 36 V/m in the intercept values is observed, with the right side having the highest value of 102.7 V/m. Furthermore, it seems like BMI and sex have much more impact on the EF strength in the right hippocampus than in the left hippocampus. Additionally, eTIV appears to have approximately the same effect on the EF strength in both the right and left hippocampus. When it comes to age, the EF strength in the left hippocampus depends more on age compared to in the right hippocampus, according to Table 4.3 and 4.4. Age still has an apparent effect on EF strength in the right hippocampus, it is just not as great as on the left side.

4.2 Volume Change

Figure 4.9 shows an example of the volume segmentation in FreeSurfer. As explained in section 3.6, ΔV is the percentage volume change of the segmented structures from tp 1 to tp 3. ΔV will further be referred to as the volume change. This section explores the relationship between volume change (ΔV) and the variables EF strength, age, sex, number of ECT sessions (nECTs), and BMI. No statistical relationship was found for volume change and age, in addition to volume change and BMI. The plots based on these variables are nevertheless presented and discussed, as no findings can be a finding itself, and some of the plots show tendencies to correlate with volume change.

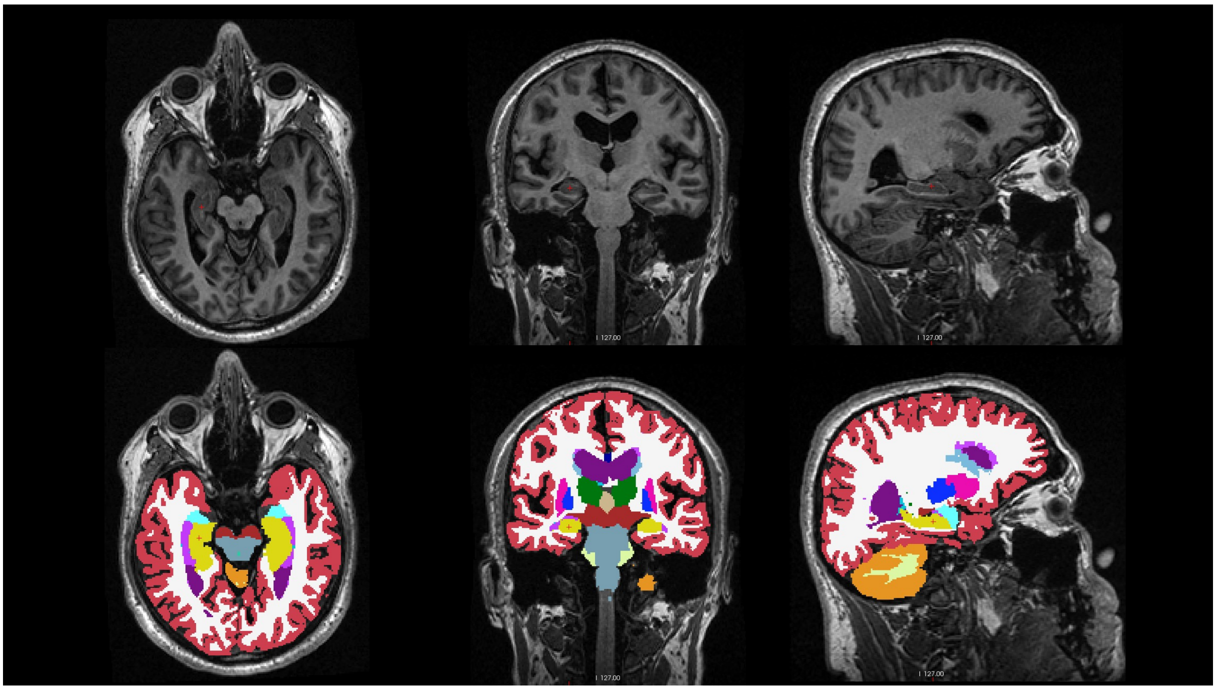

Figure 4.9: *Random participant, MRI 1.* ***Top:*** *Axial, coronal and sagittal view of a T1-weighted MRI (orig.mgz).* ***Bottom:*** *Axial, coronal and sagittal view of the segmentation of subcortical structures (aseg.mgz). Hippocampus is segmented in yellow. The minor red cursor points at the right hippocampus. Labels can be found in Figure 4.10.*

🟩 10 Left-Thalamus
🟦 11 Left-Caudate

🟨 17 Left-Hippocampus
🟦 18 Left-Amygdala

🟩 49 Right-Thalamus
🟦 50 Right-Caudate

🟨 53 Right-Hippocampus
🟦 54 Right-Amygdala

Figure 4.10: *Labels for ROIs in aseg.mgz*

4.2.1 Effect of Electric Field Strength

Hippocampus

In Figure 4.11, plots of the linear regression models $\Delta V_{Left.Hippo} \sim EF_{Left.Hippo}$ and $\Delta V_{Right.Hippo} \sim EF_{Right.Hippo}$ are to be found. The scatter plots represent the individual relationship between ΔV and the EF strength. A significant positive correlation between ΔV and the EF strength in the left hippocampus is seen. However, volume change in the right hippocampus does not seem to increase that rapidly with increasing EF strength, and the correlation is not significant. Both the model for the left and right hippocampus have a maximum volume change of about 4 %.

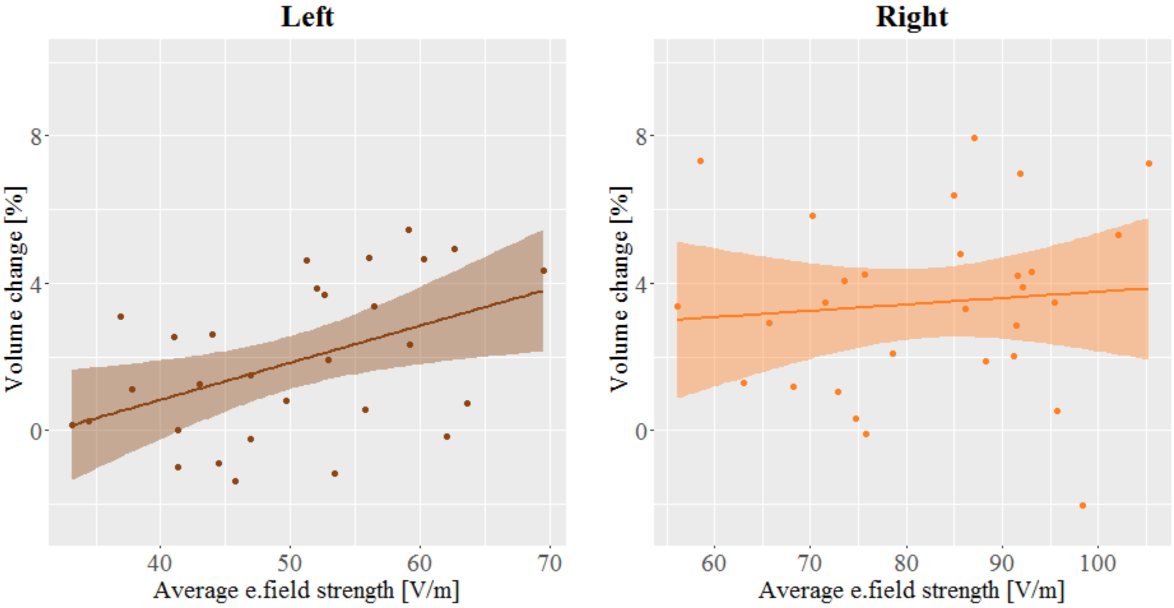

Figure 4.11: *Volume change ΔV versus the average electric field strength in the left and right hippocampus. Statistical significant relationship on the left side (r=0.46, p=0.01, t=2.7 and df=27). Right statistics were not significant.*

Table 4.5: *Statistical values for the linear models of ΔV in the left and right hippocampus based on the variable EF strength.*

$\Delta V_{Left.Hippo} \sim EF_{Left.Hippo}$						
	Estimate	**SE**	**t**	**p**	**Adj. R^2**	**F**
EF	0.00101	0.00038	2.7	0.01	0.18	7.1
$\Delta V_{Right.Hippo} \sim EF_{Right.Hippo}$						
	Estimate	**SE**	**t**	**p**	**Adj. R^2**	**F**
EF	0.00017	0.00037	0.48	0.6	-0.03	0.23

Statistical values and estimated coefficients for the linear models,

$$\Delta \mathbf{V}_{\mathbf{Left.Hippo}} = \beta_0 + \beta_1 \mathbf{EF}_{\mathbf{Left.Hippo}} + \mathbf{e}$$

and

$$\Delta \mathbf{V}_{\mathbf{Right.Hippo}} = \beta_0 + \beta_1 \mathbf{EF}_{\mathbf{Right.Hippo}} + \mathbf{e},$$

are listed in Table 4.5. Table 4.5 tells that the estimated volume change in the left hippocampus increases with 0.10 % with an increase of 1 V/m in the EF strength. In the right hippocampus the increase is 0.02 % per V/m. The t-values are the estimates divided by the standard error (see Equation 3.7). $\Delta V_{Left.Hippo}$ has a high t-value of 2.7 combined with a low p-value of 0.01, meaning the model is statistically significant. The probability of achieving a $|t|$ larger or equal to the observed absolute t-value if the null hypothesis was true is therefore small. Compared with this, the model for the right hippocampus has a low t-value and a high p-value. The p-values for the models are the same as for each predictor since there only is one single predictor in each model.

Regions of Interest

In addition to the hippocampus, the volume change versus the EF strength was plotted for the amygdala, thalamus and caudate (see Figure 4.12). Of the eight ROIs, the left amygdala has the strongest relationship between volume change and EF strength ($r = 0.60, p = 0.0005$). In all the ROIs, there is a stronger relationship on the left side compared to the right. However, only EF strength in the left hippocampus ($r = 0.46, p = 0.01$) and the left amygdala have a statistically significant correlation with volume change.

Furthermore, the right side ROIs generally experience higher EF strengths than the corresponding left side ROIs. Of all the ROIs, the right caudate experiences the strongest EF. The regression line for this ROI is almost horizontal. Hence the EF strength seems to have no effect on the volume change in the right caudate. An increase in the EF strength does not seem to have considerable influence on the volume change model in the right thalamus either. The right thalamus has a volume change of less than one percentage going from around 65 to 110 V/m in EF strength. The EF strength hippocampus experiences, compared to the EF strength in the thalamus and caudate, has a clearer role in terms of volume changes. Moreover, the effect seen in the hippocampus is vaguer than in the amygdala.

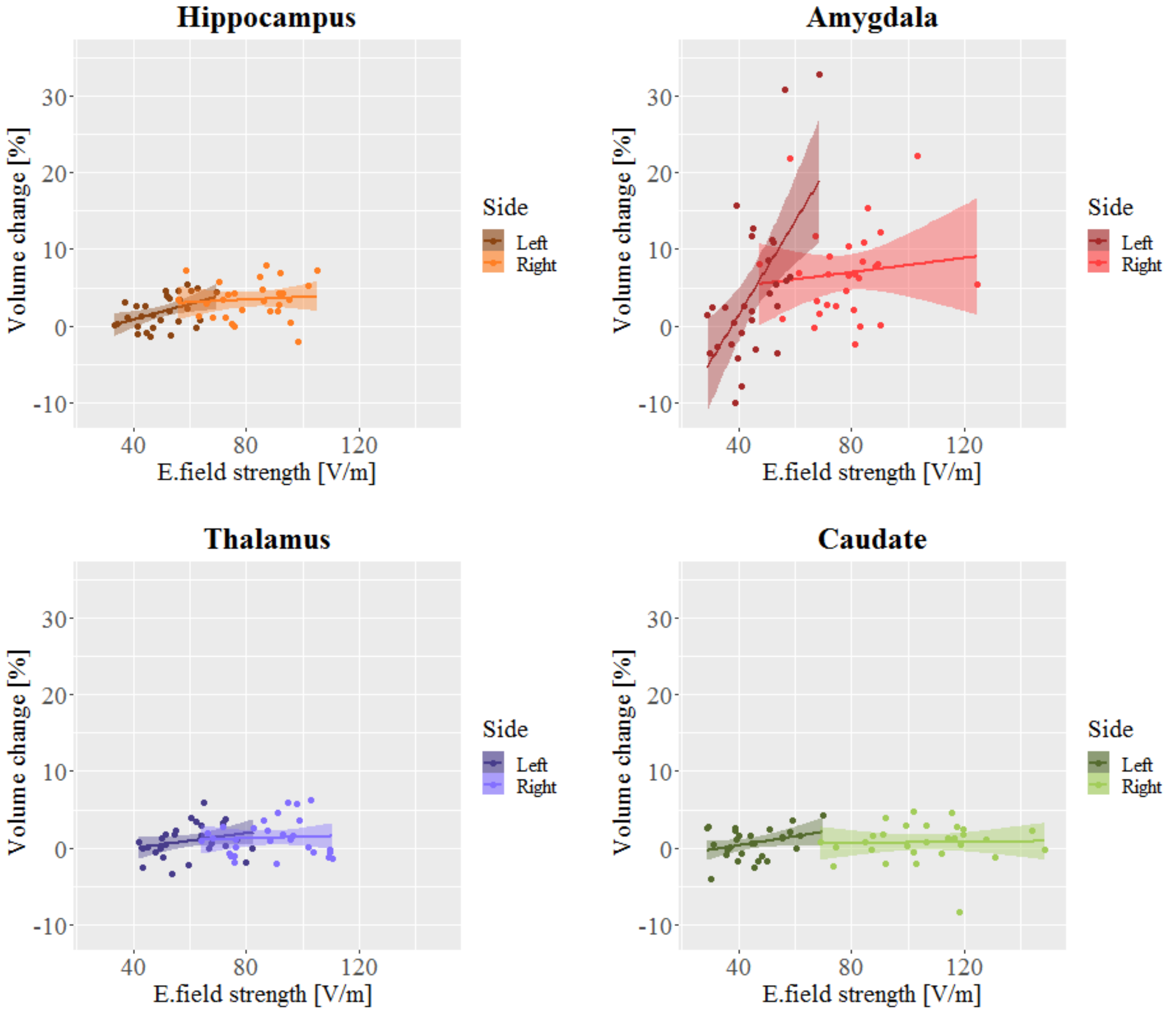

Figure 4.12: Volume change versus average electric field strength in the hippocampus, amygdala, thalamus and caudate. Statistically significant relationship in the left hippocampus (r=0.46, p=0.01, t=2.7 and df=27) and the left amygdala (r=0.60, p=0.0005, t=4.0 and df=27)

.

4.2.2 Effect of Age

No significant correlation was found on either the left or the right side. Age has a negative effect on volume change in the left hippocampus (brown) in Figure 4.13. Furthermore, the volume change in the right hippocampus (orange) appears to be positively correlated with age. The absolute magnitude of the left slope (brown) is greater than the absolute magnitude of the right slope (orange). But again, no statistically significant relationship was found in either case.

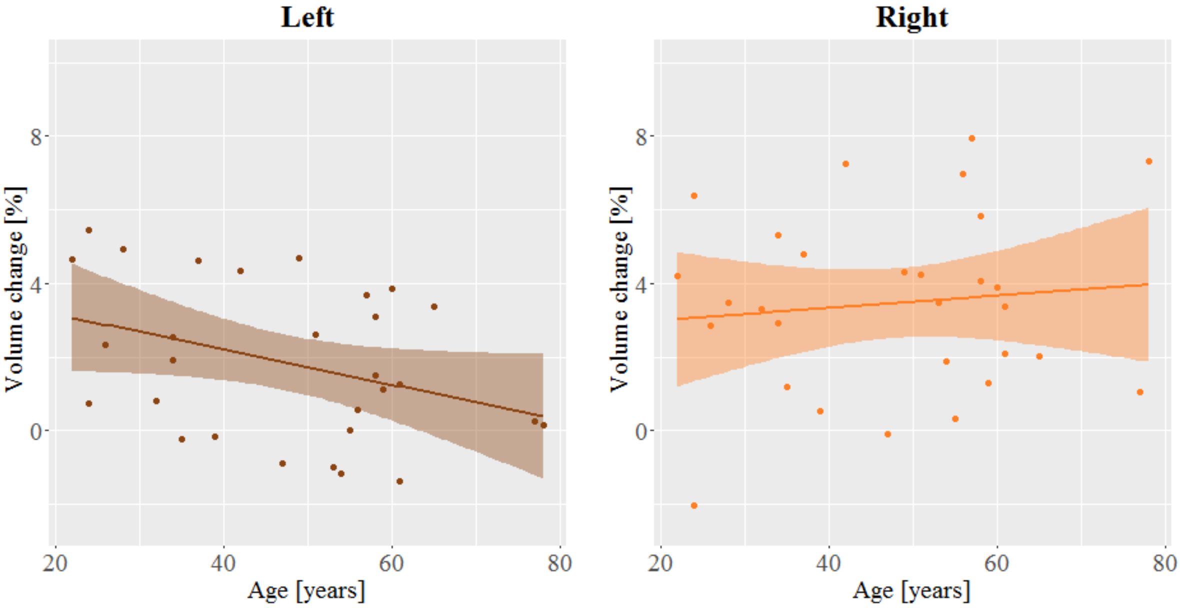

Figure 4.13: *Volume change in the left and right hippocampus versus age. No statistically significant relationship was found on either the left or the right side.*

4.2.3 Effect of Sex

Figure 4.14 shows that the hippocampi in women on average undergo larger volume change during ECT than in men. This difference is statistically significant ($p = 0.04$) for the left hippocampus (brown), where the median of volume change is between 3-4 % for the female patients, and around 1 % for male patients. At the same time, the volume measurements for women have a larger variance than the measurements for men. According to the box plots in Figure 4.14 both women and men have larger volume changes in the right hippocampus than in the left.

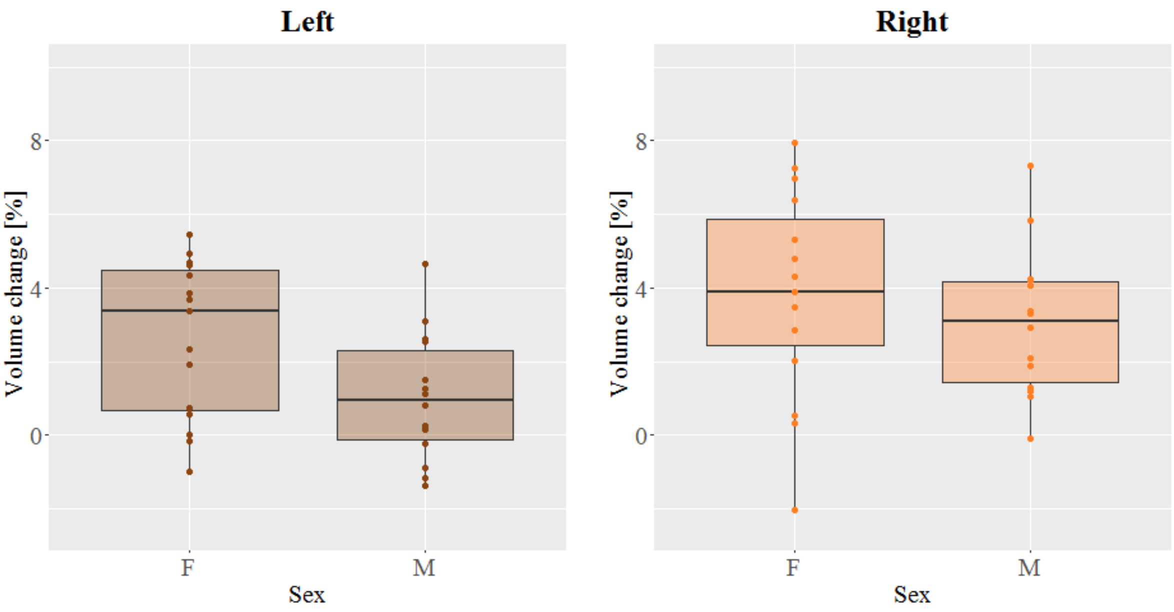

Figure 4.14: *Volume change in the left and right hippocampus versus sex. The difference in volume change between the sexes is statistically significant on the left side (r=-0.36, p=0.04, t=-2.2 and df=27). There is no significant difference on the right side.*

4.2.4 Effect of Number of ECT Sessions

In Figure 4.15, a significant positive correlation between volume change in the right hippocampus (orange) and the number of ECT sessions (nECTs) can be observed ($r = 0.46, p = 0.01$). This model predicts that patients receiving ECT treatment will experience greater volume changes in the right hippocampus with increasing ECT sessions. The linear relationship between ΔV and nECTs on the left side is not significant.

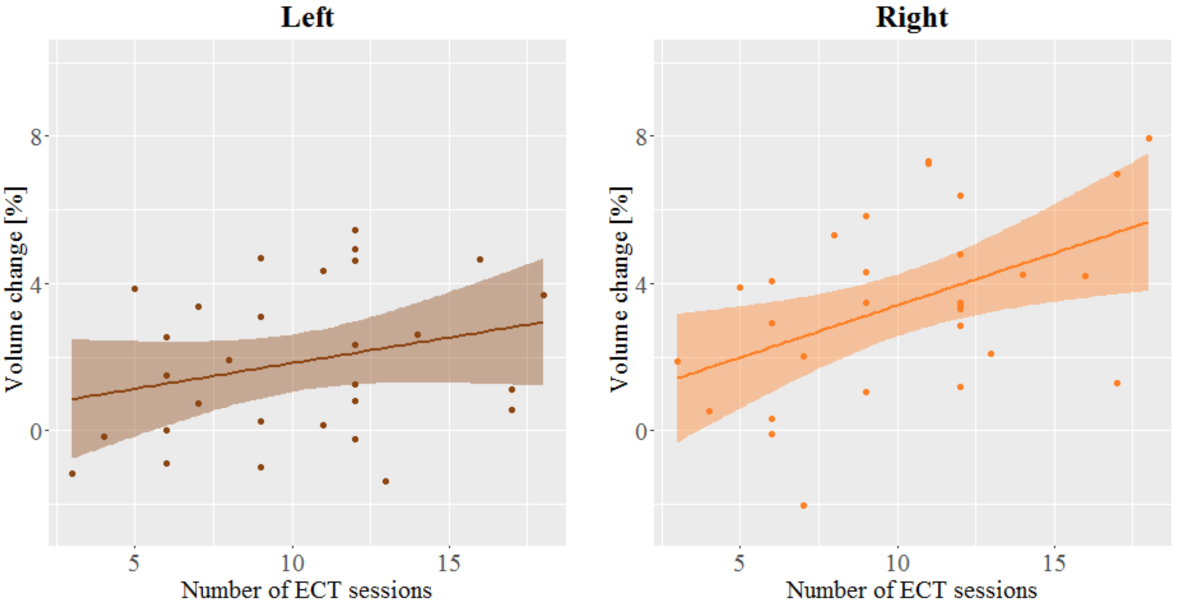

Figure 4.15: *Volume change in the left and right hippocampus verus total number of ECT sessions. The relationship is significant on the right side (r=0.46, p=0.01, t=2.7 and df=27). There is no statistical significant relationship on the left side.*

4.2.5 Effect of BMI

Figure 4.16 shows the volumetric change in the left and right hippocampus plotted against BMI. There is a tendency for the volume change of being negatively affected by increasing BMI in both hippocampi (but this is not significant).

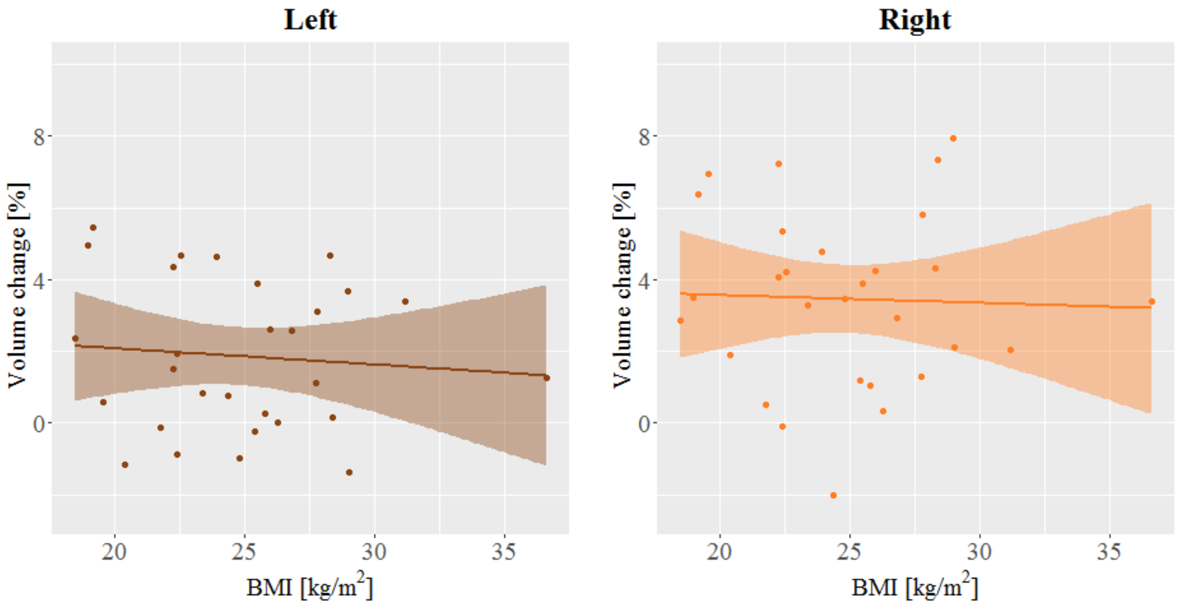

Figure 4.16: *Volume change in the left and right hippocampus versus BMI. No statistically significant relationship was found on either the left or the right side.*

4.2.6 Effect of Multiple Variables

Correlation between Volume Change, EF Strength, Age, Sex, Number of ECTs and BMI

Figure 4.17 shows the correlation values between ΔV, EF strength, age, sex, number of ECT sessions (nECTs) and BMI. In Figure 4.17a, one can see that $\Delta V_{Left.Hippo}$ correlates positively with $EF_{Left.Hippo}$ ($r = 0.46$) and negatively with sex ($r = -0.39$), meaning the volume change seem to be greater when exposed to a greater $EF_{Left.Hippo}$, and male patient appear to have smaller volume changes in the left hippocampus than female patients. Furthermore, sex has a strong significant negative linear relationship with $EF_{Left.Hippo}$ ($r = 0.62$), demonstrating that male patients tend to have weaker $EF_{Left.Hippo}$ compared to female patients. This is illustrated in subsection 4.1.3.

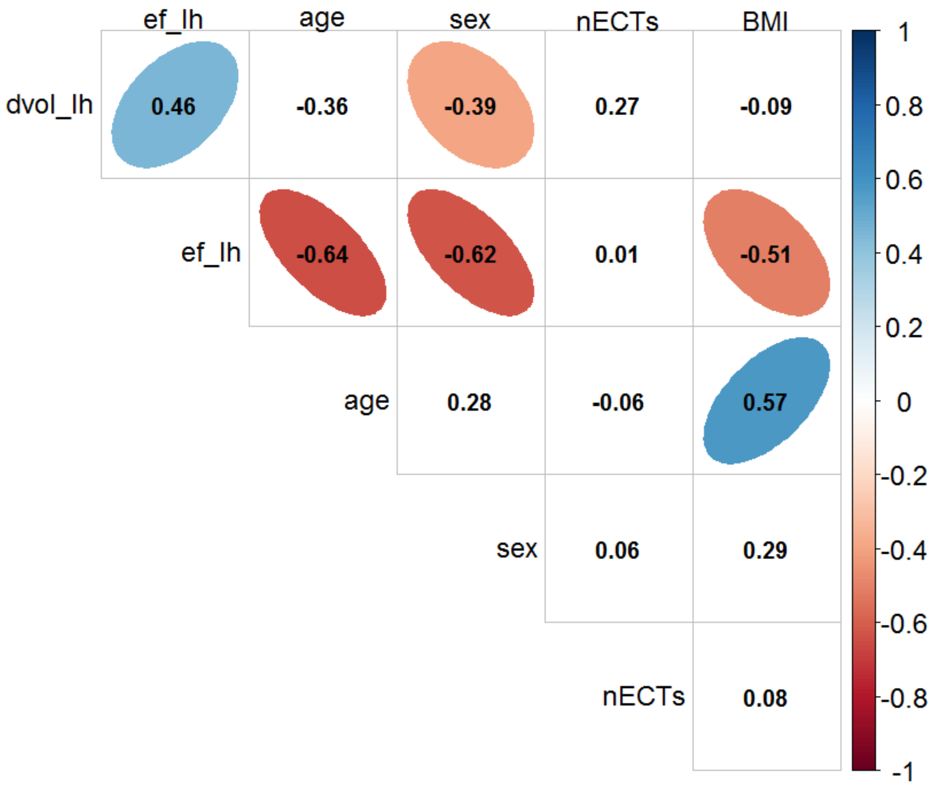

(a) Correlation plot for the variables: volume change in the left hippocampus (dvol_lh), average EF strength in the left hippocampus (ef_lh), age, sex, number of ECT sessions (nECTs) and BMI.

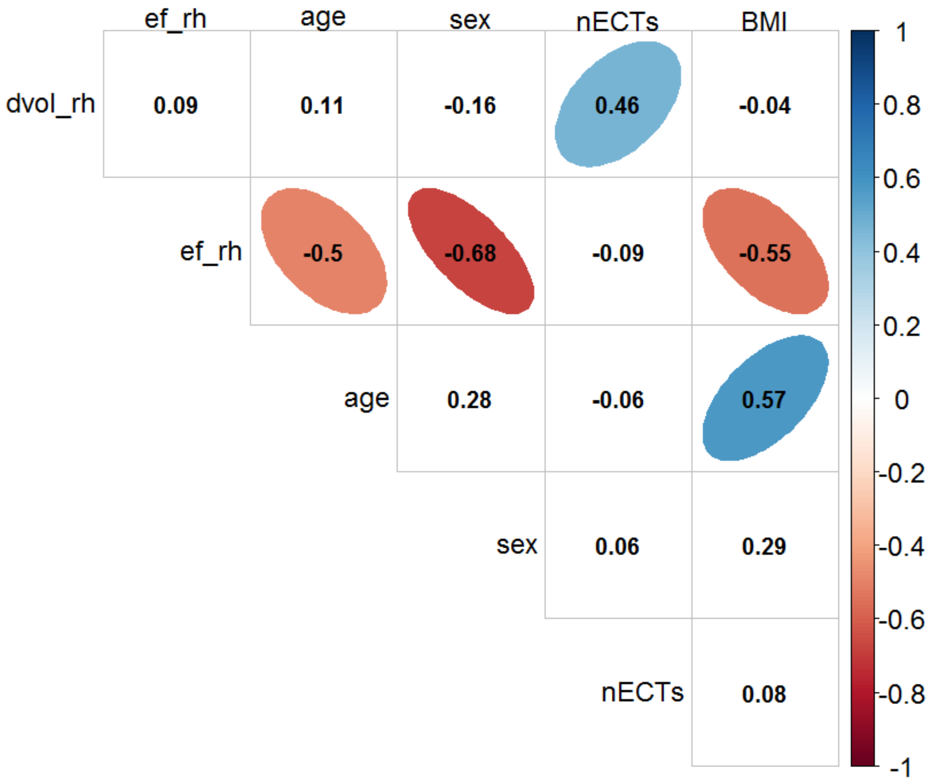

(b) Correlation plot for the variables: volume change in the right hippocampus (dvol_rh), average EF strength in the right hippocampus (ef_rh), age, sex, number of ECT sessions (nECTs) and BMI.

Figure 4.17: *Correlation plot made with corrplot().*

Figure 4.17b shows that volume change in the right hippocampus only correlates with nECTs ($r = 0.46$) of the variables present in the correlation plot. The few significant correlation values for volume change is gathered in Table 4.6.

Table 4.6: *Pearson's correlation between the volume change in the hippocampus and the variables: Electric field strength (EF), age, number of ECT treatments (nECT) and BMI. Only statistically significant values are shown.*

Pearson's correlation values, r					
	EF	**Age**	**Sex**	**nECTs**	**BMI**
$\Delta\mathbf{V}_{\mathbf{Left.Hippo}}$	0.46		−0.39		
$\Delta\mathbf{V}_{\mathbf{Right.Hippo}}$				0.46	

EF strength, age, sex, nECTs and BMI were used as explanatory variables in the multiple linear regression models for $\Delta V_{Left.Hippo}$ and $\Delta V_{Right.Hippo}$.

Multiple Linear Regression with Normalised Variables

In Table 4.7, the estimated coefficients for the multiple linear regression model,

$$\Delta\mathbf{V}_{\mathbf{Left.Hippo}} = \beta_0 + \beta_1\mathbf{EF} + \beta_2\mathbf{age} + \beta_3\mathbf{sex} + \beta_4\mathbf{nECT} + \beta_5\mathbf{BMI} + \mathbf{e},$$

with additional statistical values for each estimate and the model as a whole can be found. The model has no statistically significant coefficients and the model as a whole is not significant either (*p=0.06*).

Table 4.8 shows that the multiple linear regression model,

$$\Delta\mathbf{V}_{\mathbf{Righ.Hippo}} = \beta_0 + \beta_1\mathbf{EF} + \beta_2\mathbf{age} + \beta_3\mathbf{sex} + \beta_4\mathbf{nECT} + \beta_5\mathbf{BMI} + \mathbf{e},$$

has one significant coefficient. The positive coefficient for nECT of 0.047 tells that the volume change increases with 4.7 % if the number of ECT sessions is increased from the minimum (3 session) to the maximum (18 session) measured value in this study. The model as a whole turned out not to be statistically significant (*p=0.09*), meaning the null hypothesis that β_i is zero could not be rejected.

Table 4.7: *Statistical values for the linear model of ΔV in the left hippocampus based on multiple normalised variables.*

$\Delta V_{Left.Hippo} \sim EF + age + sex + nECT + BMI$							
	Estimate	**SE**	**t**	**p(>|t|)**	**Adj. R^2**	**F**	**p**
Intercept	0.0042	0.0204	0.20	0.8	0.21	2.4	0.06
EF	0.022	0.022	0.99	0.3			
Age	−0.017	0.018	−0.96	0.3			
Sex (M)	−0.0097	0.0090	−1.1	0.3			
nECT	0.019	0.013	1.4	0.2			
BMI	0.022	0.020	1.1	0.3			

Table 4.8: *Statistical values for the linear model of ΔV in the right hippocampus based on multiple normalised variables.*

$\Delta V_{Right.Hippo} \sim EF + age + sex + nECT + BMI$							
	Estimate	**SE**	**t**	**p(>|t|)**	**Adj. R^2**	**F**	**p**
Intercept	0.0048	0.0254	0.19	0.9	0.17	2.2	0.09
EF	0.0083	0.0254	0.33	0.8			
Age	0.029	0.019	1.5	0.1			
Sex (M)	−0.0086	0.011	−0.76	0.5			
nECT	0.047	0.016	3.0	**0.007**			
BMI	−0.018	0.025	−0.74	0.5			

4.3 Dose

This section presents the relationship between volume change and dose, where the dose is the average dose, cumulative dose and field exposure.

4.3.1 Average Dose

Figure 4.18 illustrates the volume change of different intracerebral structures after a treatment series versus the average dose given for an ECT session. No correlation is found for most of the ROIs, while both positive and negative correlations are found for some of them. This variation is probably because an average dose corresponds to *one* session and not the whole treatment as the volume change does.

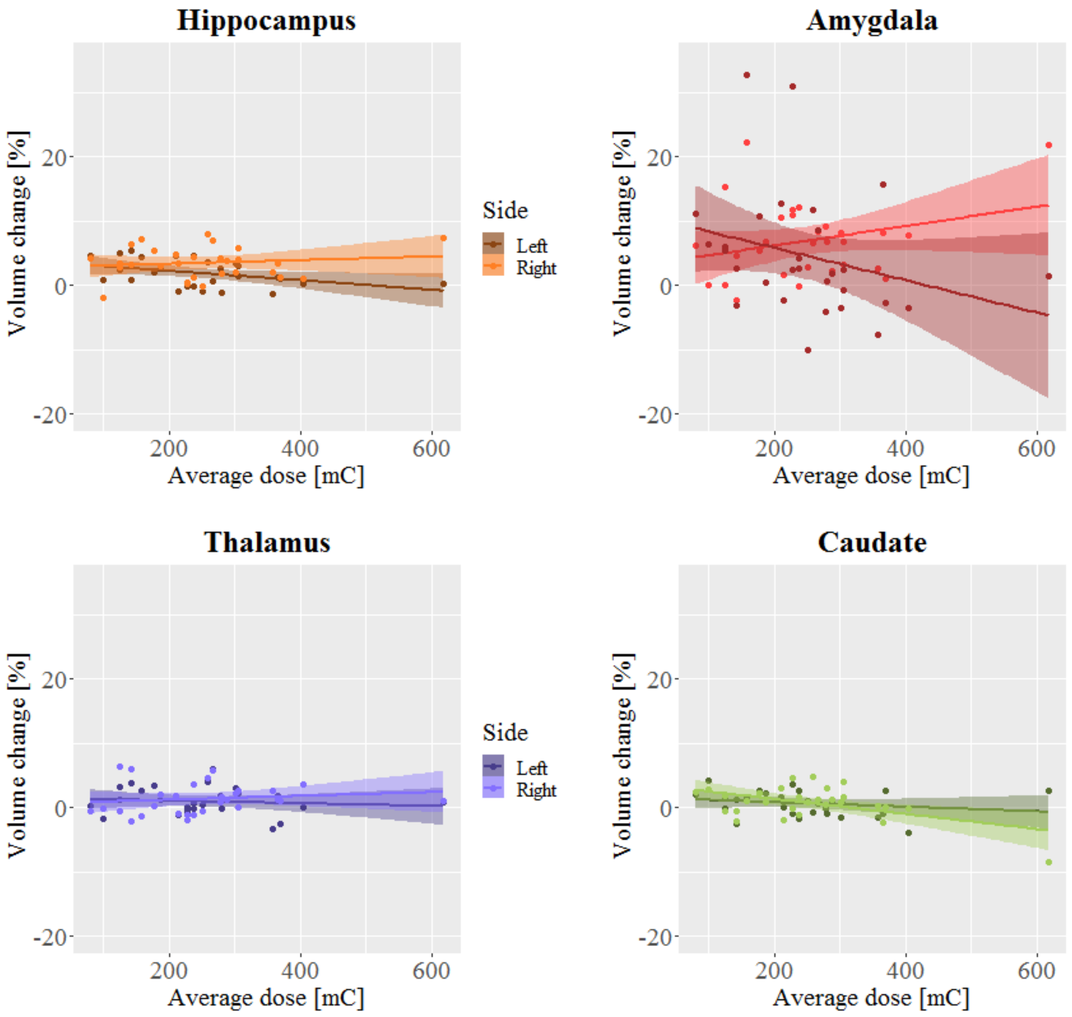

Figure 4.18: *Volume change versus average stimulus dose in the hippocampus, amygdala, thalamus and caudate.*

4.3.2 Cumulative Dose

A clearer relationship between volume change and the cumulative dose was expected as both variables correspond to the entire treatment period. However, Figure 4.19 shows results with the same tendencies as the results seen in Figure 4.18. The relationship seems random, and the cumulative dose does not seem to affect the volume change in the ROIs.

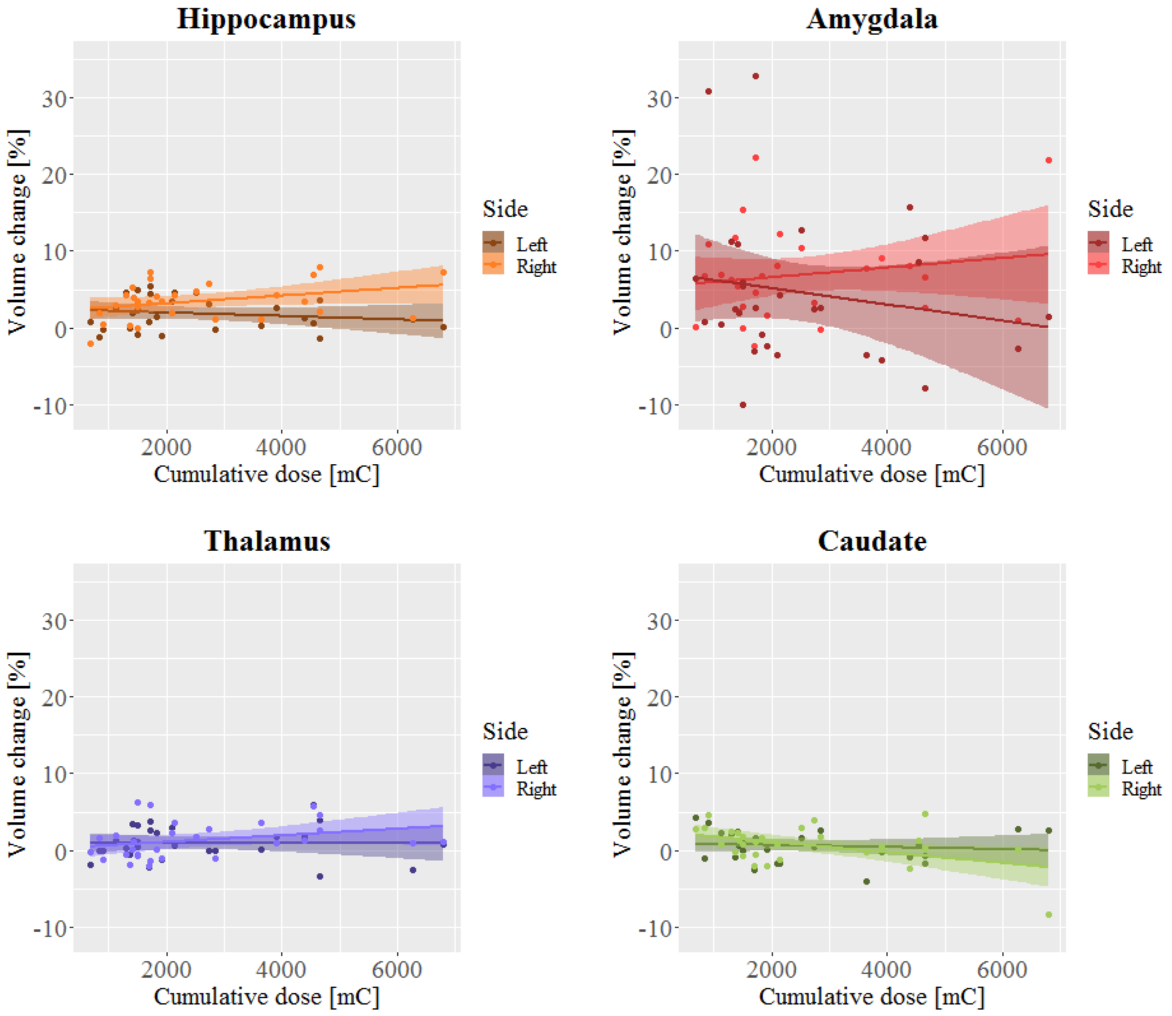

Figure 4.19: *Volume change versus cumulative stimulus dose in the hippocampus, amygdala, thalamus and caudate.*

4.3.3 Field Exposure

Since neither of the two previous dose concepts seemed to have an effect on volume change, an attempt was made to find a dose concept that described what was happening inside the ROIs instead of outside. Field exposure FE is defined by Equation 4.1, and is the average electric field strength $\overline{|\mathbf{E}|}$ in a structure multiplied with the exposure time T_e (see Equation 3.1).

$$FE = \overline{|\mathbf{E}|} \cdot T_e \tag{4.1}$$

Volume change in the left and right hippocampus plotted against the field exposure can be seen in Figure 4.20. The positive correlation ($r = 0.44$) on the right side (orange) is statistically significant ($p = 0.02$), and the model for volume change in the right hippocampus increase with approximately 3 % when the field exposure goes from around 75 to 460 Vs/m. No significant relationship can be seen in the left hippocampus from this plot.

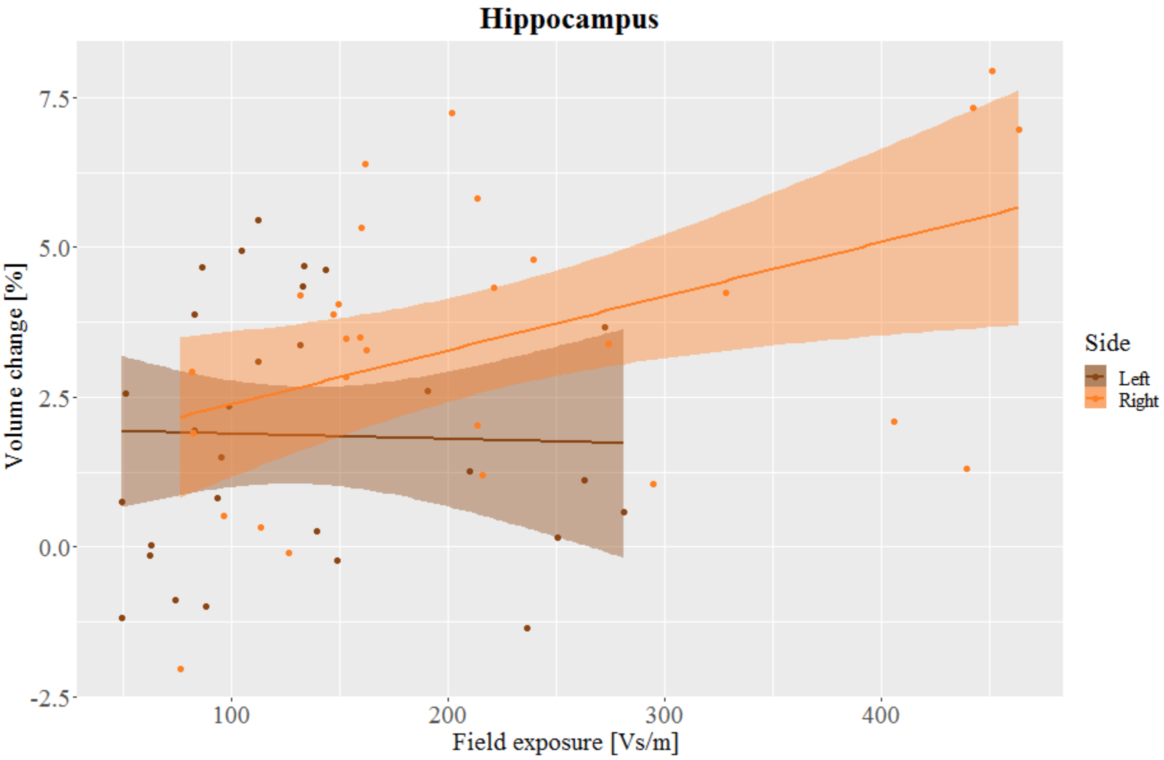

Figure 4.20: *Volume change versus the field exposure in the left and right hippocampus. The relationship is statistically significant on the right side ($r = 0.44$, $p = 0.02$, t=2.56 and df=27).*

It was assumed that the right and left hippocampus would respond in the same way if exposed to the same field exposure. On this basis, a model was created that includes volume changes from both the right and left hippocampus. This linear model and the individual responses can be seen in Figure 4.21. A significant positive correlation is observed ($r = 0.37$, $p = 0.004$).

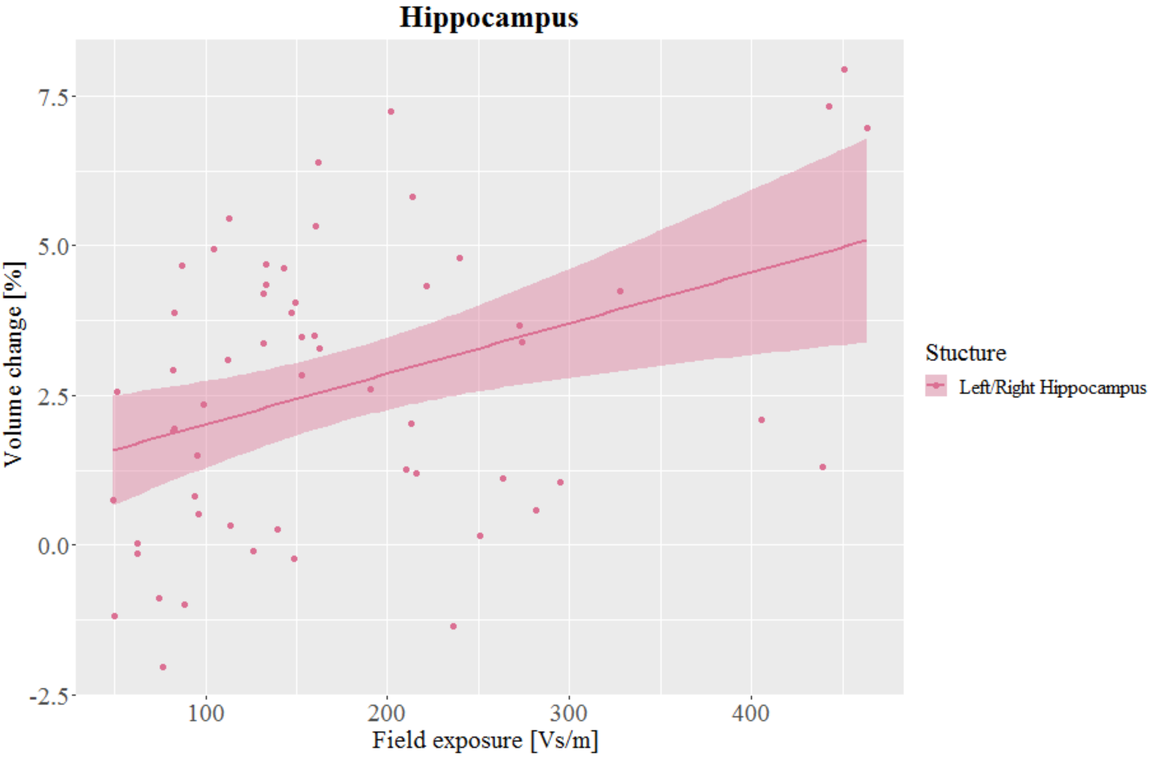

Figure 4.21: *Volume change versus the field exposure in the hippocampi. The relationship is statistically significant (r=0.37, p=0.004, t=3.05 and df=56).*

Table 4.9 summarises the statistics for the model $\Delta V_{Hippo} \sim FE$ seen in Figure 4.21. It shows that the model explains 13 % of the variation in ΔV_{Hippo} and that the probability is small of finding a t-value higher or equal to 3.05 if the true value of the coefficient was zero. The probability is 0.004, meaning the model is statistically significant.

Table 4.9: *Statistical values for the linear model of* ΔV *in the hippocampi based on the variable field exposure (FE).*

$\Delta V_{Hippo} \sim FE$						
	Estimate	**SE**	**t**	**p**	**Adj. R^2**	**F**
$\mathbf{EF \cdot T_e}$	$8.46 \cdot 10^{-5}$	$2.77 \cdot 10^{-5}$	3.05	0.004	0.13	9.3

Chapter 5

Discussion

The goal of this master project was to investigate how well the age-based method takes into account individual differences and ensures equal treatment effects. Correlation values and linear regression models have been studied to examine whether there was significant variation in volume change and electric field strength between individuals with respect to BMI, age, sex, number of ECT sessions and intracranial volume. The same methods were used to quantify the volumetric changes of the hippocampus after ECT with respect to both the electric field strength and different dose concepts. To study the distribution, volumetric changes and electric field strengths were investigated in different regions; left/right hippocampus, left/right amygdala, left/right thalamus and left/right caudate. This chapter discusses the results from chapter 4, in addition to the limitations of the methods.

5.1 Electric Field Strength

From Figure 4.2, and by studying multiple images of the electric field strength distribution, it can be seen that the EF strength have high values underneath the two electrodes and in the skull (especially close to the electrodes and between the electrodes). The skull has low conductivity compared to the scalp (see Table 2.1) and will therefore act as a resistor of greater resistance than the scalp (Equation 2.30). The potential drop over the skull will therefore be larger than over the scalp. Consequently, the gradient of the potential in the skull will be larger than the gradient of the potential in the scalp. Hence, the electric field strength in the skull will be larger than in the scalp by Equation 2.19. The poorly conducting skull will also cause most of the current to flow directly to the other electrode through the scalp, as most of the current follow the path of least resistance. Furthermore, it can be observed that the electric field is inversely proportional to the conductivity (Equation 2.27) in areas consisting of strongly conducting CSF. In these areas, the EF strength is weak. Other than this, the images show that the EF strength tends to get weaker the further away from the two electrodes one moves.

5.1.1 Effect of BMI

The simple linear regression models for $EF \sim BMI$ in the left and right hippocampus seen in Figure 4.3 indicate that BMI has a negative effect on the electric field. A negative effect meaning a higher BMI would lead to a weaker EF in the hippocampi. The effect seems to be a little bit greater on the right side, where the model says that the EF strength decreases with 1.78 V/m in the right hippocampus if BMI increases with one. For both models, the estimated coefficient is statistically different from zero with p-values of 0.005 (left) and 0.002 (right).

Since ROAST does not segment fat but segments the scalp as one layer, the negative correlation between EF strength and BMI is maybe caused by a thicker scalp layer segmented for those with higher BMI. However, considering the high correlation value between BMI and age (*r=0.57*) seen in Figure 4.8, it is not easy to distinguish whether the effect is due to age differences or different BMI. Further investigation is therefore necessary to verify the relationship between BMI and EF strength. By studying a group of participants where everyone was the same age could separate the effects of age from BMI on the EF strength.

There is also a need to study whether there actually is a correlation between BMI and thickness of the cranial subcutaneous fat layer. In subsection 2.1.4, it was shown that low correlation values ($r = 0.19$, $r = 0.29$ and $r = 0.39$) were found for three different cohorts in a study from Bergen. This is not enough to validate the possible relationship between BMI and subcutaneous fat in the head. Additionally, it must be mentioned that a possible source of error is that BMI can be high due to muscle mass and will then most likely not correlate with the thickness of subcutaneous fat.

This negative correlation between EF strength and BMI is also observed in the other grey matter regions of interest; amygdala, thalamus and caudate. The correlation values for all the ROIs except right caudate are between -0.56 and -0.46 and are statistically significant. This indicates that BMI does not only affect the electric field in the hippocampus but affects the electric field in larger areas of the brain. The expectation was that BMI would reduce the EF strength throughout the whole brain, as less current would enter the brain.

If it is confirmed that there is a positive relationship between BMI and cranial subcutaneous fat, and there is a negative correlation between EF strength and BMI, the dose parameters for each patient should be adapted to ensure the same effect of the treatment. The electric field increase and decrease as a function of increasing and decreasing current. Adjusting the amplitude of the stimulus current higher for patients with higher BMI and lower for the patient with lower BMI could be a step towards equal treatment effect. This is based on the belief that it is the electrical stimulus that causes the volume changes and not the seizure.

5.1.2 Effect of Age

The results seen in Figure 4.5 demonstrate that higher age within the patient group was associated with linearly decreasing EF strength in the hippocampus. This could be a result of greater skull thickness with age. ROAST does not segment the skull as a three-layered structure consisting of two compact bone layers and one spongy bone layer in the middle. Therefore, the thickness of the two outer layers needs to grow thicker than the inner layer shrinks, to have an effect on the electric field calculations in ROAST. The decreasing conductivity of the whole skull with age is not considered, but may, to some extent, have been taken into account since the skull as a whole tend to become thicker with age (see subsection 2.1.4).

One can observe a significant linear relationship between EF strength and age in both the left and right hippocampus ($r_{left} = -0.64, p_{left} = 0.0002$; $r_{right} = -0.50, p_{right} = 0.006$), where the EF strength decrease with about 10 V/m with an increase of 20 years in age. However, as mentioned in the previous subsection, it is not possible to know whether the effects we see in Figure 4.5 are due to age or BMI, as the group examined turns out to have an increased BMI as a function of age. Disregarding this, the decrease in EF strength with age may be what causes the seizure threshold to increase with age.

5.1.3 Effect of Sex

The boxplots seen in Figure 4.6 demonstrate the differences in EF strength in the hippocampus for female and male patients. Looking at the plot for the left hippocampus, one sees that female patients generally experience a higher EF strength. The median value for female patients is around 56 V/m, while the median for male patient is around 46 V/m. On the right side, the median for female patients is around 92 V/m, while the male median is around 74 V/m. The difference is statistically significant on both sides ($t_{left} = -4.13$, $p_{left} < 0.001$; $t_{right} = -4.79$, $p_{right} < 0.0001$). Furthermore, Figure 4.8 reveals a positive correlation ($r = 0.71$) between sex and intracranial volume (eTIV), meaning female patients tend to have smaller intracranial volumes. Hence, the results seen in Figure 4.6 is probably to a large extent caused by different head sizes.

If high EF strength in the hippocampus is associated with side effects, then the results in Figure 4.5 and Figure 4.6 show that women and young people experience significantly higher EF strength compared to men and older people. This is the same group Brus et al. [39] found out had a higher risk of experiencing subjective memory worsening. It is nevertheless possible that the high field magnitude will be compensated for by women receiving a lower dose. This means that women will be exposed to the electric field for a shorter time than men of the same age. Assuming there is a connection between volume change and electric field strength in the hippocampus, one would expect that the differences in volume change between female and male patients would be close to zero. This will be further discussed in subsection 5.2.3.

5.1.4 Effect of Intracranial Volume

From Figure 4.7, it appears that smaller intracranial volume is associated with higher EF strength in the hippocampi and that higher intracranial volume leads to weaker EF strength in the hippocampi. There is a significant negative linear relationship in both the left and right hippocampus ($r_{left} = -0.53$, $p_{left} = 0.003$; $r_{right} = -0.58$, $p_{right} < 0.001$). On the left side, one can see a decrease of about 10 V/m when the estimated total intracranial volume increase with $0.3 \cdot 10^5$ mm^3. The same amount of decrease in EF strength is seen on the right side with an increase of $0.2 \cdot 10^5$ mm^3 in intracranial volume. The effect, therefore, seems to be greater on the right side. As mentioned in the last subsection, intracranial volume seems to be highly correlated with sex ($r = 0.71$). This could be one of the reasons why the seizure threshold is lower for women than for men.

5.1.5 Effect of Multiple Variables

The two multiple regression analyses from subsection 4.1.5 use BMI, age, sex and estimated total intracranial volume (eTIV) as predictors for the EF strength in the left and right hippocampus. Table 4.3 shows the summary of the multiple regression model for $EF_{Left.Hippo}$. Only two significant predictor variables, age and eTIV, can be found, where age appears to have the greatest effect on $EF_{Left.Hippo}$. To only get two significant predictors was unexpected, as all of the variables individually had shown a significant correlation with EF strength in the left hippocampus. However, the model as a whole is significant ($p = 6 \cdot 10^{-6}$) and explains 64 % of the variation in $EF_{Left.Hippo}$

Table 4.4, presents the summary of the multiple linear regression analysis for $EF_{Right.Hippo}$, and contains no significant predicting variables, even though the model as a whole is significant ($p = 3 \cdot 10^{-5}$) and explains 59 % of the variation. A reason for this may be that some of the variables explain the same variation in $EF_{Right.Hippo}$. Multicollinearity found in Figure 4.8 demonstrate that the predicting variables are dependent on each other. This breaks with the assumptions for the linear model. High correlation values between both BMI and age and between sex and eTIV, indicate that one can not change the variable BMI without changing age and one can not change the variable sex without changing the variable eTIV. Creating models for EF strength based on only BMI and sex, BMI and eTIV, age and sex or age and eTIV would therefore probably give more reliable results for the individual predictors than all of them together. Multicollinearity is also present in the model for $EF_{Left.Hippo}$. The multiple regression models created seem to predict the simulated EF strength in the left and right hippocampus very well for the patients in this study. However, it is not easy to distinguish what actually affects the electric field the most.

5.2 Volume Change

5.2.1 Effect of Electric Field Strength

The results found in Figure 4.11 and 4.12 regarding the relationship between volume change and EF strength are in line with previous findings by Argyelan et al. [6]. They show positive correlation between the volume change and EF strength in left hippocampus ($r = 0.46$, $p = 0.01$) and left amygdala ($r = 0.60$, $p = 0.0005$). What stands out is that no correlation was found in the right amygdala, in addition to a much steeper slope for the left amygdala. These findings of non-correlation on the right side, may be a result of the relationship not actually being linear. Because of limited space in the brain, there is limited space for the structures to expand. If it is assumed that missing correlation between EF strength and volume change in the right hippocampus is due to ceiling effects, like Argyelan et al. [6] assumed, it could be possible that the graph would stabilise around 4 % volume change.

Table 4.5 shows that the simple linear regression model with EF strength as the predictor explains 18 % of the variation in volume change in the left hippocampus. This is only 3 % less than the multiple linear regression model. But compared to the multiple linear regression model, the simple linear regression model is statistically significant. This model is therefore considered a better predictor of volume change in the left hippocampus.

It is also important to remember that the electric field simulation is a static image, and only represents what the electric field would look like in a brief moment undergoing ECT. The volume change, on the other hand, is the result after the whole treatment ranging from 3 to 18 sessions. A model including the time aspect might therefore be a better approach. Volume change as a function of the EF strength times the exposure time will be discussed in section 5.3.

5.2.2 Effect of Age

The results seen in Figure 4.13 are not significant. Why the results ended up looking like this is not intuitive. No effect of age on volume change could indicate that the age-based method for calculating the stimulus dose works well since people of different age roughly experience the same amount of structural changes.

5.2.3 Effect of Sex

There is a significant difference in volume change between female and male patients in the left hippocampus ($t = 2.2$, $p = 0.04$), but not in the right hippocampus. Lager volume changes in the hippocampus for women compared to men can be observed in Figure 4.14, but as the effect of the EF strength on volume change, the results are only significant on the left side. In subsection 5.1.3 it was discussed how the EF strength have a negative correlation with sex (EF strength is greater in the hippocampus for female patients than male patients) and how sex is positively correlated with intracranial volume (female patients tend to have smaller intracranial volumes). This could indicate that a significantly higher EF strength in female patients, due to smaller head size, induces volume changes in the left hippocampus significantly greater than the volume changes in the left hippocampus for male patients. Said in other words, significantly lower EF strength in male patients due to bigger head size may induce volume changes in the left hippocampus that is significantly smaller than the volume changes in the left hippocampus for female patients. These findings may suggest that the sex-specific dose correction is not enough to ensure equal response of the treatment. If larger volume changes in the hippocampus are associated with clinical improvement, the ECT stimulus parameters should be adjusted, so that male patients get larger volume changes. If, on the other hand, changes of the hippocampal volumes are associated with side effects, the dose parameters should be adjusted so that the volume changes in women are reduced.

No significant difference in volume change on the right side is maybe caused by the ceiling effect. If the volume reaches its maximum for a specific EF strength, and most of the patients experience an EF strength that exceeds this value in the right hippocampus, one will not observe large differences in volume change between the sexes in that structure. High EF strength on the right side is expected because all patients got RUL ECT.

As seen in Figure 4.8, the difference in the number of ECT sessions between female and male patients is not significant (p-value for the r-value is the same as for the t-test for a simple linear regression model), meaning the variable nECTs do probably not contribute to the differences found between the sexes.

5.2.4 Effect of Number of ECT Sessions

The results show significant positive correlation for nECTs and volume change in the right hippocampus ($r = 0.46$, $p = 0.01$). From the plot in Figure 4.15, it seems like the volume change in the right hippocampus increase with 2 % if the number of ECT sessions increase by approximately 7. Of all the predicting variables chosen for the multiple regression analysis for volume change, nECTs was the only variable that was significantly correlated with volume change in the right hippocampus (see Figure 4.17b).

No significant correlation is found for the left hippocampus. By looking at the plot for the left hippocampus in Figure 4.15 it looks like there is a tendency for increasing volume change with an increasing number of ECT sessions. Furthermore, the relationship observed between volume change and the number of ECTs looks very similar to the results found by Oltedal et al. [7], that discovered a significant relationship between the number of ECT sessions and the change of the hippocampal volume on both the left and the right side. Therefore, it seems reasonable to assume that hippocampal volume change is related to the number of ECT sessions, but nECTs affect the volume change in the right hippocampus the most.

5.2.5 Effect of BMI

Interestingly, the volume change did not show clear reduction when it was presented as a linear function of BMI (see Figure 4.16). The correlation values close to zero for both the left and right hippocampus demonstrate no linear relationship found between the variables, volume change and BMI. Hence, volume change in the hippocampus caused by ECT seems to be unaffected by BMI by evaluating the statistical values. The effect of BMI could still be present in the electric field, but it is not a good predictor for volume change in the hippocampus itself in this study. Note that there are only two points plotted for BMI>30. This leads to greater uncertainties for the linear model in this area. A larger study should be carried out with a broader variation in BMI to get a model valid for a wider range of BMI values.

5.2.6 Effect of Multiple Variables

The multiple regression analysis of the effects of multiple variables on ΔV did not reach statistical significance, as the p-values for both models, $\Delta V_{Left.Hippo}$ and $\Delta V_{Right.Hippo}$, were higher than 0.05 ($p_{Left} = 0.06$, $p_{Right} = 0.09$). Not a single estimated coefficient for $\Delta V_{Left.Hippo}$ in Table 4.7 is statistically significant ($p > 0.1$ for all coefficients). In Table 4.8, containing information about the multiple regression analysis for $\Delta V_{Right.Hippo}$, there is only one significant estimated coefficient, nECT ($p = 0.007$). Comparing the multiple regression model for $\Delta V_{Right.Hippo}$ with the simple regression model in subsection 4.2.1, it seems like nECTs is a better predictor for volume change in the right hippocampus than EF strength, since at least 17 % of the variance in $\Delta V_{Right.Hippo}$ is explained by the multiple regression model, compared to zero in the simple linear regression model.

A reason why there are no significant coefficients in the multiple regression analysis for left hippocamps might be that multicollinearity is present. Volume change in the left hippocampus is correlated with EF strength, which further is strongly correlated with age, sex and BMI (see Figure 4.17a). The large variation in age and dose parameters within the patient group possibly also makes it difficult to predict the volume change. Additionally, undiscovered factors may have affected the results as well.

5.3 Dose

Figure 4.18 and Figure 4.19 illustrate no clear association between volume change and average dose or volume change and cumulative dose. Hence, the relationship between volume change and stimulus dose in millicoulomb remains unclear in this thesis. Figure 4.20 and Figure 4.21, on the other hand, show statistically significant relationships between field exposure and volume change. Looking at volume change in the left and right hippocampus separately, the relationship is only significant on the right side ($r = 0.44$, $p = 0.02$). By studying data from both the left and right hippocampus together, a significant positive correlation appears ($r = 0.37$, $p = 0.004$) between field exposure and volume change in the hippocampi. These findings suggest that field exposure is a better predictor for volume change than the stimulus dose. A possible reason for this is that the field exposure considers what is going on inside the brain, unlike the stimulus dose, which only describes how the current is delivered to the head. Studying field exposure in the process of calculating the dose could maybe contribute to avoid overexposure or underexposure.

5.4 Methodological Considerations

5.4.1 Study Participants

The participant group in this thesis had a balanced sex distribution, with 15 female and 14 male patients. Sex balance enabled studying differences between the sexes, while the sample size of 29 participants turned out to be large enough to achieve statistically significant results. Future studies should still be done with a larger sample size to falsify or verify the results of this project.

The large variation in age (see Table 3.1) made it difficult to study the effect of BMI. This was because BMI correlated with age, in addition to the fact that age-related factors itself affect the EF strength. Additionally, patients were given a dose determined by age. Studying several patients of the same age would therefore make it easier to exclude the effects of other parameters, like large dose differences and age-related effects, and only investigate the effect of BMI.

5.4.2 The ECT Procedure

Positioning of the electrodes was done based on d'Elia, but does not necessarily correspond to the exact location chosen for the simulation. The reason for this is both that the electrodes may have been placed a little differently than shown in Figure 3.1, and that the electrode placement in the simulation only is an approximation of the d'Elia electrode placement. Hence, the electric field distribution simulated may not correspond exactly to the true electric field distribution. The extent to which a small change in electrode placement affects the electric field distribution should be further investigated.

5.4.3 Dose Parameters

The stimulus dose is defined by four parameters; current, pulse width, pulse frequency and total stimulus duration (see Equation 2.46). For all the patients, the current is 900 mA. Pulse width, pulse frequency and total stimulus duration, on the other hand, may vary between individuals. Although two patients have received the same stimulus dose, it is possible that different dose parameters were used to achieve this dose.

In this study, it was investigated whether one of the stimulus parameters, current, has an effect on volume change (since the amplitude of the current is directly proportional to the electric field strength). Additionally, field exposure, which includes the product of the pulse width, pulse frequency and total stimulus duration for each treatment, was investigated. Since it is known that the different dose parameters affect the outcome of the treatment differently (see section 2.3), it should maybe be investigated if some of the other stimulus parameters have an effect on the electric field and volume change alone.

5.4.4 MRI Limitations

Segmentations done by FreeSurfer and ROAST depend on the T1-weighted MR images. The FSPGR scan takes 10:32 min (see Table 3.3), so staying perfectly still all that time is difficult. Hence, head movements, B_0 inhomogeneity, gradient artefacts and RF noise are some factors that may have contributed to errors in the segmentation. Correction for B_0 inhomogeneity and gradient non-linearity was performed in the pre-processing (subsection 3.4.1) and FS analysis (subsection 3.4.2), which leads to the effects of these being minimised.

Furthermore, poor contrast between tissues may also have contributed to difficulties with distinguishing the boundaries between the different structures. Hence, voxels not belonging to a structure may have been included, while voxels actually belonging to a structure may have been excluded. It is also difficult to distinguish between skull and CSF since both are dark on a T1-weighted image. Since the electric field strength in a structure is an average value, where the highest and lowest one percentile are excluded from the calculation, some extra voxels or missing voxels probably do not affect the calculations of the average EF strengths to a great extent.

5.4.5 Limitations of the Volume Segmentation

A possible limitation is that the ROIs that were segmented in this project are small structures. Moreover, the volume changes that occur are of a few percentages. Hence, incorrect segmentation of voxels in the boundaries between the structures may therefore make a difference in the calculated volume changes. At the same time, the FreeSurfer pipeline is referred to as state-of-the-art anatomical processing and never reported problems with data quality or segmentation. It is therefore assumed that the images and volumes used in this thesis were of sufficient quality.

There is also a specific module in development for segmenting the hippocampal subfields and the nuclei of the amygdala with FreeSurfer 7. This module ensures that the segmentation of the hippocampus and amygdala do not overlap or have gaps between them [74]. Studying the subfields of the hippocampus was beyond the scope of the current thesis, but should be investigated in the future.

Furthermore, Oltedal et al. [7] found no significant changes in hippocampal volumes for the control subjects. It therefore seems reasonable to assume that other parameters (than the ECT treatment) that possibly could have had an effect on hippocampal volume change during the treatment period are negligible.

5.4.6 Limitations of the Electric Field Simulations

First of all, inaccurate head conductivities and geometry estimations of the head based on the MRI affects the EF calculations. ROAST only segments the head into scalp, skull, CSF, grey matter, white matter and air cavities, even though some of these tissue types clearly are inhomogenous and consist of multiple layers with different electric characteristics. In subsection 2.1.4, it was shown how the skull is a three-layered structure and that the scalp consists of multiple layers, including skin, subcutaneous fat and muscles. When studying the effect of BMI, which possibly involves different thicknesses of subcutaneous fat, this reduction of complexity of the scalp is considered a source of uncertainty. The same applies to the representation of the skull as a single-layered structure when studying the age effects.

Another source of inaccuracy is simplifying the tissue conductivity to be uniform. Both white and grey matter conductivity have anisotropic properties but is treated as isotropic in ROAST. As mentioned in subsection 2.1.4, this can lead to errors in the calculation of EF strength.

Furthermore, very thin layers of CSF is challenging to segment with a resolution of 1 mm^3. In some regions, the thickness of CSF is close to the resolution [23]. Because of its high conductivity, CSF plays a significant role in determining the current flow. Incorrect segmentation of CSF may therefore lead to errors in the calculations of the electric field. Additionally, functional changes that may happen during the treatment that can affect the electric field are not included in the simulation since it is a static image.

5.5 Conclusions and Future Work

The results of this thesis indicate that the age-based method, corrected for sex-specific differences in seizure threshold, does not take into account the individual differences in a way that is sufficient for equal treatment effects. ECT treatment based on the age-based method may lead to much higher electric field strengths in the hippocampi than necessary for women, inducing significantly greater volume change in the left hippocampus compared to male patients, potentially contributing to side effects. Therefore, individual adjustment of the current amplitude should be explored, as this hopefully could reduce some of the side effects. The use of field exposure in calculating the dose could also be a way to avoid overexposure or underexposure. To investigate whether the volume change and electric field strength are associated with side effects or clinical outcome was beyond this project's scope. Future work in this field should maybe include studying the role of the EF strength in hippocampal subfields in regard to volume change, clinical outcome and side effects.

The relationship found between volume change and electric field strength in this thesis supports the findings of Argyelan et al. [6], although a slightly different method was used. Furthermore, negative correlation was found between electric field strength in the hippocampi and BMI. Further investigation of the relationship between BMI and cranial subcutaneous fat is needed to draw any conclusions regarding how BMI affects EF strength. Future studies should also analyse the effect of BMI on EF strength in the hippocampus within a group of the same age to remove the effect of age. Moreover, no significant reduction in volume change was found for increasing BMI. A similar study should therefore be replicated on a larger data set (GEMRIC) to validate or falsify the results.

Furthermore, the results in this thesis showed a decrease in EF strength with age, which may be related to the increasing seizure threshold with age. However, no significant correlations were found between age and volume change. This could indicate that ECT given by the age-based method works well since it leads to minor differences in volume change between the different age groups.

Few significant predictors were found for volume change in the right hippocampus. Only the number of ECT sessions and the field exposure turned out to have a clear effect on $\Delta V_{Right.Hippo}$.

As Argyelan et al. [6] suggested, this might be because of ceiling effects or non-linear relationships. This study found it difficult to distinguish which predictors had the greatest effect on EF strength and volume change due to the high correlation between the predicting variables. However, the identification of significant predictors for the EF strength and volume change may be important in the development of a more personalised dosage.

Bibliography

[1] World Health Organization, *Depression*, Accessed 14 April 2021, Jan. 2020. [Online]. Available: `https://www.who.int/news-room/fact-sheets/detail/depression`.

[2] S. Carney, P. Cowen, K. Dearness, and J. Eastaugh, "Efficacy and safety of electroconvulsive therapy in depressive disorders: A systematic review and meta-analysis," *Lancet*, vol. 361, pp. 799–808, Mar. 2003. DOI: `10.1016/S0140-6736(03)12705-5`.

[3] H. K. Schoeyen, U. Kessler, O. A. Andreassen, B. H. Auestad, P. Bergsholm, U. F. Malt, G. Morken, K. J. Oedegaard, and A. Vaaler, "Treatment-resistant bipolar depression: A randomized controlled trial of electroconvulsive therapy versus algorithm-based pharmacological treatment," *Am J Psychiatry*, vol. 172, no. 1, pp. 41–51, Jan. 2015. DOI: `10.1176/appi.ajp.2014.13111517`.

[4] M. S. George, J. J. Taylor, and B. Short, "Treating the depressions with superficial brain stimulation methods," in *Handbook of Clinical Neurology*. Elsevier, 2013, vol. 116, pp. 399–413, ISBN: 978-0-444-53497-2. DOI: `10.1016/B978-0-444-53497-2.00033-4`. [Online]. Available: `https://linkinghub.elsevier.com/retrieve/pii/B9780444534972000334`.

[5] O. T. Ousdal, M. Argyelan, K. L. Narr, C. Abbott, B. Wade, M. Vandenbulcke, M. Urretavizcaya, I. Tendolkar, A. Takamiya, M. L. Stek, and et al., "Brain changes induced by electroconvulsive therapy are broadly distributed," *Biological Psychiatry*, vol. 87, no. 5, pp. 451–461, Mar. 2020, ISSN: 00063223. DOI: `10.1016/j.biopsych.2019.07.010`.

[6] M. Argyelan, L. Oltedal, Z.-D. Deng, B. Wade, M. Bikson, A. Joanlanne, S. Sanghani, H. Bartsch, M. Cano, A. M. Dale, and et al., "Electric field causes volumetric changes in the human brain," *eLife*, vol. 8, e49115, Oct. 2019, ISSN: 2050-084X. DOI: `10.7554/eLife.49115`.

[7] L. Oltedal, K. L. Narr, C. Abbott, A. Anand, M. Argyelan, H. Bartsch, U. Dannlowski, A. Dols, P. van Eijndhoven, L. Emsell, and et al., "Volume of the human hippocampus and clinical response following electroconvulsive therapy," *Biological Psychiatry*, vol. 84, no. 8, pp. 574–581, Oct. 2018, ISSN: 00063223. DOI: `10.1016/j.biopsych.2018.05.017`.

[8] I. van Oostrom, P. van Eijndhoven, E. Butterbrod, M. H. van Beek, J. Janzing, R. Donders, A. Schene, and I. Tendolkar, "Decreased cognitive functioning after electroconvulsive therapy is related to increased hippocampal volume: Exploring the role of brain plasticity," *J ECT*, vol. 34, no. 2, pp. 117–123, Jun. 2018. DOI: `10.1097/YCT.0000000000000483`.

[9] A. M. Leaver, M. Vasavada, A. Kubicki, B. Wade, J. Loureiro, G. Hellemann, S. H. Joshi, R. P. Woods, R. Espinoza, and K. L. Narr, "Hippocampal subregions and networks linked with antidepressant response to electroconvulsive therapy," *Mol Psychiatry*, 2020. DOI: `10.1038/s41380-020-0666-z`.

[10] C. M. Swartz, *Guide to Electroconvulsive Therapy*. Revised for 2020, 32 pp., Downloaded e-book 9 March 2021.

[11] Helsedirektoratet, *Nasjonal faglig retningslinje om bruk av elektrokonvulsiv behandling - ECT*, Jun. 2017.

[12] D. J. Griffiths, *Introduction to Electrodynamics*, 4th Edition. Cambridge University Press, 2017, ISBN: 9781108420419. DOI: `10.1017/9781108333511`.

[13] H. D. Young and R. A. Freedman, *University physics with modern physics, Global Edition*, 14th Edition. Pearson Education Limited, 2016, ISBN: 9781292100319.

[14] R. A. Adams and C. Essex, *Calculus: A Complete Course*, 7th Edition. Pearson, 2017, ISBN: 9780321549280.

[15] E. R. Grüner, *Compendium PHYS212: Medical physics and technology*, version 1.0, Department of Physics and Technology, University of Bergen, 2012.

[16] Wikimedia Commons. (2020). Accessed 7 April 2021, [Online]. Available: `https://commons.wikimedia.org/wiki/File:VFPt_dipoles_magnetic.svg`.

[17] ——, (2010). Accessed 21 March 2021, [Online]. Available: `https://commons.wikimedia.org/w/index.php?curid=10508433`.

[18] ——, (2018). Accessed 21 March 2021, [Online]. Available: `https://commons.wikimedia.org/w/index.php?curid=67510332`.

[19] Y. Huang, A. Datta, M. Bikson, and L. C. Parra, "Realistic volumetric-approach to simulate transcranial electric stimulation—roast—a fully automated open-source pipeline," *Journal of Neural Engineering*, vol. 16, no. 5, p. 056 006, Jul. 2019, ISSN: 1741-2552. DOI: `10.1088/1741-2552/ab208d`.

[20] A. V. Peterchev, M. A. Rosa, Z.-D. Deng, J. Prudic, and S. H. Lisanby, "Electroconvulsive therapy stimulus parameters: Rethinking dosage," *The Journal of ECT*, vol. 26, no. 3, pp. 159–174, Sep. 2010, ISSN: 1095-0680. DOI: `10.1097/YCT.0b013e3181e48165`.

[21] H. McCann, G. Pisano, and L. V. Beltrachini, "Reported human head tissue electrical conductivity values," *Brain Topogr*, vol. 32, pp. 825–858, Sep. 2019. DOI: `10.1007/s10548-019-00710-2`.

[22] M. Akhtari, H. C. Bryant, A. N. Mamelak, E. R. Flynn, L. Heller, J. J. Shih, A. Matlachov, D. M. Ranken, E. D. Best, M. A. DiMauro, and et al., "Conductivities of three-layer live human skull," *Brain Topography*, vol. 14, no. 3, pp. 151–167, Mar. 2002. DOI: `10.1023/A:1014590923185`.

[23] Y. Huang, J. P. Dmochowski, Y. Su, A. Datta, C. Rorden, and L. C. Parra, "Automated mri segmentation for individualized modeling of current flow in the human head," *Journal of Neural Engineering*, vol. 10, no. 6, Dec. 2013, ISSN: 1741-2560, 1741-2552. DOI: `10.1088/1741-2560/10/6/066004`.

[24] S. M. Rampersad, D. F. Stegeman, and T. F. Oostendorp, "Single-layer skull approximations perform well in transcranial direct current stimulation modeling," *IEEE Transactions on Neural Systems and Rehabilitation Engineering*, vol. 21, no. 3, pp. 346–353, 2013. DOI: `10.1109/TNSRE.2012.2206829`.

[25] T. Wagner, F. Fregni, S. Fecteau, A. Grodzinsky, M. Zahn, and A. Pascual-Leone, "Transcranial direct current stimulation: A computer-based human model study," *NeuroImage*, vol. 35, pp. 1113–1124, Apr. 2007, ISSN: 10538119. DOI: `10.1016/j.neuroimage.2007.01.027`.

[26] A. Datta, V. Bansal, J. Diaz, J. Patel, D. Reato, and M. Bikson, "Gyri-precise head model of transcranial direct current stimulation: Improved spatial focality using a ring electrode

versus conventional rectangular pad," *Brain Stimulation*, vol. 2, no. 4, pp. 201–207, Oct. 2009, ISSN: 1935861X. DOI: `10.1016/j.brs.2009.03.005`.

[27] W. H. Lee, Z.-D. Deng, T.-S. Kim, A. F. Laine, S. H. Lisanby, and A. V. Peterchev, "Regional electric field induced by electroconvulsive therapy in a realistic finite element head model: Influence of white matter anisotropic conductivity," *NeuroImage*, vol. 59, no. 3, pp. 2110–2123, Feb. 2012, ISSN: 10538119. DOI: `10.1016/j.neuroimage.2011.10.029`.

[28] J. H. Blok, D. F. Stegeman, and A. van Oosterom, "Three-layer volume conductor model and software package for applications in surface electromyography," *Annals of Biomedical Engineering*, vol. 30, no. 4, pp. 566–577, Apr. 2002, ISSN: 0090-6964. DOI: `10.1114/1.1475345`.

[29] J. Petrofsky, "The effect of the subcutaneous fat on the transfer of current through skin and into muscle," *Medical Engineering & Physics*, vol. 30, no. 9, pp. 1168–1176, Nov. 2008, ISSN: 13504533. DOI: `10.1016/j.medengphy.2008.02.009`.

[30] A. R. Craven, K. Kompus, and K. Hugdahl, "Segmentation and quantification of subcutaneous fat from cranial, T1-weighted structural MRI," unpublished, N.D.

[31] J. P. Pinel and M. Edwards, *A colorful introduction to the anatomy of the human brain: A brain and psychology coloring book*, 2nd Edition. Pearson Education Inc. (US), 2008, ISBN: 9780205548743.

[32] M. Matsumae, R. Kikinis, I. A. Mórocz, A. V. Lorenzo, T. Sándor, M. S. Albert, P. M. Black, and F. A. Jolesz, "Age-related changes in intracranial compartment volumes in normal adults assessed by magnetic resonance imaging," *Journal of Neurosurgery*, vol. 84, no. 6, pp. 982–991, 1996. DOI: `https://doi.org/10.3171/jns.1996.84.6.0982`.

[33] C. Westbrook and C. Kaut, *MRI in practice*, 2nd Edition. Blackwell Science, 1998, ISBN: 0632042052.

[34] M. A. Brown and R. C. Semelka, *MRI: Basic Principles and Applications*, 3rd Edition. John Wiley Sons, Inc, 2003, ISBN: 0471433101.

[35] Questions and Answers in MRI, *Chemical shift artifact*, Accessed 10 June 2021. [Online]. Available: `http://mriquestions.com/chemical-shift-artifact.html`.

[36] C. Westbrook, *MRI in practice*, 3rd Edition. Wiley-Blackwell, 1, ISBN: 9781405160858.

[37] U. Kessler and K. J. Ødegaard, "ECT og andre nevrostimulerende behandlingsformer," in *Praktisk psykiatri*, T. F. Aarre and A. A. Dahl, Eds., 2nd ed. Fagbokforlaget, 2018, ch. 22, pp. 485–498.

[38] G. Gazdag and G. S. Ungvari, "Electroconvulsive therapy: 80 years old and still going strong," *World Journal of Psychiatry*, vol. 9, no. 1, pp. 1–6, Jan. 2019, ISSN: 2220-3206. DOI: `10.5498/wjp.v9.i1.1`.

[39] O. Brus, P. Nordanskog, U. Båve, Y. Cao, Å. Hammar, M. Landén, J. Lundberg, and A. Nordenskjöld, "Subjective memory immediately following electroconvulsive therapy," *The Journal of ECT*, vol. 33, pp. 96–103, 2 Jun. 2017. DOI: `10.1097/YCT.0000000000000377`.

[40] H. Sackeim, P. Decina, I. Prohovnik, and S. Malitz, "Seizure threshold in electroconvulsive therapy: Effects of sex, age, electrode placement, and number of treatments," *Arch Gen Psychiatry*, vol. 44, no. 4, pp. 355–360, 1987. DOI: `doi:10.1001/archpsyc.1987.01800160067009`.

[41] H. Qiu, X. Li, W. Zhao, L. Du, P. Huang, Y. Fu, T. Qiu, P. Xie, H. Meng, and Q. Luo, "Electroconvulsive therapy-induced brain structural and functional changes in major depressive disorders: A longitudinal study," *Medical science monitor : international medical journal of experimental and clinical research*, vol. 22, no. 1, pp. 4577–4586, Nov. 2016. DOI: `10.12659/msm.898081`.

[42] P. C. Mulders, A. Llera, C. F. Beckmann, M. Vandenbulcke, M. Stek, P. Sienaert, R. Redlich, G. Petrides, M. L. Oudega, L. Oltedal, and et al., "Structural changes induced by electroconvulsive therapy are associated with clinical outcome," *Brain Stimulation*, vol. 13, no. 3, pp. 696–704, May 2020, ISSN: 1935861X. DOI: `10.1016/j.brs.2020.02.020`.

[43] A. Takamiya, J. Chung, K. Liang, A. Graff-Guerrero, M. Mimura, and T. Kishimoto, "Effect of electroconvulsive therapy on hippocampal and amygdala volumes: Systematic review and meta-analysis," *Br J Psychiatry*, vol. 212, pp. 19–26, 2018.

[44] S. Wilkinson, G. Sanacora, and M. Bloch, "Hippocampal volume changes following electroconvulsive therapy: A systematic review and meta-analysis," *Biol Psychiatry Cogn*

Neurosci Neuroimaging, vol. 2, pp. 327–35, 2017. DOI: `10.1016/j.bpsc.2017.01.011`.

[45] L. Schmaal, D. Veltman, T. van Erp, P. Sämann, T. Frodl, N. Jahanshad, E. Loehrer, H. Tiemeier, A. Hofman, W. Niessen, and et al., "Subcortical brain alterations in major depressive disorder: Findings from the enigma major depressive disorder working group," *Mol Psychiatry.*, vol. 21, pp. 806–12, Jun. 2016. DOI: `10.1038/mp.2015.69`.

[46] B. Cao, Q. Luo, Y. Fu, L. Du, T. Qiu, X. Yang, X. Chen, Q. Chen, J. C. Soares, R. Y. Cho, X. Y. Zhang, and H. Qiu, "Predicting individual responses to the electroconvulsive therapy with hippocampal subfield volumes in major depression disorder," *Sci Rep*, vol. 8, p. 5434, 2018. DOI: `10.1038/s41598-018-23685-9`.

[47] P. Eriksson, E. Perfilieva, T. Björk-Eriksson, A.-M. Alborn, C. Nordborg, D. A. Peterson, and F. H. Gage, "Neurogenesis in the adult human hippocampus," *Nat Med*, vol. 4, pp. 1313–1317, 1998. DOI: `10.1038/3305`.

[48] B. Jacobs, H. van Praag, and F. Gage, "Adult brain neurogenesis and psychiatry: A novel theory of depression," *Mol Psychiatry 5*, pp. 262–269, 2000. DOI: `10.1038/sj.mp.4000712`.

[49] T. M. Madsen, A. Treschow, J. Bengzon, T. G. Bolwig, O. Lindvall, and A. Tingström, "Increased neurogenesis in a model of electroconvulsive therapy," *Biological psychiatry*, vol. 47, no. 12, pp. 1043–1049, 2000. DOI: `10.1016/s0006-3223(00)00228-6`.

[50] J. Nuninga, R. Mandl, M. Boks, S. Bakker, M. Somers, S. Heringa, W. Nieuwdorp, H. Hoogduin, R. Kahn, P. Luijten, and I. Sommer, "Volume increase in the dentate gyrus after electroconvulsive therapy in depressed patients as measured with 7t," *Mol Psychiatry*, vol. 25, no. 7, pp. 1559–1568, Jul. 2020. DOI: `10.1038/s41380-019-0392-6`.

[51] *Freesurfer*. [Online]. Available: `http://surfer.nmr.mgh.harvard.edu`.

[52] RStudio Team, *RStudio: Integrated Development Environment for R*, RStudio, PBC., Boston, MA, 2020. [Online]. Available: `http://www.rstudio.com/`.

[53] S. A. Montgomery and M. Åsberg, "A new depression scale designed to be sensitive to change," *British Journal of Psychiatry*, vol. 134, no. 4, pp. 382–389, Apr. 1979, ISSN: 0007-1250, 1472-1465. DOI: `10.1192/bjp.134.4.382`.

[54] L. Oltedal, U. Kessler, L. Ersland, R. Grüner, O. A. Andreassen, J. Haavik, P. I. Hoff, Å. Hammar, A. M. Dale, K. Hugdahl, and et al., “Effects of ECT in treatment of depression: Study protocol for a prospective neuroradiological study of acute and longitudinal effects on brain structure and function,” *BMC Psychiatry*, vol. 15, no. 1, p. 94, Dec. 2015, ISSN: 1471-244X. DOI: `10.1186/s12888-015-0477-y`.

[55] *User Manual Thymatron® System IV*, Somatics LLC. [Online]. Available: `http://www.thymatron.com/downloads/System_IV_Instruction_Manual_Rev21.pdf`.

[56] G. d’Elia, “Unilateral electroconvulsive therapy,” *Acta Psychiatr Scand Suppl*, vol. 215, pp. 1–98, 1970.

[57] Questions and Answers in MRI, *Gradient linearity*, Accessed 4 May 2021, 2021. [Online]. Available: `http://mriquestions.com/gradient-linearity.html`.

[58] M. Reuter, N. J. Schmansky, H. D. Rosas, and B. Fischl, “Within-subject template estimation for unbiased longitudinal image analysis,” *NeuroImage*, vol. 61, no. 4, pp. 1402–1418, Jul. 2012, ISSN: 10538119. DOI: `10.1016/j.neuroimage.2012.02.084`.

[59] M. Fogarty, *Recon-all*, Accessed 5 May 2021, 2017. [Online]. Available: `https://surfer.nmr.mgh.harvard.edu/fswiki/recon-all`.

[60] ——, *Subcortical Segmentation*, Accessed 5 May 2021, 2018. [Online]. Available: `https://freesurfer.net/fswiki/SubcorticalSegmentation`.

[61] D. Cordero, *LongitudinalProcessing*, Accessed 5 May 2021, 2021. [Online]. Available: `https://surfer.nmr.mgh.harvard.edu/fswiki/LongitudinalProcessing`.

[62] M. Reuter and B. Fischl, “Avoiding asymmetry-induced bias in longitudinal image processing,” *NeuroImage*, vol. 57, no. 1, pp. 19–21, Jul. 2011, ISSN: 10538119. DOI: `10.1016/j.neuroimage.2011.02.076`.

[63] Y. Huang, *ROAST: realistic volumetric-approach-based simulator for transcranial electric stimulation*, Accessed 6 May 2021, 2019. [Online]. Available: `https://github.com/andypotatohy/roast`.

[64] V. Jurcak, D. Tsuzuki, and I. Dan, “10/20, 10/10, and 10/5 systems revisited: Their validity as relative head-surface-based positioning systems,” *NeuroImage*, vol. 34, no. 4, pp. 1600–1611, 2007, ISSN: 1053-8119. DOI: `https://doi.org/10.1016/j.neuroimage.2006.09.024`.

[65] Y. Huang, Y. Su, C. Rorden, J. Dmochowski, A. Datta, and L. C. Parra, "An automated method for high-definition transcranial direct current stimulation modeling," in *2012 Annual International Conference of the IEEE Engineering in Medicine and Biology Society*, 2012, pp. 5376–5379. DOI: `10.1109/EMBC.2012.6347209`.

[66] *Docker overview*, Accessed 11 May 2021, Docker Inc. [Online]. Available: `https://docs.docker.com/get-started/overview/`.

[67] *Manage data in Docker*, Accessed 11 May 2021, Docker Inc. [Online]. Available: `https://docs.docker.com/storage/`.

[68] *freesurfer/freesurfer*. [Online]. Available: `https://hub.docker.com/r/freesurfer/freesurfer`.

[69] *Docker run reference*, Accessed 12 May 2021, Docker Inc. [Online]. Available: `https://docs.docker.com/engine/reference/run/`.

[70] MathWorks Ref. Arch., *Create a MATLAB container image*, 2021. [Online]. Available: `https://github.com/mathworks-ref-arch/matlab-dockerfile`.

[71] RDocumentation, *Lm: Fitting linear models*, Accessed 13 June 2021. [Online]. Available: `https://www.rdocumentation.org/packages/stats/versions/3.6.2/topics/lm`.

[72] M. J. Campbell, D. Machin, and S. J. Walters, *Medical Statistics: A Textbook for the Health Sciences*, 4th Edition. John Wiley Sons Inc, 2007, ISBN: 9780470025192.

[73] RDocumentation, *Summary.lm: Summarizing linear model fits*, Accessed 13 June 2021. [Online]. Available: `https://www.rdocumentation.org/packages/stats/versions/3.6.2/topics/summary.lm`.

[74] J. E. Iglesias, *Segmentation of hippocampal subfields and nuclei of the amygdala (cross-sectional and longitudinal)*, Accessed 6 June 2021. [Online]. Available: `https://surfer.nmr.mgh.harvard.edu/fswiki/HippocampalSubfieldsAndNucleiOfAmygdala`.